

UNANNOUNCED

AD-A956 108



JPRS: 25,897

OTS: 64-21263

10 January 1964



SOVIET RESEARCH IN PRODUCTION AND  
 PHYSICAL METALLOGY OF PURE METALS

(SECOND PRINTING - 16 JUNE 1964)

**DISTRIBUTION STATEMENT A**

Approved for public release;  
Distribution Unlimited

**DTIC**  
**ELECTE**  
**APR 2 1992**  
**S B D**

U. S. DEPARTMENT OF COMMERCE  
 OFFICE OF TECHNICAL SERVICES  
 JOINT PUBLICATIONS RESEARCH SERVICE  
 Building T-30  
 Ohio Drive and Independence Avenue, S.W.  
 Washington 25, D. C.

Price: \$3.00

1-1

92 3 31 172

92-08216



## F O R E W O R D

This publication was prepared under contract for the Joint Publications Research Service as a translation or foreign-language research service to the various federal government departments.

The contents of this material in no way represent the policies, views or attitudes of the U. S. Government or of the parties to any distribution arrangement.

### PROCUREMENT OF JPRS REPORTS

All JPRS reports may be ordered from the Office of Technical Services. Reports published prior to 1 February 1963 can be provided, for the most part, only in photocopy (xerox). Those published after 1 February 1963 will be provided in printed form.

Details on special subscription arrangements for any JPRS report will be provided upon request.

No cumulative subject index or catalog of all JPRS reports has been compiled.

All current JPRS reports are listed in the Monthly Catalog of U. S. Government Publications, available on subscription at \$4.50 per year (\$6.00 foreign), including an annual index, from the Superintendent of Documents, U. S. Government Printing Office, Washington 25, D. C.

All current JPRS scientific and technical reports are cataloged and subject-indexed in Technical Translations, published semimonthly by the Office of Technical Services, and also available on subscription (\$12.00 per year domestic, \$16.00 foreign) from the Superintendent of Documents. Semiannual indexes to Technical Translations are available at additional cost.

**UNANNOUNCED**

<b>Accession For</b>	
NTIS GRA&I	<input checked="" type="checkbox"/>
DTIC TAB	<input type="checkbox"/>
Unannounced	<input type="checkbox"/>
Justification _____	
By _____	
Distribution/	
Availability Codes	
Dist	Avail and/or Special
A-1	

JPRS: 22,697



**SOVIET RESEARCH IN PRODUCTION AND PHYSICAL METALLURGY  
OF PURE METALS**

Following is a translation of 13 articles in the Russian-language anthology Metallurgiya i metallovedeniye chistykh metallov (Production and Physical Metallurgy of Pure Metals), No 4, Gosatomizdat, Moscow, signed to the press 31 May 1963, pages 5-10, 18-33, 47-63, 69-109, 122-148, 160-181, and 228-242. Authors' names accompany each article.

**TABLE OF CONTENTS**

	<u>Page</u>
The Iodide Method of Refining Zirconium. The Transfer of Nonmetallic Additions During Refining	1
The Effect of Hydrogen and Nitrogen on the Corrosion Resistance of Zirconium in Water and Steam	8
The Formation of Scale with a Structure $6ZrO_2 \cdot Nb_2O_5$ on Alloys of Zirconium with Niobium	27
Obtaining Molybdenum Single Crystals and their Properties	39
Investigation of the Distribution of Additions in Niobium After Zone Refining	46
Electron Diffraction and X-Ray Photographic Investigation of Oxide Films on Niobium	64
Investigation of the Kinetics of the Oxidation of Iodide Niobium Refined by the Electron-Beam Method	79

Table of Contents (Cont'd)

	<u>Page</u>
Reaction of Austenite Chromium-Nickel Steel with Liquid Lithium	97
Corrosion Resistance of Iron in Lithium	106
Corrosion Resistance of Titanium in Lithium	118
Changes of Properties During Cyclic Thermal Treatment, Durability and Internal Friction of Sap	124
The Mechanical Properties of Beryllium After Zone Recrystallization	139
Installation for the X-Ray Structural Analysis of Radioactive Materials	146

THE IODIDE METHOD OF REFINING ZIRCONIUM.  
THE TRANSFER OF NONMETALLIC ADDITIONS DURING REFINING

V. S. Yemel'yanov  
A. I. Yevstyukhin  
D. D. Abanin

Essence of the Problem

In the last ten years the iodide method of refining has become the most important final stage in the production of reactor-purity zirconium. Iodide zirconium, a new structural metal, has been adopted and is being used successfully in various new technologies. It is better than unre-fined metal obtained by the methods of metallothermy and electrolysis with respect to purity and properties. The advantages of iodide zirconium over other sorts of metal are especially manifest in its high corrosion resistance (approaching the noble metals) and high plasticity which makes it possible to fabricate articles of very complex configuration from it. A number of papers have been published in connection with the industrial use of the iodide method of refining zirconium [1-4]. They are devoted to a study of this process and the equipment that is used.

However, some details of the process and some of the possibilities of the method have not been clarified fully as yet. One of these questions is the transfer of additions from the starting metal into the refined metal during iodide deposition of zirconium on a hot filament. The data that are given in this paper were obtained in experiments on obtaining zirconium of especially high purity in our laboratory.

Iodide zirconium of industrial purity normally contains the following nonmetallic additions: 0.01-0.02% oxygen, 0.01% nitrogen, 0.003% hydrogen, and 0.01% carbon. The zirconium for physical research must have considerably less nonmetallic additions. It was proposed to reduce the content of nonmetallic additions by repeated iodide refining.

Our laboratory experiments showed that 2-fold and 3-fold refining of zirconium by the iodide method reduces the content of these additions, but less than could be expected. Table 1 shows the results of analyses for the content of nonmetallic additions of industrial iodide zirconium and metal after 2-fold and 3-fold iodide refining.

Table 1

Content of Nonmetallic Additions in Iodide Zirconium

Number of Iodide Refining Repetitions	Номер опыта	Addition Content, wt. %			
		Nitrogen	Oxygen	Hydrogen	Carbon
Initial electrolytic powder	1	0,110	0,420	0,005	0,115
Single-fold	1	0,010	0,020	0,0030	0,026
"	2	0,010	0,025	0,0028	0,030
"	3	0,010	0,021	0,0025	0,028
Two-fold	1	0,003	0,016	0,0018	0,009
"	2	0,003	0,019	0,0015	0,008
"	3	0,003	0,018	0,0018	0,008
Three-fold	1	0,002	0,009	0,0010	0,004
"	2	0,0015	0,010	0,0011	0,003
"	3	0,001	0,009	0,0010	0,004

It is seen from the data in Table 1 that the nitrogen content in zirconium with one-time refining is reduced approximately ten times and the oxygen content is reduced twenty times. Upon two-fold refining the nitrogen content is reduced by about three times and the oxygen only by 1.2 times. In three-fold iodide refining the nitrogen and oxygen content in the zirconium is reduced even more in comparison with two-fold refining but it is of the same order of magnitude as observed in two-fold refining.

The carbon content in zirconium in one-time iodide refining is reduced by about five times and in two-fold refining it is reduced by three times; in three-fold refining it is reduced by only about two times. The hydrogen content in zirconium in two-fold and three-fold refining almost does not change. There is some basis to assume that the content of additions in zirconium will be reduced still less upon further increase in the number of repetitions of the iodide refining process.

It is pointed out in works studying the iodide process of refining metals [5] that at relatively low temperatures oxides, nitrides, and carbides of zirconium do not interact with the iodine and do not form volatile compounds, and do not breakdown into component parts. In accordance with thermodynamic data, these additions should not transfer from the initial metal and deposit on the filament. However, in practice these additions do transfer and the transfer mechanism to this point is unexplained. The phenomenon of transfer of nonmetallic additions in the iodide refining process was demonstrated especially graphically in one of our works [4] when zirconium carbide was used as the initial raw material. We observed the deposition of zirconium carbide on the filament (but not metallic zirconium) and could not explain this phenomenon.

However, in the work of the Australian researchers, Sciefe and Wylie [6] it is reported that very pure thorium was obtained from its carbide using the iodide method (carbide had an oxygen content of less than 0.001% and carbon less than 0.005%). The authors indicate that the transfer agents of the carbon and hydrogen during iodide refining can be  $C_2H_2$  and CO which will breakdown (disassociate) on the hot filament with a generation of C,  $O_2$ , and  $H_2$ . The latter do not react with the filament and once again interact with the carbon in the raw material.

Acetylene and carbon dioxide vapors can accumulate during the refining process as a result of the interaction of the adsorbed water vapors (not completely eliminated from the raw material during degasification) with hydrogen and carbon that are also in the raw material. The authors of this work [6] calculate that when the iodide thorium is contaminated with oxygen in the amount of 0.001% and with carbon in the amount of 0.005% the pressure of the  $C_2H_2$  in the equipment should be of the order of 0.5 mm of mercury and the pressure of the CO should be about 1 mm of mercury.

Lunem [7] also points to the interaction of carbides and oxides as the source of the CO vapors that form in the hood. He says that the formation reaction of CO occurs when the initial metal is superheated, particularly due to the radiation of the filament, to a temperature above  $600^\circ C$ .

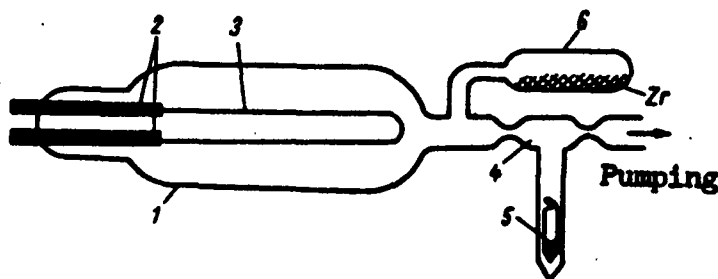
In our work we set ourselves the task of explaining experimentally the possible transfer of nonmetallic additions in repeated refining of zirconium and establishing the effect of varying degrees of degasification of the raw material on the transfer of additions.

### Research Methodology

At first the experiments on repeated refining of zirconium were conducted in hoods made from molybdenum glass 100 mm in diameter and 200-300 mm long. The degasification of the raw zirconium before iodide refining was done at  $350-400^\circ C$  at a vacuum of no less than  $10^{-4}$  mm of mercury. During

the refining process zirconium rods weighing 350-450 grams and 8-9 mm in diameter were obtained. It was noted that in obtaining rods of this thickness the raw material was superheated to 500-530°C due to the radiation of the filament (in comparison with 300-320°C for normal conditions) and the temperature of the outer walls of the hood reached 450°C. Under these conditions, as is known, the glass begins to give off oxygen which can serve as an additional source of contamination. Therefore, other conditions and methodology were selected which precluded the possibility of transfer of additions and contamination of the metal. The initial metal was degasified at a higher temperature and during the refining process the hood was heated to a lower temperature. To avoid superheating of the raw metal from the radiation of the filament the zirconium rods were kept to a thickness of 4-5 mm.

During the course of the work the raw zirconium was separately degasified and refined. Pre-degasified zirconium was put into the refining hood in quartz ampules at a high temperature. Then the hood was heated and worked at a lower temperature (300-320°C). The refining hood 1 (see the drawing) was made from molybdenum glass and was 100 mm in diameter and 500 mm long. On one end of the hood current-conducting electrodes 2 were soldered. They served two molybdenum rods 8 mm in diameter. A tungsten filament 3 that was 0.05 mm in diameter was fastened to them. The zirconium was deposited on the filament. On the other end of the hood a triangular joint 4 with two seals was fastened. Into this the ampule 5 with the iodide was placed. A quartz branch 6 was let off the main tube into which the raw metal was placed during degasification.



Equipment for Iodide Refining of Zirconium With High-Temperature Degasification of the Metal.

During degasification the hood was heated to 350°C and the quartz branch with the metal was heated to 850°C. The tungsten filament was heated at 1500°C. The vacuum in the hood was maintained at no less than  $10^{-4}$  mm of mercury. After degasification the hood was separated from the vacuum system, the iodine was distilled into the hood, and the zirconium from the branch also dropped into the hood.

In subsequent experiments the degasification of the raw metal was done separately in quartz ampules at 900-950°C and at a vacuum of 10<sup>-4</sup> mm of mercury for 20-25 hours. After this, the zirconium was placed in the hood without the quartz branch and the evacuation was done at 350°C. Then the hood was placed in a furnace and heated to 250°C. After the formation of zirconium iodide the filament heating was begun.

During the deposition of zirconium the temperature of the filament was maintained in the range 1200-1300°C and the temperature of the hood did not exceed 300-320°C. The deposition of the zirconium lasted 15-20 hours. The yield of zirconium was more than 95%. At the point of the raw metal a fluffy residue was left which consists basically of oxide films and zirconium nitrides. The final diameter of the rods of zirconium did not exceed 4-5 mm.

An electrolysis zirconium with a low content of metallic additions was used as the raw material for refining. In the first experiments this zirconium was used as a powder. In subsequent experiments it was remelted in an arc furnace and chips were made from the ingots. The iodide was premixed with CaO and NaJ to bind moisture and chlorine. Then it was taken out of this mixture in a vacuum. Then the iodide was subjected again to 2-fold resublimation in a vacuum and distilled in ampules.

A Discussion of the Results of the Experiment

Table 2 gives the typical analyses of the initial electrolytic zirconium for carbon, nitrogen, oxygen, and hydrogen content and also analyses of this metal after single iodide refining using the methodology described above.

Table 2

Content of Nonmetallic Additions (in wt.%)  
in Electrolysis and Iodide Zirconium

Zr	N <sub>2</sub>	O <sub>2</sub>	C	H <sub>2</sub>
Electrolytic . . . . .	0,005	0,400	0,008	0,008
Iodide . . . . .	0,002	0,002	0,004	0,0004

It is seen from these data that as a result of single iodide refining using the methodology described zirconium was obtained with very low hydrogen and oxygen content. Such low contents were not achieved

before by using three-fold iodide refining by the normal method. However, the nitrogen content in the iodide zirconium was reduced by only 2.5 times and the carbon content by only 2 times. The low extent to which the nitrogen and carbon contents are reduced in comparison with the hydrogen and especially the oxygen content can be explained by the insignificant content of these additions in the initial zirconium.

The rods of the iodide zirconium were extremely plastic (Brinell hardness 40-45 kg/mm<sup>2</sup>) with very clean grain boundaries and had exceptionally high corrosion resistance.

From the data that have been given it can be concluded that in iodide refining of zirconium using the methodology that has been described a very high purity of metal with respect to nonmetallic additions (carbon, oxygen, nitrogen, and hydrogen) can be attained. Besides, it also follows from these data that the mechanism of the transfer of additions during iodide refining that was proposed in the work of Sciefe and Wylie [6] is very close to the truth. However, direct proof can be obtained only by analysis of the gas phase in the hood.

#### BIBLIOGRAPHY

1. Lastmen and Kerts, Metallurgiya tsirkoniya. Gl. V. -- Polucheniye tsirkoniya razlozheniyem iodidov (Metallurgy of Zirconium. Chapter V. -- Obtaining Zirconium by Iodide Decomposition), Moscow, Publishing House of Foreign Literature, 1959.
2. V. S. Yemel'yanov, P. D. Bystrov, and A. I. Yevstyukhin, "Iodide Method of Refining Zirconium", Atomnaya energiya (Atomic Energy), Vol 1, Nr 1, 1956, pages 43-51; Nr 3, 1956, pages 122-131.
3. V. S. Yemel'yanov, P. D. Bystrov, A. I. Yevstyukhin, "Iodide Method of Refining Zirconium", Yubileyny sbornik nauchnykh trudov Moskovskogo inzhenerno-fizicheskogo instituta (Jubilee Collection of Scientific Works of the Moscow Engineering-Physics Institute), Nr 2, Moscow, Publishing House of MIFI, 1957, page 15.
4. A. I. Yevstyukhin, I. P. Barinov, and D. D. Abanin, "Investigation of the Iodide Process of Obtaining Zirconium Using Zirconium Carbide as the Starting Material", Metallurgiya i metallovedeniye chistykh metallov (Metallurgy and Metal Science of Pure Metals), Nr 1, Moscow, Publishing House of MIFI, 1959, page 78.
5. Metody polucheniya chistykh metallov (Methods of Obtaining Pure Metals), Editors: V. S. Yemel'yanov and A. I. Yevstyukhin, Moscow, Publishing House of Foreign Literature, 1957, page 30.
6. D. Sciefe and A. Wylie, Report Nr 1098 presented at the Second International conference on the Peaceful Use of Atomic Energy, Geneva, 1958.

7. Lunem, "Principles of Iodide Refining", Problemy sovremennoy metallur-  
gii (Problems of Modern Metallurgy), Nr 4(52), Moscow, Publishing  
House of Foreign Literature, 1960, page 54.

6306

CSO: 1879-D.

THE EFFECT OF HYDROGEN AND NITROGEN ON THE CORROSION  
RESISTANCE OF ZIRCONIUM IN WATER AND STEAM

V. N. Yemel'yanov  
N. V. Borkov

1. The Effects of Hydrogen

Many papers [1-4] have been devoted to the interaction of zirconium with hydrogen. Many authors have made special studies of the effects of hydrogen on the corrosion resistance of zirconium in water and steam. Hydrogen contained in the metal as an addition before the beginning of the corrosion process and hydrogen which gets into the metal during the corrosion process have an effect on the corrosion resistance of zirconium.

In this paper we are attempting to obtain direct proof of the effect of the hydrogen in the metal on the corrosion resistance of zirconium in a water vapor medium. Therefore, we prepared zirconium specimens with various predetermined amounts of hydrogen and subjected these specimens to corrosion tests. Two series of experiments were conducted in order to obtain more reliable results. In both series the tests were conducted in a water vapor medium at 350°C and a pressure of 170 atmospheres.

Preparation of Specimens

The initial material with iodide zirconium refined in an arc furnace with a consumable electrode and rolled into a sheet 1 mm thick. The typical content of additions in the initial metal is shown in Table 1.

Table 1

## Additions in the Initial Metal

Addition	Content, wt. %	Addition	Content, wt. %
N <sub>2</sub>	0,002	Ni	0,001
O <sub>2</sub>	0,006—0,009	Cr	0,004—0,006
H <sub>2</sub>	0,001	Ti	0,0013—0,0016
Al	0,005—0,009	Mg	0,0006
Si	0,02—0,03	C	0,015—0,08
Fe	0,035—0,075		

Specimens of the first series were prepared on a special die and had the shape and dimensions shown in Figure 1. Specimens of the second series were rectangles 30 x 8 mm.

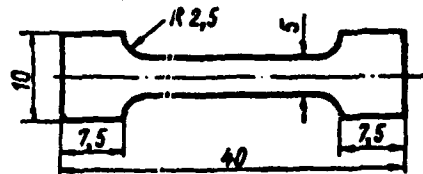


Figure 1. The Shape of the Specimens of Zirconium in the First Series of Tests

Before the specimens were alloyed with given amounts of hydrogen they were given the following preliminary treatment. Each specimen was cleaned with emery paper to remove the oxide film that formed during rolling. A hole 1.5 mm in diameter was drilled in one end of the specimen so that the specimen could be hung in the installation for alloying and later in an autoclave for the corrosion tests. A number was written on the specimen by the electric spark method. Then the specimens were etched in weak hydrofluoric acid (20% HF, 80% H<sub>2</sub>O), washed in tap water and acetone, and dried in air. After this, each specimen was weighed on scales with an accuracy to the fourth power. After this treatment the specimens were considered ready for alloying with hydrogen.

## Equipment for Alloying Zirconium Specimens with Hydrogen

We designed laboratory equipment for alloying zirconium specimens with given amounts of hydrogen. It is a high vacuum system made chiefly of glass and mounted on a vertical lattice support. A drawing of the basics of equipment is given in Figure 2. The following basic assemblies and parts are in the equipment.

1. The reaction chamber (in which the zirconium absorbs the hydrogen) is a quartz hood 11 with a vacuum slide 10. A glass crossbar is welded onto the slide inside the hood. This is used to suspend a long quartz hook 12 on which the zirconium specimen 13 is hung.

2. The measuring assembly which includes a measuring vessel 7 calibrated for the difference in weights in the dry form and filled with distilled water corrected for the density of air; two taps 6 and 8 to limit the volume; a mercury manometer 4; an oil manometer 1; and taps 2, 3, 5, and 14. The mercury manometer is used to make a rough estimate of the hydrogen pressure in this measuring vessel. The surface of the mercury (with a vapor elasticity at normal temperature of  $1 \times 10^{-3}$  mm of mercury) is covered with a small layer of vacuum oil which, under the same conditions, has a vapor elasticity of  $1 \times 10^{-8}$  mm of mercury. The oil manometer, covered with vacuum oil D1, is put into the measuring vessel by opening one of the taps (2 or 3). When this is done the opened elbow of this manometer is filled with hydrogen and the other is under the deep vacuum that was achieved earlier. The use of an oil manometer makes it possible to increase the accuracy of the estimate by 14 times in comparison with a mercury manometer. This is very important when alloying lightweight specimens with small amounts of hydrogen. The pressure of the hydrogen in the measuring vessel can be controlled with an accuracy up to  $5 \times 10^{-2}$  mm mercury.

3. The pumping system consists of two vacuum pumps: a rough vacuum pump (of the VN-461 type) 24 and a diffusion steam-oil pump (of the SDN-1 type) 20; a trap 16; a ballast vessel 22; and taps 15, 18, 19, 21, and 23. By turning on the taps 18, 19, and 21 the vacuum can be created with either one rough pump or two pumps--the rough pump and the diffusion pump--connected in sequence.

4. An instrument for measuring the vacuum of the VIT-1 type (not shown in the drawing) with a thermocouple (of the LT-2 type) 9 and an ionization thermocouple (of the LN-2 type) 17.

5. The system for retaining and releasing the hydrogen into the equipment consists of a flask with hydrogen 29; a reducer 30; a rubber chamber 31 which acts as an indicator of the rate of feed of hydrogen into the equipment; a trap 28 and taps 25 and 27. Using the trap to remove

water vapor and oxygen from the hydrogen that enters equipment makes it possible to avoid these additions.

6. A heating assembly (not shown in the drawing) consists of furnaces with nickel-chromium spirals on the quartz hood; this furnace is fed by a transformer of the type RNO-250-5 and an amperemeter which regulates the current in the furnace.

7. A device for measuring the temperature in the furnace—a thermocouple galvanometer of the MPB-46 type and a Chromel-aluminum thermocouple which forms a hot junction with the bottom of the quartz hood when it is in its working position.

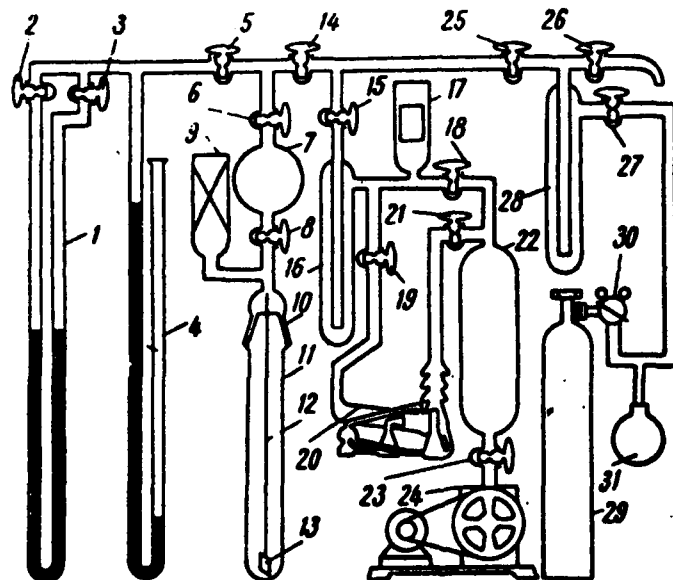


Figure 2. Drawing of the Laboratory Equipment for Alloying Zirconium With Given Amounts of Hydrogen.

Atmospheric air is let into the equipment by the tap 26. The equipment is taken from atmospheric pressure to a pressure of  $1 \times 10^{-1}$  mm of mercury by a rough vacuum pump. Then the diffusion pump is turned on and 25-30 minutes later a vacuum reaches  $1 \times 10^{-4}$ - $8 \times 10^{-5}$  mm of mercury. Using the trap 16 makes it possible to improve the vacuum to  $(1-3) \times 10^{-5}$  mm of mercury.

A well-pumped setup can retain a deep vacuum for a long time. Thus, after 48 hours the vacuum is reduced from  $2 \times 10^{-5}$  mm of mercury to  $1 \times 10^{-4}$  mm of mercury. That is, the leakage was  $1.7 \times 10^{-6}$  mm of mercury per hour. In test runs to check the retention of the vacuum when the hood had a furnace heated to  $700^{\circ}\text{C}$  the leakage in the part of the equipment opened by tap 14 was somewhat greater. Thus, in two hours of holding at this temperature the leakage was  $5 \times 10^{-3} - 2 \times 10^{-2}$  mm of mercury. Consequently, to obtain reliable results when alloying specimens with hydrogen there should be minimum holding time at high temperature, very accurate observation of all the parts of equipment, and thorough observation of all the moving parts of it (the slide, the taps). The laboratory equipment is shown in Figure 3.

### Alloying Zirconium With Hydrogen

The amount of hydrogen necessary for alloying the specimen is calculated using the Mendelejev-Klapeyron equation

$$p = \frac{mRT}{MV}$$

where  $p$  is the pressure of the hydrogen in the measuring vessel in mm of mercury;  $m$  is the weight of the hydrogen necessary to alloy the specimen in grams;  $R$  is the gas constant, 62360 mm of mercury cubic cm per degree;  $P$  is the absolute temperature in degrees kelvin;  $M$  is the molecular weight of hydrogen;  $V$  is the volume of hydrogen in cubic cm (in our case the measuring vessel had a volume of  $V = 73$  cubic cm).

The zirconium specimen 13, prepared for alloying, is hung on the quartz hook 12 in the quartz hood 11 which is firmly pressed against slide 10 by a vacuum well. The tap 26 is closed and the equipment is evacuated by the rough vacuum pump. As the rough vacuum is reached the diffusion steam-oil pump is turned on and a Dewar flask with liquid nitrogen is put on the trap 16.

At the moment when the vacuum is reached in the equipment (including in the mercury manometer and in both elbows of the oil manometer) taps 2, 3, and 5 are opened, a tubular furnace is put on the quartz hood, and the hood is heated to  $800^{\circ}\text{C}$ . Heating at this temperature for 1 hour with continuous pumping is done to degas the specimen and to dissolve the thin oxide film on it. After this roasting the furnace is taken away from the quartz hood, a Dewar flask with liquid nitrogen is put on a trap 28, tap 8 of the measuring vessel is closed, and the intermediate taps 14 and 15 and tap 25 on the trap 28 are closed. By slowly turning tap 27  $180^{\circ}$  hydrogen is fed into trap 28 from the rubber bulb 31.

Thus, the hydrogen in the trap 28 is at atmospheric pressure. Here the oxygen and water vapors are frozen out. Then tap 25 is also turned  $180^{\circ}$ . When this is done part of the hydrogen occupies the volume limited

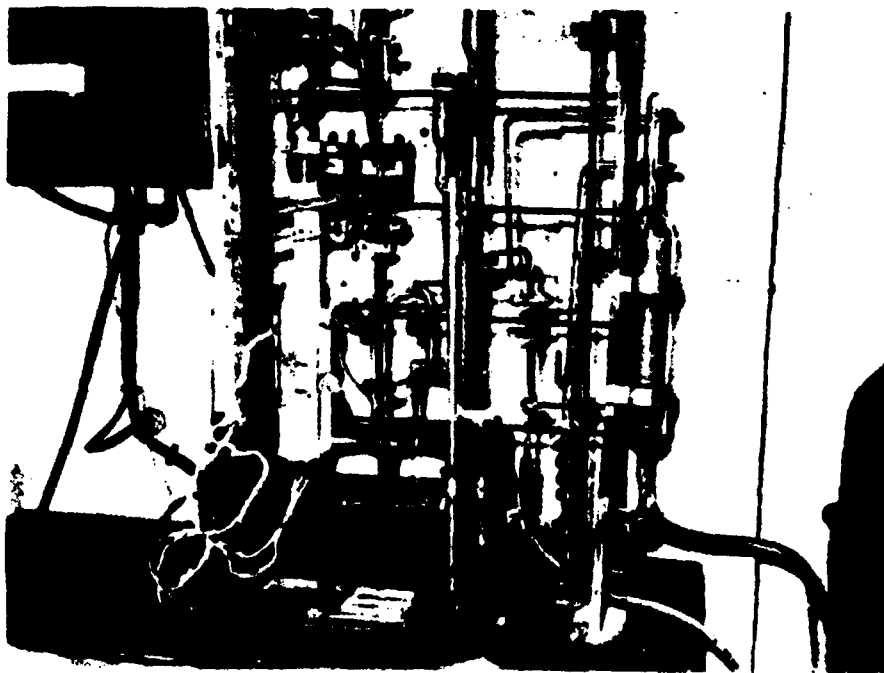


Figure 3. The Laboratory Equipment for Alloying Zirconium With Given Amounts of Hydrogen

by taps 14, 15, and 25 where it is under a pressure below atmospheric pressure. The next turn of taps 14 and 15 opens the passage so that the hydrogen can enter the measuring vessel 7 and the mercury manometer 4 which shows the pressure of the hydrogen in the measuring vessel. Depending on whether or not the pressure of the hydrogen in the measuring vessel is too high or too low, it can be raised or lowered by turning the taps. For better accuracy of estimating pressure an oil manometer 1 opened by one of the taps 2 or 3 is connected to the measuring vessel.

After the hydrogen pressure reaches the right level tap 6 is closed and tap 8 is opened. As a result, the hydrogen enters the quartz hood 11. Now a furnace is once again put on the hood and heating is begun. Meanwhile hydrogen is pumped from the remainder of the equipment (above the closed tap 6).

The furnace is put on the hood so that the specimen is in the center of the furnace. The temperature in the center of the furnace is raised to 680-700° and held at this level for 30-40 minutes. After this time the heating is stopped and the specimen is slowly cooled (with the furnace). At room temperature the residual pressure in the hood is  $6 \times 10^{-3}$ - $1 \times 10^{-2}$  mm of mercury which indicates the practically complete absorption of hydrogen by the specimen.

The data that are characteristic for the process of hydrogen absorption by zirconium are given in Table 2.

It followed from Table 2 that at 700° there is a rapid absorption of hydrogen by the zirconium. Holding at this temperature for 30-40 minutes is sufficient for uniform distribution of hydrogen over the cross section of the specimen. We checked this in a special series of experiments which were controlled by metallographic inspection of specimens alloyed with hydrogen. Figure 4 shows microphotographs of specimens of pure zirconium and zirconium alloyed with hydrogen.

Table 3 gives the results of chemical analysis for hydrogen content in zirconium specimens alloyed by the described method. There is very close agreement between the results of the analysis and the desired amounts of alloying.

Table 2

Typical Process of Hydrogen Absorption by a  
Zirconium Specimen Weighing 1 Gram

Time, minutes	Hydrogen Pressure in Quartz Hood, mm of mercury	Furnace Temperature, °C	Remarks
0 5	$1 \cdot 10^{-4}$ 8.5	20 20	This pressure was observed in the measuring vessel. After the tap between the measuring vessel and the hood was opened the pressure was lowered. The furnace was turned on.
15	$1 \cdot 10^{-1}$	680	The beginning of hydrogen absorption by the specimen was read from the vacuumeter.
20	$8 \cdot 10^{-2}$	700	=
25	$2 \cdot 10^{-2}$	700	The heating current of the furnace was turned on; Stands with the furnace.
50	$1 \cdot 10^{-2}$	700	
70	$6 \cdot 10^{-3}$	20	

Table 3

The Results of Chemical Analysis of Zirconium  
Specimens Alloyed With Hydrogen

Specimen No.	Amount of H <sub>2</sub> in the Specimen After Alloying, wt. %	
	Predicted (considering H <sub>2</sub> in starting metal)	From Results of Chemical Analysis
1	Исходный металл	0,0018
2	0,0028	0,0023
3	0,0048	0,0042
4	0,0068	0,0059
5	0,008	0,0074
6	0,01	0,0101
7	0,015	0,0127
8	0,02	0,0165



Figure 4. Microphotographs of Zirconium Specimens: a--specimen of pure zirconium annealed at  $t = 800^{\circ}$  for 1 hour (X600); b--a zirconium specimen alloyed with hydrogen in an amount of 0.01 weight % (X136). The uniform distribution of the hydrides is evident.

Corrosion Tests of the First Series of Zirconium Specimens With Different Hydrogen Content

Zirconium specimens alloyed with hydrogen using the described methodology were subjected to corrosion tests in a steam atmosphere. Three groups of specimens with the following hydrogen content (%) were tested in the series: 0.001 (initial metal), 0.01, and 0.015. Each group consisted of three specimens.

The specimens were hung on hooks of a special suspension made from stainless steel 1 KH18N9T and were placed in an autoclave of the same steel. Twice-distilled water was poured into the autoclave in an amount that was calculated, at a test temperature of 350°, to create a pressure in the autoclave of 170 atmospheres. The water was changed every week. After certain time intervals, 100, 200, 440, 670, and 925 hours, the specimens were taken from the autoclave, examined, and weighed, the kinetics of the corrosion process were determined from the weight of the specimens. Average data on this test are given in Table 4.

Table 4

Average Data on the Weight of Zirconium Specimens in Time

Hydrogen Content in Specimens, wt. %	Average Weight Gain (mg/decimeter <sup>2</sup> ) in time				
	100 hours	200 hours	440 hours	670 hours	925 hours
0.001	3.16	5.8	9.44	11.8	16.28
0.01	17.85	25.0	27.3	28.4	38.3
0.015	25.7	28.0	39.4	39.4	52.0

On the basis of the data in this table curves of the corrosion process were drawn in the coordinates weight-time. These curves are shown in Figure 5. They show that zirconium's corrosion resistance is reduced as the hydrogen content is increased.

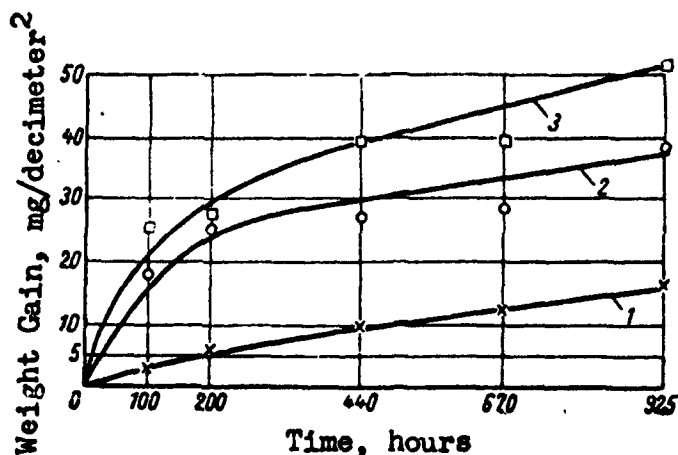


Figure 5. Corrosion of Specimens With Different H<sub>2</sub> Content.  
 Medium -- twice-distilled water at  $t = 350^{\circ}\text{C}$  and  $p = 170\text{ atm}$ :  
 1 -- Zr + 0.001 wt. % H<sub>2</sub>; 2 -- Zr + 0.01 wt. % H<sub>2</sub>; 3 -- Zr +  
 + 0.015 wt. % H<sub>2</sub>.

#### Corrosion Tests of the Second Series of Zirconium Specimens With Various Hydrogen Contents

In these experiments the corrosion medium and the test procedure were the same as for the specimens of the first series. However, there were some differences in the conduct of the experiment. First, each specimen was tested in a separate ampule made from stainless steel 1Kh18N9T. The working volume of the ampule was 6 cubic cm. The ampule was sealed by using a "ball on cone" seal. Second, the test lasted considerably longer. Four groups of specimens with hydrogen contents of 0.005, 0.01, 0.02, and 0.025 weight % were tested. Each group had five specimens. The examination and weighing of the specimens was done after 250, 500, 1000, 1500, 2000, and 2500 hours. All of the specimens showed high absolute corrosion resistance and the tests were not stopped because the specimens failed. Their external appearance was of very good quality. However, their relative corrosion resistance, which we judged as in the preceding case from the corrosion kinetics of an increase in the weight of the specimens, showed the same pattern as in the first series of tests. That is, an increase in the hydrogen content in the zirconium reduced its corrosion resistance.

Average data on the increase in the weight of the specimens during the corrosion process are given in Table 5.

Table 5

## The Average Data on the Weight of Zirconium Specimens in Time

Hydrogen Content in Specimens, wt. %	Average Weight Gain					
	250 hours	500 hours	1000 hours	1500 hours	2000 hours	2500 hours
0.005	3.63	8.5	16.1	17.6	18.2	19.2
0.01	4.36	10.9	18.9	20.3	22.7	25.9
0.02	4.84	10.0	20.9	22.5	26.7	28.78
0.025	4.98	11.8	22.52	24.5	27.3	30.3

These data were used to plot curves of the corrosion process in logarithmic coordinates. The curves are seen in Figure 6. These curves also show that the hydrogen present in the zirconium has a negative effect on the corrosion resistance of this metal in a steam vapor.

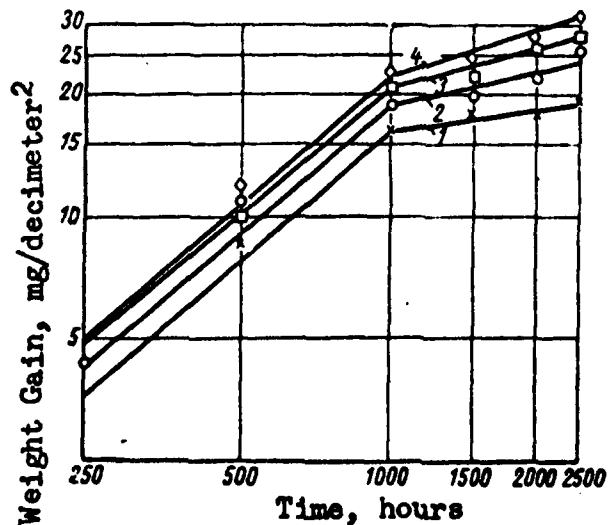


Figure 6. Corrosion of Zirconium Specimens With Varying Hydrogen Content. Corrosion medium--twice distilled water at  $t = 350^{\circ}$  and  $p = 170$  atm; 1--Zr + 0.005 wt.% H<sup>2</sup>; 2--Zr + 0.01 wt.% H<sup>2</sup>; 3--Zr + 0.02 wt.% H<sup>2</sup>; 4--Zr + 0.025 wt.% H<sup>2</sup>.

## 2. The Effect of Nitrogen

Literature [1, 2, 5, 6 and others] shows that a number of elements present in zirconium as additions noticeably reduce the corrosion resistance of zirconium in a steam atmosphere. Such elements are carbon, titanium, nitrogen, and others. Nitrogen especially reduces the corrosion resistance of zirconium. Additions of certain elements, for example, iron, chromium, nickel, tin, have a positive effect on the corrosion resistance of zirconium; they can reduce the harmful effect of other additions.

It seemed advisable to study the corrosion resistance of unalloyed zirconium with additions characteristic for metal of domestic production in relation to the nitrogen content. Zirconium refined by the iodide method, remelted in an arc furnace in an inert gas, and rolled into a strip 0.75-1.0 mm thick was the initial material.

Table 6 shows the typical chemical composition of the metal alloyed with nitrogen in different amounts and then subjected to corrosion tests in steam.

The specimens for the corrosion tests were rectangles 30x10 mm. Each specimen was alloyed with nitrogen in a predetermined amount ranging from 0.006 to 0.055 wt.%. The alloying was done in the laboratory equipment using the methodology described in the paper by N. V. Borokov [7].

Table 6

The Typical Chemical Composition of  
Initial Zirconium Specimens

Element	Content, wt. %	Element	Content, wt. %
Hf	0.045	Si	0.015
W	<0.004	Fe	0.015
Ni	<0.001	Ti	0.002
Cr	<0.003	C	0.05
K	<0.003	Cu	0.0013
Ca	<0.005	O <sub>2</sub>	0.06

The corrosion tests were made in twice-distilled water which was poured into small ampules from stainless steel 1Kh18N9T with a working volume of 6 cubic cm. Each ampule contained one specimen. Several series of specimens were tested under different conditions:  $t = 300^{\circ}$  and  $p = 88$  atmospheres;  $t = 350^{\circ}$  and  $p = 170$  atmospheres;  $t = 400^{\circ}$  and  $p = 280$  atmospheres. Three specimens in each series were tested for each nitrogen content.

The corrosion resistance was evaluated from the change in the external appearance and chiefly by the change in the weight of the specimens. The tests were stopped when a white fluffy oxide film formed on the specimens. Tables are given below of the change in the weight of zirconium specimens with various nitrogen contents during corrosion tests under the indicated conditions. The kinetic curves of the corrosion process, plotted using these data, are also given. The specimens were taken out and weighed after the time intervals indicated in the tables. The nitrogen content in the test specimens is also shown.

The specimens with a nitrogen content of 0.006 wt.% after 2000 hours of testing were in good condition with a dark firm oxide film. On the basis of the results collected in Table 7 curves were plotted in logarithmic coordinates. The curves are shown in Figure 7.

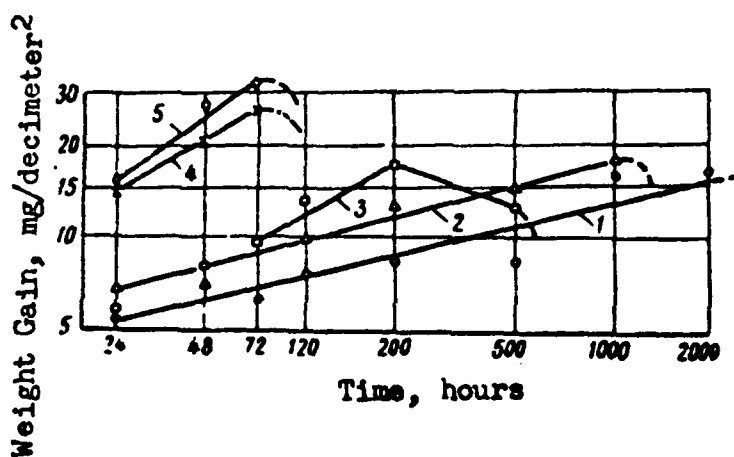


Figure 7. Corrosion of Zirconium Specimens Containing Nitrogen in a Steam Atmosphere at  $t = 300^\circ$  and  $p = 80$  atmospheres: 1--Zr + 0.006 wt.% N<sub>2</sub>; 2--Zr + 0.015 wt.% N<sub>2</sub>; 3--Zr + 0.025 wt.% N<sub>2</sub>; 4--Zr + 0.045 wt.% N<sub>2</sub>; 5--Zr + 0.055 wt.% N<sub>2</sub>.

We conducted a repetition of the experiment to determine the effect of nitrogen on the corrosion resistance of zirconium under the same testing conditions but with another series of specimens with a nitrogen content of 0.007, 0.015, 0.02, and 0.03 wt.%. The results were similar to those in Table 7 and in Figure 7. The specimens with a nitrogen content of 0.007 wt.% were tested for 4000 hours and showed no signs of failure after this time. Specimens with a nitrogen content of 0.015 wt.% were covered with a fluffy white film just as in the first case and were taken out of the test after 1000 hours. Specimens with a nitrogen content of 0.02 and 0.03 wt.% had very poor corrosion resistance (they were taken out of the tests after 200 and 100 hours respectively).

Table 7

Average Values of the Weight of Zirconium Specimens per Unit of Surface During Tests at  $t = 300^\circ$  and  $p = 88$  atmospheres.

Nitrogen Content in Specimens wt. %	Average Weight Gain (in mg/decimeter <sup>2</sup> ) in Time							
	24 hours	48 hours	72 hours	120 hours	200 hours	500 hours	1000 hours	2000 hours
0.006	5.4	—	6.16	7.70	8.50	8.50	16.17	16,2
0.015	6.92	6.92	—	10.00	13.00	14.60	17.70	Film crumbles; Specimens taken out of tests
0.025	5.4	8.16	9.68	13.22	17.41	13.10		Film crumbles; Speci- mens taken out of tests
0.045	14.30	21.00	26.60					Film crumbles; Specimens taken out of tests
0.055	15.37	26.95	32.30					Film crumbles; Specimens taken out of tests

Specimens of the third series contained 0.007, 0.02, and 0.03 wt.% nitrogen; specimens in the fourth series contained 0.007, 0.015, 0.025, and 0.045 wt.% nitrogen. Both series were tested at  $350^\circ$  under a pressure of 170 atmospheres. The tests showed that the corrosion resistance of the specimens under these conditions was lowered. Table 8 gives the average values of the weight of specimens of the third series per unit of surface.

Table 8

Average Values of the Weight of Zirconium Specimens per Unit of Surface During Tests at  $t = 350^\circ$  and  $p = 170$  atmospheres.

Nitrogen Content in Specimens, wt. %	Average Weight Gain (in mg/decimeter <sup>2</sup> ) in Time						
	24 hours	50 hours	100 hours	150 hours	200 hours	250 hours	450 hours
0,007	6	13	16	23	23	23	Film crumbles; specimens taken out of tests.
0,02	14	37	33	Film crumbles; specimens taken out of tests.			
0,03	54	Film crumbles; specimens taken out of tests.					

Curves were plotted from these data in logarithmic coordinates. They are shown in Figure 8.

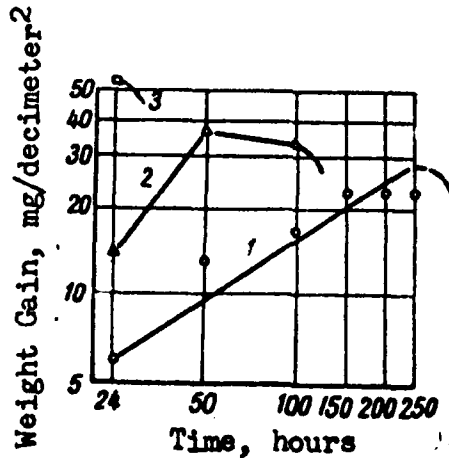


Figure 8. The Corrosion of Zirconium Specimens Containing Nitrogen in a Steam Atmosphere at  $t = 350^\circ$  and  $p = 170$  atmospheres: 1--Zr + 0.007 wt.% N<sub>2</sub>; 2--Zr + 0.02 wt.% N<sub>2</sub>; 3--Zr + 0.03 wt.% N<sub>2</sub>.

The fifth series of specimens were given a more severe test: temperature 400° and pressure 280 atmospheres. The specimens had a nitrogen content of 0.007, 0.015, 0.02, and 0.03 wt.%. As seen from Table 9 and Figure 9 in such tests the specimens have no corrosion resistance because even at a minimal nitrogen content (0.007 wt.%) the film begins to flake off after 100 hours. Specimens with higher nitrogen concentrations did not last 24 hours.

Table 9

Average Values of the Weight of Zirconium Specimens per Unit of Surface During Tests at  $t = 400^\circ$  and  $p = 280$  atmospheres.

Nitrogen Content in Specimens, wt. %	Average Weight Gain (in mg/decimeter <sup>2</sup> ) in Time			
	24 hours	50 hours	100 hours	150 hours
0,007	28	46	78	Film crumbles; specimens taken out of tests.
0,015	143	Film crumbles; specimens taken out of tests.		
0,02	163	"		
0,03	202	"		

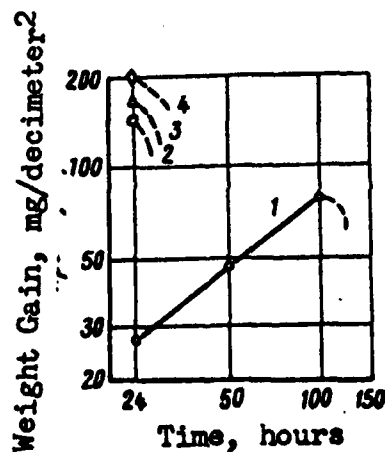


Figure 9. The Corrosion of Zirconium Specimens Containing Nitrogen in a Steam Atmosphere at  $t = 400^\circ$  and  $p = 280$  atm: 1--Zr + 0.007 wt.% N<sub>2</sub>; 2--Zr + 0.015 wt.% N<sub>2</sub>; 3--Zr + 0.02 wt.% N<sub>2</sub>; 4--Zr + 0.03 wt.% N<sub>2</sub>.

## Conclusions

1. It was shown that it is possible using the equipment and methodology described in this paper to obtain zirconium specimens with different preassigned hydrogen contents.
2. It was also shown that an increase in the hydrogen content in the zirconium specimens reduces its corrosion resistance in a steam atmosphere.
3. The corrosion resistance of zirconium is sharply reduced with an increase in the nitrogen content in it.
4. In an atmosphere of superheated steam at  $t = 400^{\circ}$  and  $p = 280$  atmospheres zirconium containing 0.007 wt.% nitrogen and more is not a corrosion-resistant material since even with a nitrogen content of 0.007 wt.% specimens did not withstand tests lasting more than 100 hours.
5. In a steam atmosphere at  $t = 350^{\circ}$  and  $p = 170$  atmospheres zirconium containing 0.007 wt. % nitrogen and more also is not a corrosion-resistant material although the testing time for specimens containing 0.007 wt. % nitrogen was somewhat increased.
6. In a steam atmosphere at  $t = 300^{\circ}$  and  $p = 88$  atmospheres the corrosion resistance of zirconium with small additions of nitrogen is considerably higher: specimens with 0.015 wt.% nitrogen withstood tests lasting 1000 hours and specimens with 0.007 wt.% nitrogen lasted 4000 hours.
7. Nitrogen reduces corrosion resistance much more than hydrogen.

## BIBLIOGRAPHY

1. R. S. Ambartsumyan and others, "Mechanical Properties and Corrosion Resistance of Zirconium and Its Alloys in Water, Steam, and Gases at Elevated Temperatures", Trudy Vtoroy mezhdunarodnoy konferentsii po mirnomu ispol'zovaniyu atomnoy energii (Transactions of the Second International Conference on the Peaceful Use of Atomic Energy), Geneva, 1958, Vol 3 -- Nuclear Fuel and Reactor Metals, Moscow, Atomizdat, 1959, page 486.
2. B. Lastman and F. Kerz, Metallurgiya tsirkoniya (Metallurgy of Zirconium), Moscow, Publishing House of Foreign Literature, 1959.
3. C. M. Schwartz and M. W. Mallett, Transactions of the American Society of Metals, Vol 46, 1954, pages 640-654.

4. M. A. Tolstaya and others, "Investigation of the Mechanism of Corrosion of Zirconium Alloys Alloyed With Niobium in High Purity Water", Korroziya reaktornykh materialov (Corrosion of Reactor Materials), Moscow, Atomizdat, 1960, page 250.
5. G. L. Miller, Tsirkoniy (Zirconium), Moscow, Publishing House of Foreign Literature, 1955.
6. Tomas, "Corrosion of Zirconium and Its Alloys in Water at Elevated Temperatures", Doklady inostrannykh uchenykh na Mezhdunarodnoy konferentsii po mirnomu ispol'zovaniyu atomnoy energii (Zheneva, 1955). V Kn.: Metallurgiya yadernoy energetiki i deystviye oblucheniya na materialy (Papers of Foreign Scientists at Second International Conference on Useful Use of Atomic Energy (Geneva, 1955)). In the book: Metallurgy of Nuclear Energy and the Effect of Radiation on Materials, Moscow, Metallurgizdat, 1956, page 376.
7. N. V. Borkov, "Laboratory Equipment for Obtaining Zirconium Alloys With Slight Additions of Nitrogen and Oxygen", Metallurgiya i metalovedeniye chistykh metallov (Metallurgy and Metal Science of Pure Metals), Nr II, Moscow, Atomizdat, 1960, page 148.

6306

CSO: 1879-D

THE FORMATION OF SCALE WITH A STRUCTURE  $6ZrO_2 \cdot Nb_2O_5$   
ON ALLOYS OF ZIRCONIUM WITH NIOBIUM

Yu. F. Bychkov  
V. A. Ivanov  
A. N. Rozanov

The heat resistance of zirconium and its alloys and also of niobium alloys has been studied by a number of researchers. Most alloying elements reduced the oxidation resistance of zirconium. However, certain additions, for example, Fe, Ni, Cr, Cu, Ag introduced in an amount less than 1 at.%, somewhat improved the heat resistance of iodide zirconium. However, they do form low melting eutectics [1, 2]. Niobium and tantalum in an amount up to 0.25% increase the heat resistance of iodide zirconium. In larger amounts they reduce the heat resistance [1].

At present several heat resistant and scale resistant in water zirconium alloys have been developed and are being used in water-cooled nuclear reactors: the well-known Zircaloy-2 containing 1.2-1.7% Sn, 0.07-0.2% Fe, 0.05-0.15% Cr, and 0.03-0.08% Ni; the alloy that is less used, Zircaloy-3 containing 0.15-0.5% Sn, 0.25% Fe, and the remaining additions the same as in Zircaloy-2; the recently created Zircaloy-4 containing 1.2-1.7% Sn, 0.12-0.18 Fe, 0.05-0.15% Cr and less than 0.002% Ni; Ozhennite containing 0.1-0.3% Sn, 0.1-0.3% Fe, 0.1-0.3% Ni, and 0.1-0.3% Nb, and finally the alloy N-1 with 1% Nb [2, 3]. Binary alloys with 0.5% Ta and W have also been recommended. All these low-alloyed alloys have comparatively low heat resistance close to the heat resistance of zirconium.

Recently attention has been given to the development of more heat-resistant alloys of zirconium with an increased content of alloying elements. Interest is being shown in the highly-alloyed Zr-Nb alloys. For example, when studying the scale resistance in air at 300, 400, and 500°C of alloys of the Zr-Nb system annealed for 24 hours at 500°C after quenching from the beta-region it was revealed [1] that the minimum

addition in weight of these alloys of the system was the alloy with 25% Nb. This alloy was equivalent to zirconium with respect to heat resistance at 400° or was better than it. The weight addition for this alloy after 300-hour soaking at 400° was less than 1 mm/sq cm and for alloys containing about 10% Nb it was 3 mm/sq cm. Alloys containing 10-20% Nb also showed high scale resistance in long-time tests in water at 400°C [1].

It was shown still earlier [4] that alloys containing 12-20% Nb have considerably higher scale resistance in air at 570°C than alloys with 2-7% Nb. When the Nb content in the alloys with zirconium is increased above 25% the heat resistance is lowered.

The scale resistance of alloys Zr-Nb on a niobium base (up to 45 wt.% Zr) was studied at 1000 and 1200°C [5]. Additions of up to 20% Zr greatly increase the linear rate of oxidation of Nb at 1000°C, but reduce it at 1200°C. Alloys of Nb with 25-45% Zr had 2-5 times less addition of weight than Nb under the same conditions; but they oxidize more strongly.

The authors of reference [5] think that in alloys of Nb with small amounts of Zr the oxidation rate increases as a result of a large size of the zirconium ions and the lower valence of zirconium in comparison with niobium which cause a reduction in the stability of Nb<sub>2</sub>O<sub>5</sub> and an increase in the rate of diffusion of oxygen through the Nb<sub>2</sub>O<sub>5</sub>.

The corrosion of alloys of zirconium with different contents of niobium (from 2 to 80 wt.%) in a current of water vapor at atmospheric pressure and at temperatures of 300, 350, 400, 450, and 500°C was studied [6]. The alloys containing 20-50 wt.% Nb were better than the Zircalloy-2 in corrosion resistance at temperatures above 400°C.

Thus, in several works data have been obtained that agree with respect to the high heat resistance of Zr-Nb alloys containing 20-30% Nb and it is admitted that these alloys merit further study due to their higher heat resistance. In the works referenced above, with the exception of the work of Klopp and others [5], relating to alloys whose compositions are far from optimal with respect to heat resistance, data on the structure and properties of oxide films formed on these alloys are not given.

As is known [2], in the oxidation of zirconium and its low alloyed alloys in air and in oxygen zirconium dioxide film forms on the surface. At temperatures below 1000°C a modification of the dioxide with a single-wedge lattice is formed and at temperatures above 1000°C a mixture of the modification with tetragonal and a single-wedge structure is formed [2]. It is indicated in the work of Klopp and others [5] that the scale that formed in the Zr-55% Nb alloy during oxidation at 1000 and 1200°C contained some amount of 6ZrO<sub>2</sub> x Nb<sub>2</sub>O<sub>5</sub> and ZrO<sub>2</sub> in addition to Nb<sub>2</sub>O<sub>5</sub>.

## Research Methodology

In this work there is an x-ray investigation of the oxide film that forms at 600-1200°C in air on the surface of the two alloys of zirconium Zr-25% Nb and Zr-15% Nb-10% Mo which have high scale resistance compared with the heat resistance of zirconium. Certain properties of the ternary alloy of zirconium with 15% Nb and 10% Mo are given in the article of Yu. F. Bychkov and others [7]. It should be noted that the niobium content in the alloy of Zr with 25% Nb corresponds to the niobium content in the compound  $6\text{ZrO}_2 \times \text{Nb}_2\text{O}_5$  of stoichiometric composition.

The initial materials for melting the specimens were iodide zirconium (99.5% Zr) and pieces of niobium and molybdenum of technical purity. From these materials alloys of Zr-25% Nb and Zr-15% Nb-10% Mo were prepared with ten ingots of each composition and also ingots of zirconium. All the ingots weighed about 30 grams. Melting was done in an arc furnace MIFI-9-3 in an argon atmosphere in a copper water-cooled bottom. To achieve homogeneity the alloys were remelted three or four times during the melting. The ingots in which the structure of the oxide formed at 600°C was studied were rolled at about 900°C into a sheet about 2 mm thick. The other specimens were studied in the cast state. Disks about 20-25 mm in diameter and about 4 mm high were cut out of the ingots. The surface of the specimens was polished.

To obtain a sufficiently thick oxide film at 600°C the specimens were held in air more than 24 hours, at 800°C they were held 20 hours and at 1000 and 1200°C they were held 5 and 3 hours respectively. The different lengths of holding at the various temperatures was caused by the need of obtaining sufficient amount of oxide film. The black oxide film obtained at 600 and 800°C was taken off by etching the base metal (alloys and also the zirconium) in a 50%-hydrofluoric acid. The white scale formed at 1000 and 1200°C was separated mechanically without etching. The scale was crushed into a powder.

The x-ray photographs were taken in a camera RKD-57 on a  $\text{CuK}\alpha$  radiation with a nickel filter. The photography was done with the following parameters: 25 kw, 10 milliamps, 3-6 hours. The x-ray photographs were measured on a comparer. The intensity of the lines was measured on a microphotometer MF-4. The intensity of the line was evaluated using a five-point system.

The fine black oxide film in an atmosphere of oxygen at 1200°C was obtained as follows. The specimens were washed in acetone and placed into a quartz hood. After evacuation and filling the hood with argon to a pressure of 250 mm of mercury it was placed in a tubular furnace heated to 1200°C. After holding for 10 minutes in the hood a mixture of oxygen with argon with portions of oxygen every 25 cubic cm was pumped into the hood. The argon created favorable conditions for slow approach of the oxygen to the surface of the specimen as a result of which the resulting film was

homogeneous. Without preintroduction of argon the specimen oxidized nonuniformly. After the oxygen was fed in the hood with the specimen was held in the furnace for two minutes and cooled in air. As a result of oxidation in oxygen the addition in weight of the specimens was 0.5-1 milligrams per square centimeter.

The black oxide film in air was obtained in a similar way but argon was not fed into the hood; the pressure of air in the hood at the moment of oxidation was 1 atmosphere. As the process of feeding air into the hood was finished the hood was taken from the furnace and cooled in air.

For kinetic investigations the specimens were weighed and put into porcelain crucibles. The crucibles were tightly covered with lids of stainless steel and were placed on a support of steel for oxidation in a muffle furnace MP-2 heated to 700°C. The temperature in the furnace was regulated by a temperature regulator MRShchPr-54. During the oxidation process the specimens were weighed on analytical scales every hour. We also investigated the compound  $6\text{ZrO}_2 \times \text{Nb}_2\text{O}_5$ . This compound was melted from powders of  $\text{ZrO}_2$  and  $\text{Nb}_2\text{O}_5$  in the following manner. First, buttons of  $\text{ZrO}_2$  and  $\text{Nb}_2\text{O}_5$  were placed in an arc furnace which were then melted in a proportion of 6:1. Niobium Pentoxide was obtained as a result of oxidation of the metallic niobium in air. The  $\text{ZrO}_2$  powder that was used to make the compound was of technical purity.

#### A Discussion of the Results

As indicated above, the separation of the oxide film from the specimens oxidized at 600 and 800°C was done by dissolving the specimens in hydrofluoric acid. The possibility of using this etching agent was checked in zirconium. Zirconium specimens oxidized at 600 and 800°C were held in acid until the metal was completely dissolved. There remained a powder-like black oxide which did not dissolve in the acid. The structure of these powders coincided with the single-wedge structure of technically pure  $\text{ZrO}_2$  powder (Figure 1). Some lines on the x-ray photos correspond to the tetragonal modification. The lack of a noticeable effect of the acid on the zirconium oxide was confirmed by the following experiment: the powder of white zirconium oxide after 2.5 hours holding in acid in which there was simultaneously dissolved metallic zirconium changed its weight by only 0.0045 grams (by 1.5%).

In the oxidation of the specimens there is first formed a homogeneous black dense film and a parabolic relation of the weight to time is observed. After the break on the oxidation curve a white oxide film appears which corresponds to the beginning of accelerated oxidation.

The structure of the scale that forms on alloys Zr-25% Nb and Zr-15% Nb-10% mo depends upon the temperature of oxidation in air. At 600°C the basic oxidation product of these alloys is a black film consisting of

zirconium oxide in the single-wedge modification (Figure 2). The white scale which formed on the alloy Zr-4.5% Nb-5% Ti after oxidation at 600°C for 145 hours that was separated mechanically also consisted practically only of ZrO<sub>2</sub>. Thus, the white and the black oxide films that form on the alloys Zr-Nb at 600°C consist of ZrO<sub>2</sub> and contain only a small amount of the new phase (see Figure 2). It can be concluded from this that the high heat resistance of alloys Zr-25% Nb at 400-500°C is not due to the formation of a new productive oxide film but to other unknown factors.

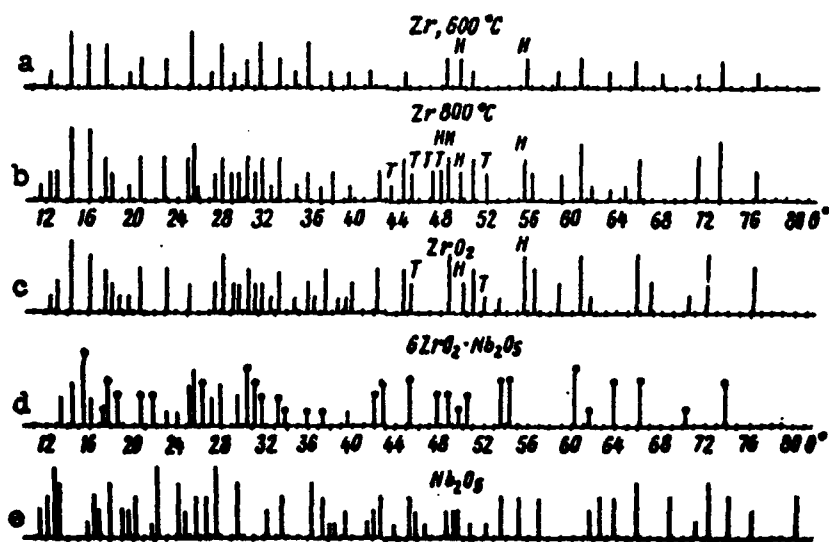


Figure 1. Lines on the X-Ray Photographs of the Oxidation Products of Zr at 600 and 800°C (a, b) of a Technical Zirconium Oxide (c), a Cast Compound  $6\text{ZrO}_2 \times \text{Nb}_2\text{O}_5$  (d) and Niobium Oxide (e). (H-ZrN, T—tetragonal modification of ZrO<sub>2</sub>)

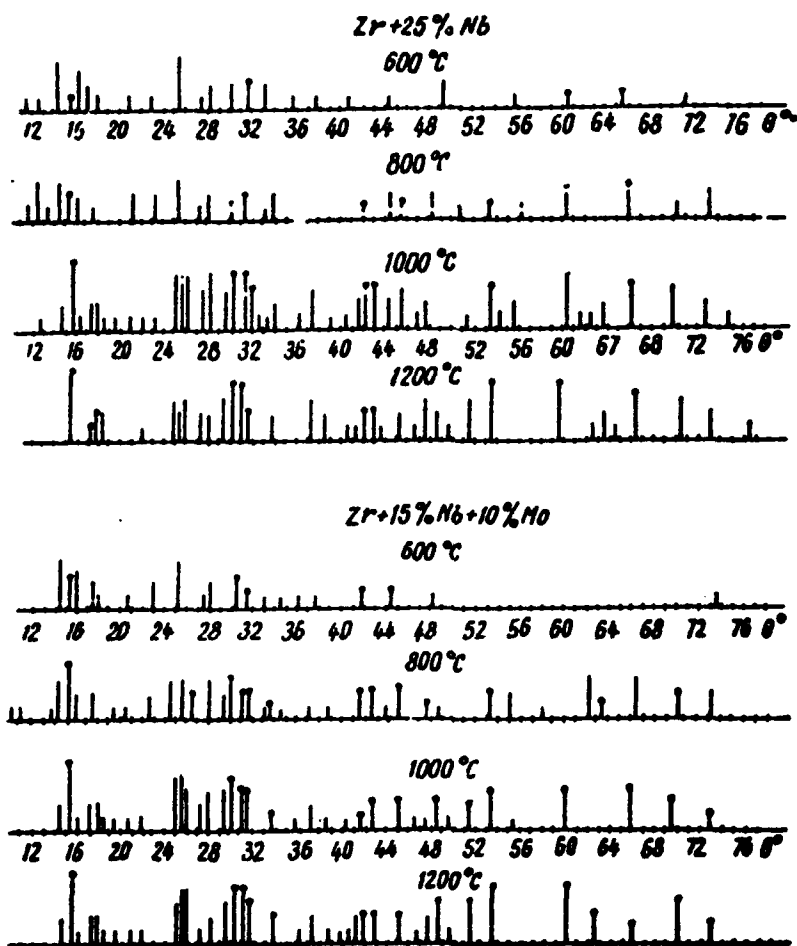


Figure 2. X-Ray Photographs of Oxide Films Formed on Alloys of Zr-25% Nb and Zr-15% Nb-10% Mo During Oxidation in Air at 600, 800, 1000, and 1200°C.

Upon an increase in the oxidation temperature from 600 to 1200°C the amount of ZrO<sub>2</sub> in the scale drops and the amount of the new phase differing from ZrO<sub>2</sub> and from Nb<sub>2</sub>O<sub>5</sub> increases (see Figures 2 and 3). Inasmuch as the new phase has a different structure from a zirconium oxide and from the niobium oxide it can be assumed that it is a complex compound of these oxides. In studying the phase diagrams of the alloy ZrO<sub>2</sub>-Nb<sub>2</sub>O<sub>5</sub> [8] the compound 6ZrO<sub>2</sub> x Nb<sub>2</sub>O<sub>5</sub> on the basis of which the region of limited

solid solutions is formed was revealed. This compound melts at 1670°C.

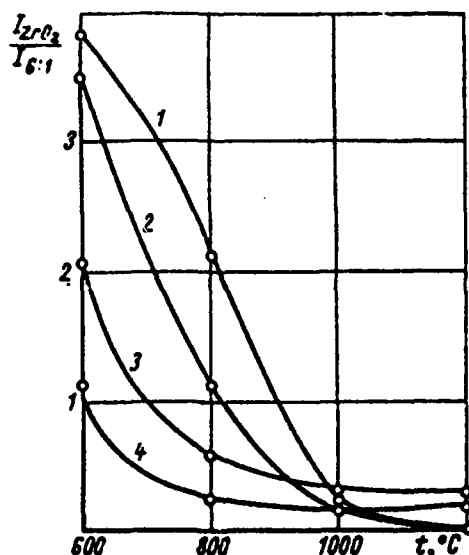


Figure 3. The Relation of the Intensity of Two Lines  $ZrO_2$  ( $d = 3.194$  and  $2.857$  Å) to the Intensity of Lines  $6ZrO_2 \times Nb_2O_5$  ( $d = 2.982$  Å) to the Temperature of Oxidation of the Alloys: 1, 2--for Alloy Zr-25% Nb; 3, 4--for Alloy Zr-15% Nb-10% Mo.

Rot and Kofanur [8] investigated the structure of this compound and determined the interplanular distances. The interplanular distances for the compound  $6ZrO_2 \times Nb_2O_5$  which we melted (see table) coincide with the values given in the work of these authors [8] except for several lines relating to  $ZrO_2$  which can be due to a deviation in the composition of the alloy from the stoichiometric composition during melting. The interplanular distances for the new phase that forms during oxidation of alloys Zr-Nb and Zr-Nb-Mo at high temperatures coincide with the interplanular distances for the melted compound which is seen from a comparison of Figures 1 and 2.

Table of Interplanar Distances for Compounds  
of  $6\text{ZrO}_2 \times \text{Nb}_2\text{O}_5$  Melted in an Arc Furnace

N	d, Å	l	N	d, Å	l	N	d, Å	l
1	0.803	3	15	1.162	2	29*	1.852	3
2	0.821	1	16*	1.222	1	30	1.929	1
3	0.845	3	17	1.290	1	31	2.009	1
4	0.861	3	18	1.328	1	32	2.101	2
5	0.880	1	19	1.401	1	33	2.227	2
6	0.893	4	20	1.430	2	34	2.492	2
7	0.954	3	21	1.480	2	35	2.598	3
8	0.965	3	22	1.512	3	36	2.662	1
9	0.991	2	23	1.553	4	37*	2.866	2
10	1.015	1	24*	1.588	2	38	2.995	5
11	1.031	2	25*	1.669	3	39*	3.178	3
12	1.048	2	26*	1.713	2	40	3.438	2
13	1.094	3	27	1.775	3			
14	1.144	3	28*	1.817	4			

\*  $\text{ZrO}_2$  lines.

The amount of the compound  $6\text{ZrO}_2 \times \text{Nb}_2\text{O}_5$  increases with an increase in the oxidation temperature and at  $1200^\circ\text{C}$  for the alloy Zr-25% Nb it is close to 100%. The ratio between the amounts of  $\text{ZrO}_2$  and  $6\text{ZrO}_2 \times \text{Nb}_2\text{O}_5$  in the scale can be judged from the ratio of the intensities for the lines that are close together and are stronger for these phases (see Figure 3). From the data in Figure 3 it can be concluded that at  $1200^\circ\text{C}$  a sufficiently oxidized alloy contains a maximum amount of the new phase and at lower temperatures the scale contains considerable amounts of  $\text{ZrO}_2$ . In view of the fact that the compound  $6\text{ZrO}_2 \times \text{Nb}_2\text{O}_5$  has no transformations and is refractory (melts at about  $1670^\circ\text{C}$ ), we assumed that the oxide film corresponding in composition to this compound will have better protective properties than the films with a different structure. It was also assumed that such a film can be obtained at high oxidation temperatures.

To evaluate the protective properties of the films that form at high temperature oxide films were obtained on specimens in an atmosphere of oxygen and also in air at  $1200^\circ\text{C}$  using the method described above and the kinetics of oxidation at  $700^\circ\text{C}$  of the initial and at  $1200^\circ\text{C}$  of the pre-oxidized alloys was studied.

The results are given in Figures 4 and 5 from which it is seen that the alloy Zr-15% Nb-10% Mo in the initial state and also after pre-oxidizing

is close with respect to heat resistance to the alloy Zr-25% Nb (the weight values are practically the same). The kinetic curves of oxidation at 700°C for different melts of the same composition are not identical and the weights are somewhat scattered which, probably, is due to the specimens having different contents of additions.



Figure 4. Oxidation Kinetics of Alloy Zr-25% Nb in Air at 700°C; 1, 2—Specimens Pre-Oxidized in Air; 1', 2'—Specimens Pre-Oxidized in Oxygen; 1'', 2''—Specimens Without Preliminary Oxidation.

Preliminary oxidation of any of the specimens at 1200°C always increases the scale resistance. The weights in this case were lower than without preliminary oxidation.

In Figure 4, in which the kinetic curves for alloy Zr-25% Nb are given, it is seen that the oxidation of specimen No. 1 in the initial state (Curve 1'') first occurs according to the parabolic law and after about 3 hours there is a break—acceleration of corrosion. The same specimen after preliminary oxidation in oxygen (Curve 1') and in air (Curve 1) oxidized according to the parabolic law for a longer time (6 hours and more) and had less of an increase in weight. For specimen No. 2 a similar occurrence was observed—specimens preoxidized at 1200°C (Curves 2 and 2') were oxidized at 700°C considerably more slowly than the initial specimen. The slight advantage of the pre-oxidized specimens was retained through the entire 10-hour period of testing.

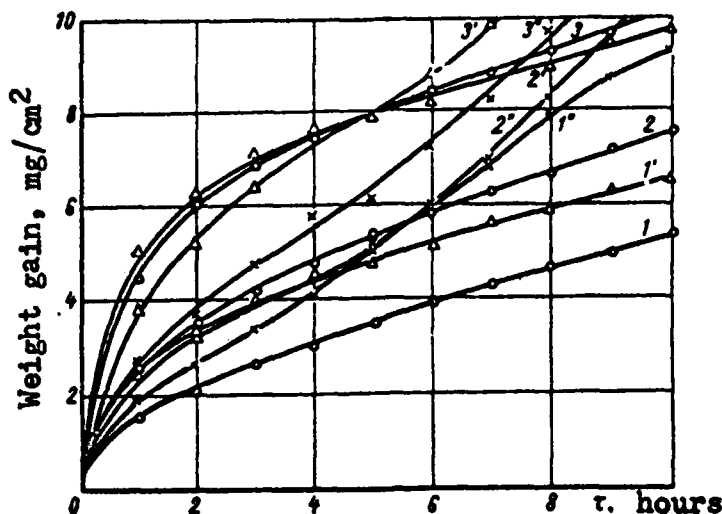


Figure 5. Oxidation Kinetics of Alloy Zr-15% Nb-10% Mo in Air at 700°C: 1,2,3--Specimens Pre-Oxidized in Air; 1',2',3'--Specimens Pre-Oxidized in Oxygen; 1'', 2'',3''--Specimens Without Preliminary Oxidation.

The kinetic curves for specimens of the alloy Zr-15% Nb-10% Mo in the initial state (Curves 1'',2'',3'', see Figure 5) followed the parabolic law for the first three to four hours and the subsequent part of the curves corresponded to oxidation accelerating in time and not subordinate to the parabolic law. The specimens pre-oxidized at 1200°C (besides Specimen 3'') were oxidized by the parabolic law throughout the entire test time which lasted 10 hours (Curves 1, 1', 2, 2', 3). The influence of the preliminary oxidation at 1200°C on the oxidation rate of the alloy Zr-15% Nb-10% Mo is somewhat less than for alloy Zr-25% Nb.

X-ray investigation of the black oxide film obtained in oxygen at 1200°C (a weight gain of 0.5 milligrams/sq cm) which was separated by etching the specimen in a 50%-hydrofluoric acid showed that this film does not contain a noticeable amount of the compound  $6\text{ZrO}_2 \times \text{Nb}_2\text{O}_5$ . That is, the slight increase in heat resistance that was observed after preliminary oxidation is not due to the formation of this complex compound. The formation of the compound  $6\text{ZrO}_2 \times \text{Nb}_2\text{O}_5$  occurs only in the later stages of oxidation at high temperatures after the beginning of the formation of the white oxide.

## Conclusions

1. It was shown that upon oxidation in air of alloys Zr-25% Nb and Zr-15% Nb-10% Mo a compound  $6ZrO_2 \cdot Nb_2O_5$  appears on the surface along with  $ZrO_2$ . The amount of the  $6ZrO_2 \cdot Nb_2O_5$  during strong oxidation at 1200 °C of alloy Zr-25% Nb reaches almost 100% and close to 100% for the second alloy.

2. Preliminary oxidation of these alloys at 1200° C at lowered pressure in oxygen and in air before the formation of the black oxide film somewhat increases their resistance to oxidation at 700° C which is not due, however, to the formation of  $6ZrO_2 \cdot Nb_2O_5$ .

3. The elevated resistance to oxidation of alloy Zr-25% Nb at temperatures below 600° C, evidently, cannot be explained only by the formation of the compound  $6ZrO_2 \cdot Nb_2O_5$  since even after oxidation at 600° C the content of this compound in the oxide film is low.

## BIBLIOGRAPHY

1. O. S. Ivanov and V. K. Grigorovich, "Structure and Properties of Zirconium Alloys", Trudy Vtoroy mezhdunarodnoy konferentsii po mirnomu ispol'zovaniyu atomnoy energii (Papers of the Second International Conference on the Peaceful Use of Atomic Energy), Geneva, 1958, Vol 3 -- Nuclear Fuel and Reactor Metals, Moscow, Atomizdat, 1959, page 439.
2. Sbornik:metallurgiya zirkoniya (Collection: Metallurgy of Zirconium), Moscow, Publishing House of Foreign Literature, 1959.
3. R. S. Ambartsumyan and others, "Mechanical Properties and Corrosion Resistance of Zirconium and Its Alloys in Water, Steam, and Gases at Elevated Temperatures", same source as reference 1.
4. Yu. F. Bychkov, A. N. Rozanov, and D. M. Skorov, Atomnaya energiya (Atomic Energy), Vol II, Nr 2, 1957, page 146.
5. W. D. Klopp, C. T. Sims, R. J. Jaffee, Report Nr 712 (USA) presented at the Second International Conference on the Peaceful Use of Atomic Energy, Geneva, 1958.
6. Atomic Energy Research Establishment, 1960, NR 3257, page 28.
7. Yu. F. Bychkov, V. V. Vasov, and A. N. Rozanov, V sb.: Metallurgiya i metallovedeniye chistykh metallov (In the Collection: Metallurgy and Metal Science of Pure Metals), Nr III, Moscow, Gosatomizdat, 1961, page 82.

8. R. Rot and L. Kofanur, "Equilibrium of Phases in Niobium pentoxide - Titanium Dioxide and Niobium Pentoxide - Zirconium Dioxide Systems", V sb.: Niobiy i tantal (In the Collection: Niobium and Tantalum), Ed. O. P. Kolchin, Moscow, Publishing House of Foreign Literature, 1960, page 422.

6306

CSO: 1879-D

## OBTAINING MOLYBDENUM SINGLE CRYSTALS AND THEIR PROPERTIES

V. S. Yemel'yanov, A. I. Yevstyukhin,  
G. A. Leont'yev, and A. N. Semenikhin

Modern technology requires high melting metals and alloys based on them. It is necessary that there be broad research conducted on these metals and alloys. The most interesting results can be obtained in the study of pure single crystals.

For most metals with a comparatively low melting temperature the methods of obtaining single crystals have been well developed and described in literature [1]. But the obtaining of pure monocrystals of refractory metals such as molybdenum, tungsten, niobium, and tantalum has certain experimental difficulties. In this connection we attempted to grow single crystals of molybdenum from the gaseous phase using the method of thermal dissociation.

The possibility of obtaining single crystals from the gaseous phase was mentioned by Van Arkel [2]. To grow the monocrystal it is necessary to have a monocrystal base. Then the growing deposit of metal will repeat the structure of the base. Single crystal filaments were obtained by recrystallization of polycrystal wires from molybdenum mounted in an apparatus for deposition. The methodology and the equipment used in the experiment were described in the work of V. S. Yemel'yanov and others [3]. After heating at 1550-1650°C for 2-4 hours on a molybdenum wire 0.1 mm in diameter it was possible to obtain single crystal segments from 10-90 mm long.

The features of obtaining molybdenum deposits from the gaseous phase by thermal dissociation of  $\text{MoCl}_5$  required that deposition begin at 1500-1600°C. After a certain time the temperature was reduced to 1280-1300°C. At temperatures below 1280°C the deposition proceeded more slowly but the deposit had a mirror finish with smooth ribs. Upon an increase in the temperature of the filament the rate of deposition increased and the

definition of the crystals became more clearly expressed. In this way filaments up to 3 mm thick consisting of monocrystal segments up to 90 mm long were obtained. The external appearance of such segments is shown in Figure 1. The content of gas additions in the single crystal and also in the base material are given in Table 1.

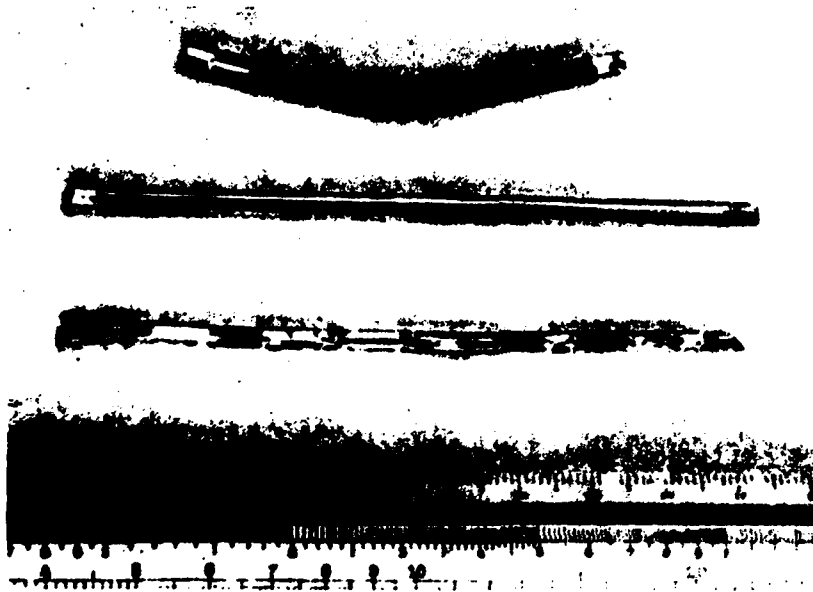


Figure 1. External Appearance of Molybdenum Single Crystals.

Table 1

Gas Content in Metallic Molybdenum (in %)

Material	N <sub>2</sub>	H <sub>2</sub>	O <sub>2</sub>
Initial chip . . . . .	1.7 · 10 <sup>-3</sup>	1.4 · 10 <sup>-3</sup>	4 · 10 <sup>-3</sup>
Chip after growing a single crystal. . .	4 · 10 <sup>-3</sup>	3 · 10 <sup>-3</sup>	5 · 10 <sup>-3</sup>
Single crystal . . . . .	8 · 10 <sup>-4</sup>	6 · 10 <sup>-4</sup>	1.5 · 10 <sup>-3</sup>

The single crystals that were obtained had high plasticity at room temperature. They bent easily at a large angle and were cold rolled while the polycrystalline deposit obtained from the gas phase broke easily during bending due to the poor bonds between the individual crystals. The appearance of the bent single crystal is shown in Figure 2. The molybdenum single crystals have considerably less hardness than the normal metal (Table 2).



Figure 2. Molybdenum Single Crystals Bent at Room Temperature

Table 2

Hardness of Various Molybdenum Specimens

Material	Hardness after <sub>2</sub> Brinell, kg/mm <sup>2</sup>
Single crystal A	82-86
Single crystal B	76-85
Industrial sheet, 0.95 mm thick deformed	237-247
annealed at 1000° C	209

The microhardness of the single crystals was in the range 180-200 kg/mm<sup>2</sup> (load of 200 grams) and for normal industrial metal in the annealed state it is 230-260 kg/mm<sup>2</sup>.

Other properties that were studied were the modulus of elasticity and the internal friction. For these purposes whole single crystals 90 mm long were cut from rods. In order to be convinced whether the specimen consists of a single monocrystal, at several points on one face Lauegrams were taken which turned out to be identical. One of these photographs is shown in Figure 3.



Figure 3. A Typical Lauegram Taken From the Reflection of a Face of the Single Crystal

The modulus of elasticity and the internal friction were measured on equipment described in the work of A. I. Dashkovskiy, A. N. Semenikhin, and P. L. Gruzin (see page 41 of this collection). The modulus of elasticity was calculated from the resonance frequency of bend oscillations of a freely supported cylindrical specimen. The internal friction  $Q^{-1}$  was determined from the dampening of the bend oscillations. For comparison the same measurements were made in polycrystalline specimens from normal molybdenum serving as the raw material for obtaining the single crystals. The measurement showed that the modulus of elasticity of the single crystals is somewhat greater than in specimens from the normal metal (Figure 4, Table 3).

Table 3

The Elasticity Modulus at Room Temperature for Various Types of Molybdenum

Material	E, kg/mm <sup>2</sup>
Single crystal A	33,300
Single crystal B	33,900
Industrial metal	31,600
" "	31,800 [4]
" "	32,000 [5]

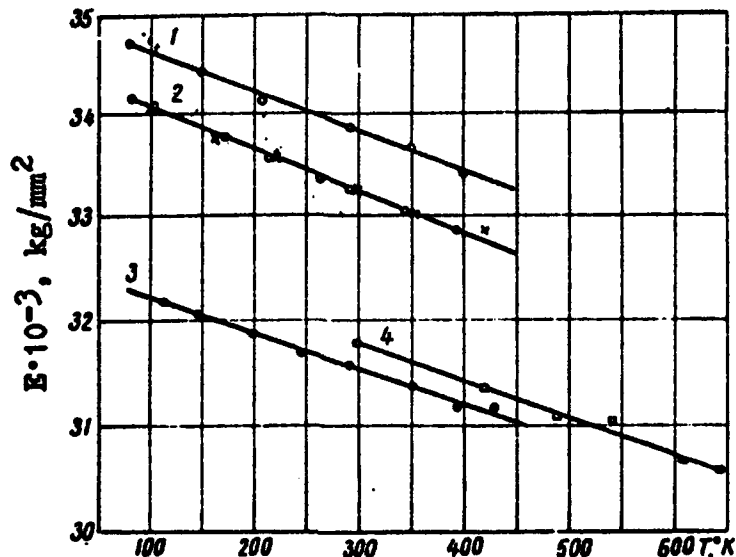


Figure 4. Change in the Modulus of Elasticity  $E$  for Molybdenum Single Crystals in Relation to Temperature: 1--single crystal B; 2--single crystal A (O--in the initial state, X--after annealing at  $600^{\circ}\text{C}$  for 2 hours); 3--industrial molybdenum; 4--industrial molybdenum from the work of Freerman and others [4].

The internal friction in molybdenum single crystals monotonously increases in the measured range of temperatures from  $1.6 \times 10^{-5}$  at  $-190^{\circ}\text{C}$  to  $3.8 \times 10^{-5}$  at plus  $200^{\circ}\text{C}$ .

In quenched and then wrought single crystals there was a regression of the values of the internal friction  $Q^{-1}$ . Quenching was done in the equipment to balance the crystals with a temperature of about  $1300^{\circ}\text{C}$ . The quenched single crystals had a low internal friction. After slight bending strain (residual bending of about 1 mm) the internal friction increased sharply. At heating to  $90^{\circ}\text{C}$   $Q^{-1}$  in the deformed single crystal began to drop sharply (Figure 5). As a result of heating to  $130^{\circ}\text{C}$  the internal friction was reduced by three times; additional annealing at  $600^{\circ}\text{C}$  for 2 hours led to only a slight additional reduction in the value  $Q^{-1}$ .

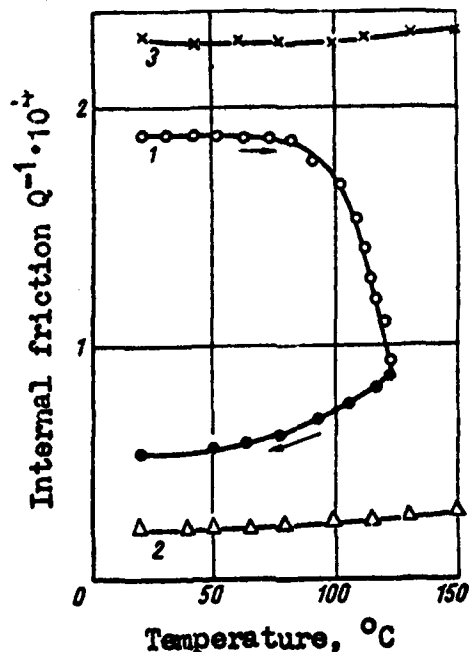


Figure 5. Change in the Internal Friction of a Molybdenum Single Crystal in Relation to Temperature: 1--quenched and then bent monocrystal; 2--annealed at 600°C for 2 hours; 3--annealed at 600°C for 2 hours and then bent.

Crystals annealed at 600°C were subjected to the same deformation as the quenched crystals but the regression in the  $Q^{-1}$  in the temperature range 100-200°C did not occur in them.

According to the theory of Granato and Lucke [6], the internal friction can be attributed to the dislocation motion under the applied stresses. In plastic bending the number of dislocations increases which leads to an increase in the value  $Q^{-1}$ . If the crystal contains an excessive number of point defects which are fixed by quenching, then the latter can migrate toward the dislocations and amplify them reducing thereby the level of internal friction.

### Conclusions

1. A methodology was developed for growing molybdenum single crystals from the gaseous phase using the method of thermal dissociation.

2. Preliminary investigations of hardness, modulus of elasticity, and internal friction were conducted in the single crystals that were obtained.

#### BIBLIOGRAPHY

1. V. D. Kuznetsov, Kristally i kristallizatsiya (Crystals and Crystallization), Moscow, Gostekhizdat, 1954.
2. Van Arkel, Reine Metalle (Pure Metals), 1939.
3. V. S. Yemel'yanov, G. A. Leont'yev, and A. I. Yevstyukhin, Sbornik metallurgiya i metallovedeniye chistykh metallov (In the Collection Metallurgy and Metal Science of Pure Metals), Nr III, Moscow, Gosatomizdat, 1961, page 137.
4. R. E. Freerman and J. Z. Briggs, Propulsion, Vol 27, Nr 2, 1957, pages 138-147.
5. R. M. Parke, Metals Progress, Vol 59, 1951, page 81.
6. A. Cranato and K. Lucke, Journal of Applied Physics, Nr 27, 1956, page 789.

6306

CSO: 1879-D

**INVESTIGATION OF THE DISTRIBUTION OF ADDITIONS  
IN NIOBIUM AFTER ZONE REFINING**

A. I. Yevstyukhin  
V. V. Nikishanov  
I. V. Milov

**Introduction**

In published works [1-3] the growing interest in niobium and its importance for the development of certain branches of new technology are pointed out. It is also noted that the methods of refining niobium of the additions which accompany it determine to a large degree the level of its production and use.

At present various methods of refining niobium have been developed. Zone refining of niobium and its melting using the electron-beam method have the best prospects [4-6]. Remelting niobium in modern equipment with electron-beam heating makes it possible to obtain niobium in the form of ingots of different size [7-9]. The remelted ingots of niobium can be pressure worked and worked by other methods. For example, they can be rolled into a foil 0.013 mm thick without intermediate annealing [10].

Research has shown that the remelting of niobium by the electron-beam method causes considerable vaporation of certain additions including Fe, Cr, Al, Ni, V, W, C, and B [11].

However, the equipment for electron-beam melting in production is still quite complex. In this sense, the equipment for arc and induction melting are most reliable in production. The melting and some recrystallization of niobium in this case occurs in crucibles and without crucibles. Electric arc melting of niobium, from our point of view, is most suitable and productive in production.

The method of arc zone recrystallization in a copper cooled crucible in a vacuum (or in an atmosphere of clean inert gas) makes it possible with the use of comparatively simple equipment to obtain niobium in the form of ingots with large single crystals of very high purity [12]. The use of induction heating in zone recrystallization in the variation without the crucible also makes it possible to grow single crystals of niobium of very high purity [8, 12], but this method has low productivity and is less economical.

### The Theoretical Possibility of Refining Niobium by Zone Recrystallization

Study of binary phase diagrams of alloys of niobium with other elements makes it possible qualitatively, and in some instances when the factor of distribution of additions in the niobium is known, quantitatively to describe the degree of refining of niobium of additions by zone recrystallization.

Three types of interaction of additions with this metal can be selected from the set of phase diagrams of alloys of niobium with other elements.

The first type of additions include the elements forming a series of solid solutions with niobium. They include Mo, Ta, Ti, W, V, U, and Zr. The second type of addition includes the elements that form limited zones of solid solutions and they are: C, Cr, Ce, Fe, Si, B, Be, Al, N, Sn, Re, Cu, Mg, and La. The third type of addition includes the elements that practically do not dissolve in the solid niobium. Such elements are, for example, hydrogen and thorium. Since microquantities of these additions have a large effect on the properties of niobium, refining it of additions has great practical importance.

The degree of refining and the direction of movement of additions in zone recrystallization basically are determined by the value of the factor distribution of an addition in the solvent.

When  $K$  is greater than 1 the addition is moved in the direction opposite to the motion of the zone; if  $K$  is less than 1 the addition moves in the direction of the zone movement. The greater the difference between the distribution factor and 1 the higher the degree of refining will be.

Table 1 gives the characteristics of binary systems of niobium. As it follows from the table, the degree of refining and the nature of transfer of all the additions can be divided into three groups.

The first group includes additions in which  $K$  is greater than 1. A typical metal in this group is W. The second group of additions is formed by Pb, Sn, Ti, La, H, Th, Cu, Mo, Zr, U, Cr, Ce, V, Fe, Si, O, N, Al, B, and C. For these elements  $K$  is less than 1. Therefore, the

effectiveness of niobium refining is increased upon a reduction in K and is greatest for thorium and hydrogen. Additions of this group during refining should be concentrated in the last zone of the ingot. The third group includes such additions as Ta, Re, and Mg. These elements have a factor of distribution K that is close to 1. This makes their redistribution during zone recrystallization difficult. In this case magnesium is separated from the niobium by vaporization while Ta and Re remain in the ingot.

Table 1

Characteristics of Binary Systems of Niobium Alloys

Addition	Eutectic temperature, °C	Maximum solubility, wt. %	K	Reference
W	—	Cont. ser. of solid sol.*	3.9	[9]
Ta	—	Same	1.2	[13]
Re	2350	64.0	~1	[14]
Mg	2380	~1.0	<1	[15]
Mo	—	Cont. ser. of solid sol.	0.8	[16]
U	—	Same	0.75	[17]
Pb	—	—	0.71—0.8	according to authors' data
V	—	Cont. ser. of solid sol.	0.72	[18]
Zr	—	Same	0.4—0.6	[19]
Al	2120±10	6.0	0.32	[20]
B	1600	0.49	0.3	[21]
Ti	—	Cont. ser. of solid sol.	0.3	[22]
Si	1850	1.56	0.2 <sup>a</sup>	[23]
Fe	~1660	2.44	0.17—0.2	[24]
Cr	1660	12.25	0.2	[25]
Cu	1580	16.0	0.17—0.2	[26]
Sn	2000±25	13.0	0.143	[27]
O	1915	0.72	0.13	[28]
N	—	0.07	<1	[29]
C	2335	0.03	<1	[30]
Co	2370±20	2.0	<1	[31]
La	2400	0.1—0.2	<1	[32]
Th	1435	0	<1	[33]
H	—	0	<1	[34]

\* Cont. ser. of solid sol. -- Continuous series of solid solutions.

On the basis of these data it can be expected that during zone recrystallization niobium should be cleaned of additions and almost all of them except Ta and W, should be concentrated in the last part of the ingot. When there are large numbers of zone passes and corresponding rates of zone movement the middle part of the ingot should be freest of additions. The factor of vaporization of additions should also play a very important role in the refining process [7].

#### A Discussion of the Results of the Investigation

In this section we describe the experiments and the results of refining niobium of technical purity of carbon, iron, lead, and tungsten in a specialized laboratory arc furnace using the method of zone recrystallization. The methodology and the equipment in which the experiments were conducted were described earlier by the authors [3].

The experiments were conducted in an atmosphere of clean helium at low pressures. An axial-symmetric constant magnetic field concentric to the arc tongue was used to stabilize the arc tongue during melting. Careful stabilization of the arc is necessary to create more balanced conditions of metal crystallization. An unstable thermal feed in the molten zone causes rapid solidification of the layers that are enriched with additions near the crystallization front (concentration peak) arising in the liquid zone due to insufficient mixing of the melt which reduces the effectiveness of the process of addition redistribution. The melting regime for the experiments described above was as follows: current--500 amp, voltage--24.5 volts, length of molten zone--25 mm.

Before the beginning of the zone recrystallization the ingots were about 230 mm long (about 10 zones) and weighed 150 grams. It should be noted that in the melting process all of the ingots were shortened to 200 mm (8 zones) as a result of the transfer of metal to meet the movement of the zone (its effect can be eliminated using proper angle of the crucible). Variations in the current fed into the zone did not exceed 1-3%. The number of zone passes for all the ingots besides the ingots studied for the transfer of lead was ten. The rate of movement of the molten zone in the experiment was 0.75 mm per minute. For the ingots in which the transfer of lead was studied 2 rates were used: 30 and 0.75 mm per minute. The length of the molten zone was the same as in the other experiments--25 mm.

The experiments were conducted with niobium of industrial purity. The initial content of additions in niobium is given in Table 2.

Table 2

## Additions in Industrial Purity Niobium

Addition	Content, wt. %	Addition	Content, wt. %
O	0,008	Cr	0,04
H	0,007	Ti	0,15
C	0,05	Si	0,08
Fe	0,08	Pb	0,03
N	0,012		

For study of the redistribution of carbon, iron, and tungsten their radioactive isotopes were used. There was parallel chemical analysis of control ingots (without isotopes) recrystallized under the same conditions.

In one ingot of industrial purity with an initial carbon content of 0.05 wt.%, 0.005 wt.% of the isotope  $C^{14}$  was introduced; in another ingot with an initial iron content of 0.08 wt.%, 0.01 wt.% of the  $Nb^{59}$  isotope was introduced; in a third ingot with an initial tungsten content of 0.03 wt.%, 0.01 wt.% of the  $W^{182}$  isotope was introduced. The amount of isotope was selected with consideration of its specific activity in such a way that the basic chemical composition of the ingot was not changed.

After introduction of the radioactive isotopes all the ingots (including the control ingots) were subjected to zone recrystallization with a speed of 0.75 mm/min. with four passes (the number of passes was established experimentally). The uniformity of distribution of the isotopes was checked by measuring the activity of the individual sections of the ingots.

Ingot with a balanced composition were subjected to zone recrystallization after which the radioactivity of the various sections of the ingot from the side of the arc and from the side of the crucible was measured. The measurement was done on a gage of the type T-25-BSL. The control in active ingots and the ingots in which the lead transfer was studied were analyzed in a chemical laboratory.

The distribution factors of carbon, iron, and tungsten, determined from the phase diagrams of the alloys Nb-C, Nb-Fe, and Nb-W (see Table 1) are respectively:  $K_C$  is greater than 1;  $K_{Fe} = 0.17-0.2$ ;  $K_W = 3.9$ . Consequently, in the zone recrystallization process the tungsten must be concentrated in the first part of the ingot; the iron and carbon must be

concentrated in the last part. The experiments confirmed these assumptions.

### Transfer of Carbon

Study of the distribution of the radioactive isotope  $C^{14}$  after zone recrystallization showed that the carbon is concentrated in the last part of the ingot. This is evidence that the distribution factor of the carbon in the niobium is less than 1. Along the transverse cross section of the ingot the carbon is distributed uniformly; measurements of activity along the upper and lower surfaces of the ingot gave coinciding results. Figure 1 shows a curve of the distribution of the radioactive isotope  $C^{14}$  along the length of the ingot. The curve shows that the ratio of the concentration of carbon in the end and the beginning of the ingot is 8:1. In the experiment a considerable vaporization of carbon was revealed. Evidently this is in the form of the products CO or  $CO_2$  since the walls of the crucible and the chamber showed no activity after melting and the over-all level of activity of the ingot as a whole was lowered.

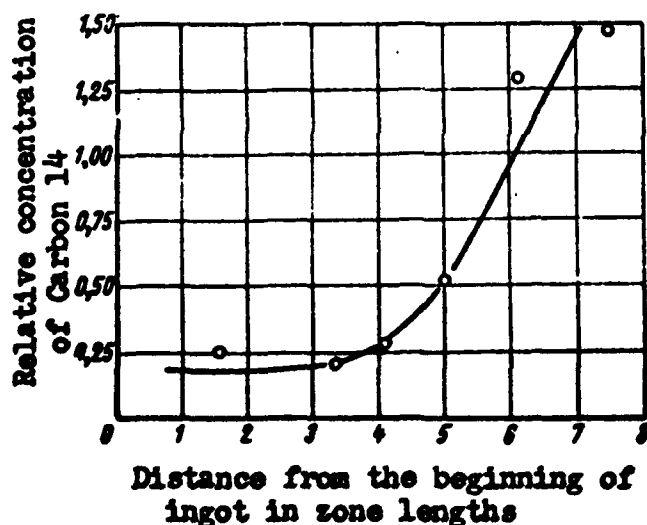


Figure 1. Change in Radioactivity Along the Length of an Ingot of Niobium With the Radioactive Isotope Carbon 14 After 10-fold Zone Recrystallization

The data of chemical analysis (Table 3 and Figure 2) confirmed that the niobium is refined of carbon under the action of zone recrystallization and also indicate the vaporization of carbon from the ingot (the carbon content is nowhere greater than the initial carbon content).

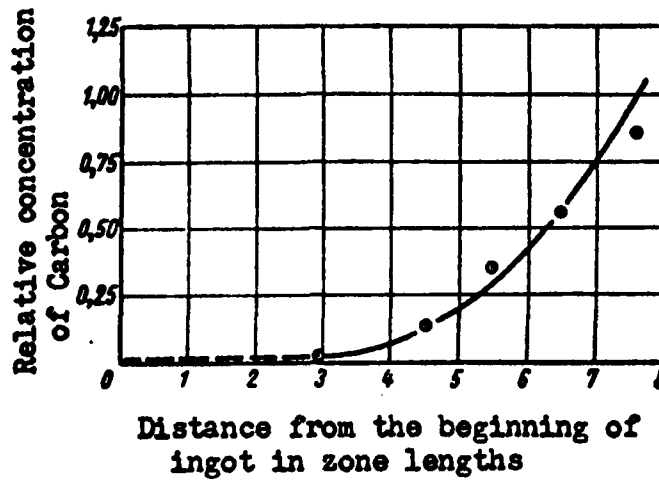


Figure 2. Change in Carbon Content Along the Length of an Ingot of Niobium After 10-Fold Zone Recrystallization (From the Data of Chemical Analysis).

Table 3

Carbon Content in Certain Sections of the Ingot After Zone Recrystallization

Number of section	Distance from beginning of ingot, mm	Carbon content, wt. %
1	12	Not revealed
2	37	" "
3	62	" "
4	87	" "
5	112	>0.01
6	137	0.010
7	163	0.025
8	185	0.041

The data of radiometry and chemical analysis are evidence that the section equal to 3-4 lengths of the zone, that is, about half of the ingot, is refined of carbon to the greatest extent.

## Transfer of Iron

Figure 3 gives a graph of the distribution of the radioactive isotope  $Fe^{59}$  in an ingot of niobium of industrial purity after 10-fold zone recrystallization. The data of chemical analysis give the same picture of transfer of iron in the direction of zone movement (Table 14, Figure 4).

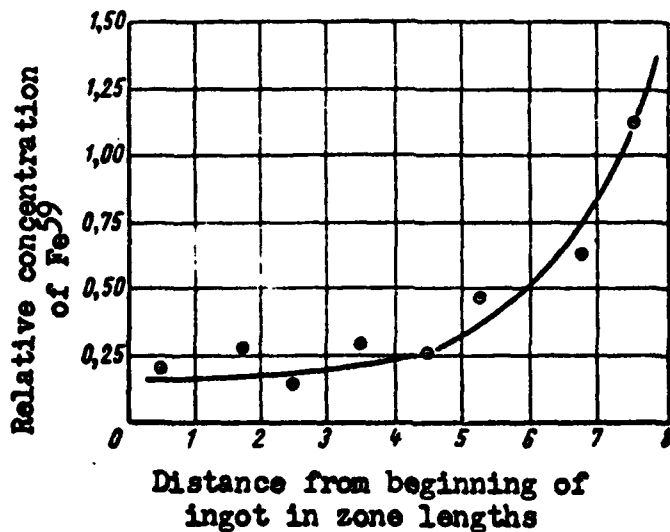


Figure 3. Change in Radioactivity Along the Length of an Ingot of Niobium With The Radioactive Isotope  $Fe^{59}$  After 10-Fold Recrystallization.

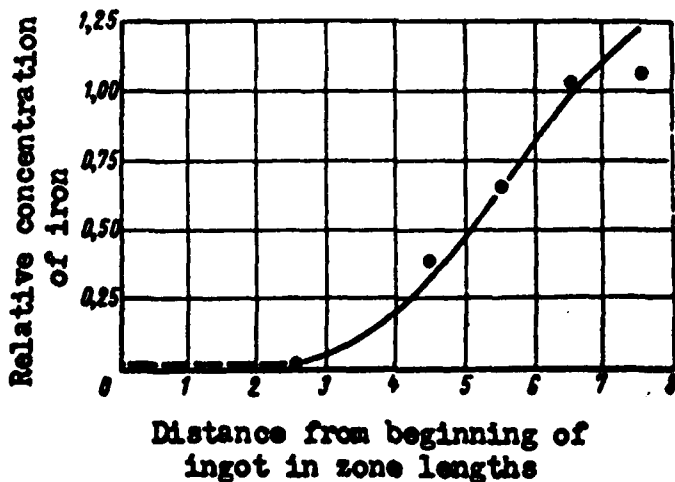


Figure 4. Change in Iron Content Along the Length of an Ingot of Niobium After 10-Fold Recrystallization (From Data of Chemical Analysis).

Table 4

Iron Content in Certain Sections of the Ingot  
After Zone Recrystallization

Section number	Distance from beginning of ingot, mm	Iron content, %
1	10	Not revealed
2	35	, ,
3	65	, ,
4	90	0.031
5	110	0.040
6	135	0.055
7	161	0.083
8	186	0.095

Along the vertical cross section of the ingot the iron (just as the carbon) is distributed uniformly. The results of radiometry and chemical analysis make it possible to say that iron during zone arc recrystallization is vaporized in a significant amount since only the last two sections have a slightly different iron content from the initial iron content and the first three sections can be considered to be practically free from iron. According to the data of radiometric measurements the degree of refining of these section is about 5:1.

Thus, using the described regime of recrystallization the niobium is noticeably refined of iron.

#### Transfer of Lead

Published literature has no data on the phase diagram of the Nb-Pb system and before this experiment we did not know the factor of distribution of lead in niobium.

Figure 5 shows three curves of the distribution of lead in niobium for two ingots after 64 and 32 passes with a speed of 30 mm/min. and for one ingot after 10 passes with a speed of 0.75 mm/min. Table 5 gives data of the chemical analysis of specimens in different sections of the ingot. The initial lead content in industrial niobium was 0.03 wt.%.

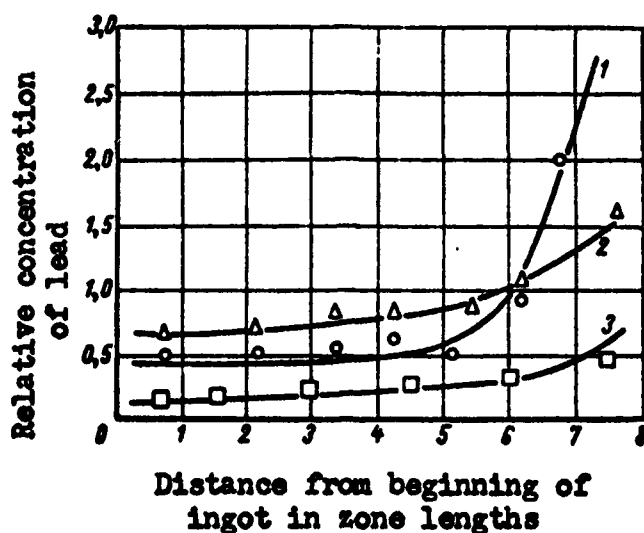


Figure 5. Change in the Lead Content Along the Length of an Ingot After Zone Recrystallization With Different Speeds and Different Number of Passes  $n$ : 1—30 mm/min,  $n = 64$ ; 2—30 mm/min,  $n = 32$ ; 3—0.75 mm/min,  $n = 10$ .

Table 5

Lead Content (in %) in Various Sections of the Ingot After Zone Recrystallization

Specimen number	No. of zone passes	Beginning	Middle	End
1	64	0.015	0.015	0.075
2	32	0.021	0.024	0.049
3	10	0.006	0.006	0.015

It follows from the data in Figure 5 and Table 5 that lead is concentrated in the last section of the ingot. As the number of passes of the zone along the ingot is increased the depth of refining of niobium of lead is increased. We calculated the effective factor of distribution of lead in niobium; it was 0.80 for a specimen after 64 passes of the zone and 0.71 for a specimen after 32 passes of the zone.

A third ingot (Curve 3, see Figure 5) was recrystallized with a speed of movement of the zone of 0.75 mm/min. Ten passes were made and it was established that in this regime of melting the vaporization of the

lead predominates over the refining effect due to zone recrystallization. The vaporization rate upon a zone movement with a speed of 30 mm/min is  $1.8 \times 10^{-6}$  grams/min sq cm and with a speed of 0.75 mm/min it is  $7.5 \times 10^{-6}$  grams/min sq cm. The over-all degree of refining due to recrystallization and vaporization is considerably higher when the zone moves with a speed of 0.75 mm/min. But the effect of refining due to only zone recrystallization at a speed of 0.75 mm/min is less than when the speed of movement is 30 mm/min. This can be explained by the fact that at low speeds of zone movement its rate is comparable with the rate of diffusion of lead from the liquid phase into the solid phase.

On the basis of these results certain conclusions can be reached.

1. The solubility of lead in niobium can be estimated in several hundredths of a per cent; the lead addition in technical niobium, probably, is in the solid solution (metallographic analysis nowhere revealed the presence of a second phase). The diagram of Nb-Pb in its niobium part, probably, should have a eutectic.

2. The lead content in technical niobium can be reduced considerably by zone recrystallization during arc melting. The vaporization of lead plays an important role; it can predominate over the effect of zone recrystallization.

### Transfer of Tungsten

The results of experiments on the transfer of tungsten confirmed the assumption that tungsten is concentrated in the first section of the ingot and its factor of distribution is considerably greater than 1.

Table 6 gives the results of measuring the activity of a niobium ingot with the radioactivity isotope  $W^{182}$  and the results of measuring the radioactivity of the ingot from the side of the crucible and along the upper side of the ingot.

Figure 6 gives the curve of distribution of the radioactive isotope  $W^{182}$  along the length of the ingot; in this case the activity was measured from the side of the crucible.

Study of the distribution of intensity of radiation of the ingot shows that the ratio of intensities of the first and last sections in the upper layers is 4.65 to 1 while in the lower layers (from the side of the crucible) the equivalent ratio is 3.1 to 1. The distribution of the radioactive isotope  $W^{182}$  across the cross section of the niobium ingot (see Table 6) shows the continuous increase in the tungsten content from the upper to the lower layers of the ingot.

Table 6

Change in the Activity of a Niobium Ingot With  
Radioactive Isotope  $W^{182}$  Along the Length of the Ingot (1/64)

Section number	Distance from beginning of ingot, mm	Radiation intensity, pulses/minute x $cm^2$	
		Top of ingot	Bottom of ingot
1	7	812	800
2	18	575	710
3	43	408	575
4	65	340	480
5	88	278	410
6	116	232	370
7	138	210	310
8	153	190	290
9	175	175	245

Note: Radiation intensity of the ingot after zone balancing was 625 pulses/minute x  $cm^2$ .

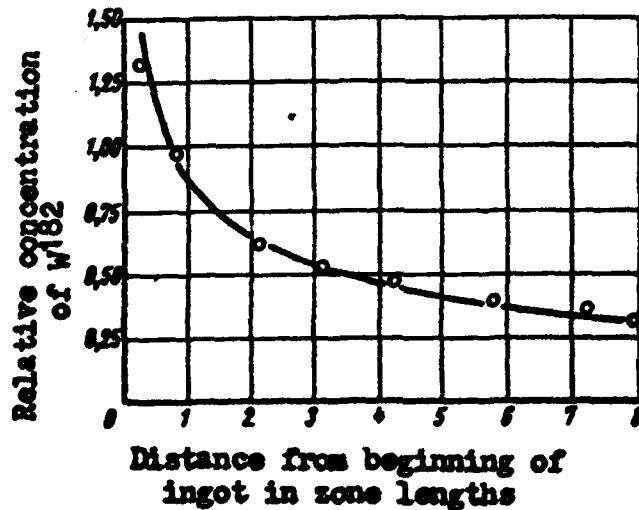


Figure 6. Change in Radioactivity Along the Length of an Ingot of Niobium With Radioactive Isotope  $W^{182}$  After 10-Fold Recrystallization

The redistribution of tungsten across the cross section of the ingot can be explained by the following factors.

1. It can be explained by the presence of a distribution coefficient greater than 1. Such a distribution factor leads to relocation of tungsten during zone recrystallization counter to the movement of the zone and also counter to the direction of grain growth. In crucible melting the grains begin to grow from the bottom and the walls of the crucible and then they bend and grow along the axis of the ingot.

2. Insufficient mixing of the melt in the liquid zone as a result of which the vaporization effect of the tungsten can cause impoverishment of the upper layers of the niobium ingot. The vaporization of tungsten is confirmed by the fact that the walls of the melting chamber which were cleaned at the beginning of the melt show considerable activity after zone recrystallization.

3. It is possible that there occurs also an accumulation of tungsten in the lower layers of the ingot due to the difference in the specific weights of tungsten and niobium.

4. Considering the saucer-shape of the liquid zone and the incomplete mixing of the melt in it it can be assumed that the capacity of the zone with respect to additions differs along the height and drops from top to bottom. This can cause nonuniform distribution of additions along the height of the ingot and a more significant effect of the refining in the upper layers of the ingot than in the lower layers.

The refining effect was inspected by chemical analysis and metallographic methods. Table 7 shows the tungsten content in various sections of the control ingot (without the radioactive isotope) after 10 passes of the zone following the melting regime that has been described.

The initial tungsten content in the niobium was  $3 \times 10^{-2}$  wt. %.

Table 7

Change in Tungsten Content in the Niobium Ingot After Zone Recrystallization

Section number	Distance from beginning of ingot, mm	Tungsten content, $\times 10^{-2}$ wt. %
1	10	4.2
2	20	4.2
3	53	3.6
4	90	1.6
5	110	0.44
6	140	—
7	170	—

Figure 7 shows the change in the tungsten content along the length of the ingot from the data of the analysis. The effective factor of distribution of tungsten in niobium, calculated from the results of experiments on refining niobium of tungsten with inspection using radioactive isotopes, is 6, and 25, and using inspection by chemical analysis it is 4.9. The calculation of the factors of distribution of lead and tungsten was done using the method described in Paper [33].

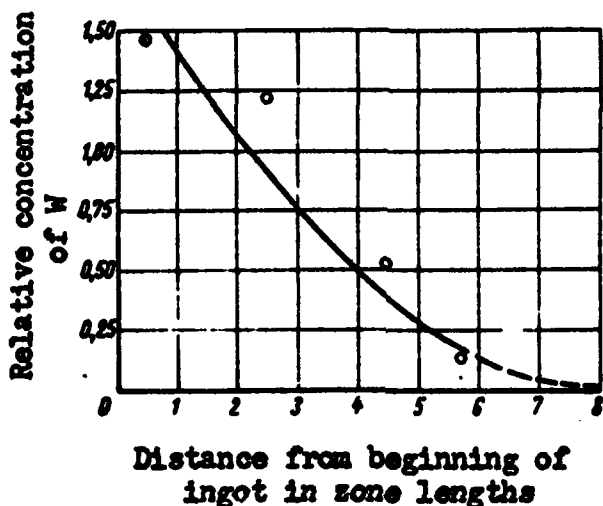


Figure 7. Change in Tungsten Content Along the Length of a Niobium Ingot After 10-Fold Zone Recrystallization (From Data of Chemical Analysis)

The difference between the distribution factors that were found and those that were calculated from the phase diagram of Nb-W [9] can be explained by the influence of the vaporization of tungsten on the effect of zone recrystallization.

Metallographic analysis of the specimen showed that when the rate of movement of the zone is 30 mm/min a clearly expressed columnar structure is observed. The grains grow from the bottom and the walls of the crucible toward the axis of the ingot and bend in the direction of the movement of the zone.

When the rate of movement of the zone is 0.75 mm/min very large grains that are oriented in the same way with a length of 15-20 mm are formed; they occupy the entire cross section of the pouring lip of the crucible. X-ray analysis showed that these grains are perfect single crystals (Figure 8). The disorientation of blocks in them is slight.

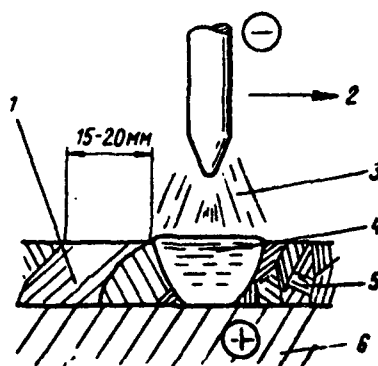


Figure 8. A Drawing of Zone Electric Arc Recrystallization: 1--Single Crystal Grains; 2--Direction of Movement of the Zone; 3--Arc; 4--Zone; 5--Ingot; 6--Copper Crucible.

Near the first and the last parts of the ingot the grains are somewhat finer. The boundaries between them are difficult to perceive. When the ingot is bent it breaks not along the grain boundaries but across the grain; the fracture occurs precisely along the junction plane.

Investigation of the hardness of these single crystals showed that some of them, located basically in the middle of the ingot, have a Brinell hardness of 90-100 kg/sq mm. The initial hardness of the ingot after balancing zone recrystallization was 180 kg/sq mm.

### Conclusions

1. The paper contains a brief examination of the theoretical assumptions of the possibility and effectiveness of refining niobium of additions by the method of zone recrystallization.
2. The additions in the niobium are classified according to the degree of effectiveness of their refining using zone recrystallization.
3. The experiments that were conducted on zone recrystallization of niobium by the arc method in a copper crucible showed that effective refinement of additions (carbon, iron, lead, and tungsten) with different distribution factors is achieved.
4. It was established that in arc zone recrystallization of niobium there is also refinement of additions by means of vaporization (particularly the volatile additions and also metals that form volatile compounds).

## BIBLIOGRAPHY

1. A. I. Yevstyukhin, V. V. Nikishanov, and I. V. Milov, "Zone Melting of Niobium Using the Arc Method", Metallurgiya i metallovedeniye chistykh metallov (Metallurgy and Metal Science of Pure Metals), Gosatomizdat, 1961, page 152.
2. G. G. Ryabova, P. L. Gruzin, and A. I. Yevstyukhin, "Study of the Distribution of Additions of Carbon, Iron, and Chromium in Niobium by Autoradiography", Metallurgiya i metallovedeniye chistykh metallov (Metallurgy and Metal Science of Pure Metals), Gosatomizdat, 1961, page 163.
3. A. I. Yevstyukhin, V. V. Nikishanov, and I. V. Milov, "Zone Refining of Niobium by the Electric Arc Method", Sbornik nauchnykh dokladov po teorii zharoprochnosti (Collection of Scientific Reports on the Theory of Heat Resistance), Publishing House of the Academy of Sciences, U.S.S.R., 1961, page 242.
4. Chemical Week, Vol 85, Nr 5, 1959, page 51.
5. Chemical Engineering Progress, Vol 54, Nr 5, 1958, pages 118, 120, and 140.
6. S. H. Dayton, Mining World, Vol 20, Nr 8, 1958, pages 40-44.
7. H. R. Smith, C. Hunt, and C. J. Hanks, Journal of Metals, Vol 11, Nr 2, 1959, pages 112-117.
8. Industrial Heating, Nr 5, 1958, page 924.
9. V. S. Mikheyev, and D. M. Pevtsov, Zhurnal neorganicheskoy khimii (Journal of Inorganic Chemistry), Vol III, Nr 4, 1958.
10. Canadian Machining and Manufacturing News, Nr 9, 1958, pages 152-154.
11. A. Calverley, M. Davis, and R. J. Lever, Journal of Scientific Instruments, Vol 34, 1957, page 142.
12. Buehler, Transactions of the Metallurgical Society AIME, Vol 212, Nr 5, 1959, pages 694-698.
13. D. Williams and W. Pechin, Transactions of the American Society of Metals, Vol 50, 1957, page 54.
14. Ye. M. Savitskiy, M. A. Tylkina, and K. B. Pivovarova, Atomnaya energiya (Atomic Energy), Vol 7, Nr 5, 1959.

15. Ye. M. Savitskiy, Pedkiye metally i splavy (Pure Metals and Alloys), Publishing House of the House of Technology, 1959.
16. I. I. Kornilov and P. S. Polyakov, Trudy Instituta Metallurgii AN SSSR (Works of the Institute of Metallurgy of the Academy of Sciences, U.S.S.R.), Nr 2, Moscow, Publishing House of the Academy of Sciences, U.S.S.P., 1957.
17. B. Poger, D. Atkins, E. Manthos, and M. Kirkpatrick, Advances in Nuclear Engineering, Nr 2, 1957, page 157.
18. H. Wilhelm, O. Carlson, and J. Dickinson, Journal of Metals, Vol 6, Nr 8, 1954.
19. Yu. F. Bychkov, A. N. Rozanov, and D. M. Skorov, Atomnaya energiya (Atomic Energy), Vol II, Nr 2, 1957.
20. V. V. Baron and Ye. M. Savitskiy, Zhurnal neorganicheskoy khimii (Journal of Inorganic Chemistry), Vol IV, Nr 1, 1961.
21. R. Kieffer and F. Benesovsky, Presented Before the Powder Metallurgy Joint Group of the Iron and Steel Institute of Metals, London, 1958.
22. M. Hansen, E. Kamm, H. Kessler, and D. McPherson, Metals, Vol 3, Nr 10, 1951.
23. A. Knapton, Nature, Vol 175, 1955, page 730.
24. H. Goldschmidt, Research, Vol 10, Nr 7, 1957.
25. V. P. Yelyutin and V. F. Funke, Izvestiya ANSSSR, OTN, Metallurgiya i toplivo (News of the Academy of Sciences, U.S.S.R., Department of Technical Sciences, Metallurgy and Fuel), Nr 3, 1956.
26. G. V. Zakharova and others, Niobiy i ego splavy (Niobium and Its Alloys), Moscow, Metallurgizdat, 1961.
27. M. I. Agafonova, V. V. Baron, and Ye. M. Savitskiy, Izvestiya AN SSSR, OTN, Metallurgiya i toplivo (News of the Academy of Sciences, U.S.S.R., Department of Technical Sciences, Metallurgy and Fuel), Nr 5, 1959.
28. R. P. Elliott, Transactions of ASME, Nr 52, 1960, page 990.
29. Reactive Metals, Nr 2, 1958, page 341.
30. Ye. M. Savitskiy, V. F. Terekhova, and I. V. Burov, Zhurnal neorganicheskoy khimii (Journal of Inorganic Chemistry), Vol IV, Nr 6, 1959.
31. O. Carlson, J. Dickinson, H. Lunt, H. Wilhelm, Journal of Metals, Vol 8,

1956, page 2.

32. G. Brauer and R. Hermann, Z. anorgan. und allgem. Chem., Nr 2, 1953, page 274.
33. V. N. Vigdorovich and V. S. Ivleva, Izvestiya AN SSSR, OTN, Metallurgiya i toplivo (News of the Academy of Sciences, U.S.S.R., Department of Technical Sciences, Metallurgy and Fuel), N r 6, 1960, page 51.

6306

CSO: 1879-D

ELECTRON DIFFRACTION AND X-RAY PHOTOGRAPHIC  
INVESTIGATION OF OXIDE FILMS ON NIOBIUM

I. I. Korobkov  
B. N. Revyakin  
Chen' Khe-Min

The question of the structure and composition of oxide films that form during heating of niobium in oxygen and in air is of great interest for an understanding of the mechanism and the kinetics of its oxidation. Many papers have been devoted to a study of this problem. However, different opinions are held concerning the oxidation products of niobium which correspond to the different stages of corrosion.

According to data in literature [1, 2], the stable phases in the niobium-oxygen system are the oxides NbO, NbO<sub>2</sub>, and Nb<sub>2</sub>O<sub>5</sub>. The oxide NbO has a very limited region of homogeneity [1] which is in the range from NbO<sub>0.94</sub> to NbO<sub>1.04</sub>. This oxide melts at 1945°C and has a cubic lattice of the NaCl type with  $a = 4.210 \text{ \AA}$ . Niobium dioxide NbO<sub>2</sub> also has a narrow region of homogeneity which is in the range from NbO<sub>1.94</sub> to NbO<sub>2.09</sub>. The oxide NbO<sub>2</sub> ( $t_{\text{melting}} = 1915^\circ\text{C}$ ) has a tetragonal crystal lattice of the rutile type with the parameters:  $a = 4.844 \text{ \AA}$ ,  $c = 2.99 \text{ \AA}$ , and  $c/a = 0.618$ . The melting temperature of the higher niobium oxide Nb<sub>2</sub>O<sub>5</sub> is 1495°C. Synthetic niobium pentoxide can exist in three modifications: a low temperature modification (T) isomorphic to the oxide Ta<sub>2</sub>O<sub>5</sub> and stable to 900°C; a stable intermediate form (M) between 900 and 1100°C, and a high-temperature modification (H) above 1100°C.

However, in more recent works [3-8] contradictory data have been obtained concerning the number of modifications of Nb<sub>2</sub>O<sub>5</sub> and the temperature ranges in which they exist. The work of Gol'dshmidt [7] was an important contribution to the study of the polymorphism of Nb<sub>2</sub>O<sub>5</sub>. This work is devoted to an x-ray photographic investigation of the oxidation products of niobium directly at high temperatures. It was shown that the low-temperature form of Nb<sub>2</sub>O<sub>5</sub> ( $\alpha = \text{Nb}_2\text{O}_5$  according to Gol'dshmidt)

that forms at temperatures up to 900°C is a metastable modification since it is transformed into the high-temperature form (beta-Nb<sub>2</sub>O<sub>5</sub>) with different speeds depending upon temperature. Beta-Nb<sub>2</sub>O<sub>5</sub> is formed at temperatures of 900-1230°C and does not undergo polymorphic transformations at any rate of cooling to room temperature. The intermediate modification (M-Nb<sub>2</sub>O<sub>5</sub>), discovered by Brauer, in the opinion of Gol'dshmidt is a variation of a structure of the H-form and the transition M to H is associated with a slight change in structure. Above 1280°C there is still another modification which cannot be fixed by quenching [8].

There are also a number of opinions concerning the nature of the dark sublayer of oxide which always exists between the metal and the fluffy layer of light-yellow oxide scale and which determines basically the rate of oxidation of niobium in the process characterized by the linear law. Using the same method of x-ray photographic phase analysis [7, 9], only the Nb<sub>2</sub>O<sub>5</sub> phase was observed in this sublayer (with texture features) while according to the data of Klopp and others [10] a mixture of the phases Nb<sub>2</sub>O<sub>5</sub> and NbO was observed in the transitional layer.

Recently data have been obtained on the oxide phases on niobium that form in the beginning moment of oxidation. As Seybolt showed [11], the solubility of oxygen in the lattice of metallic niobium increases upon an increase in temperature from 775 to 1100°C in the range from 1.38 to 5.52 at.%. Brauer and Muller [12] and Gurlen [13] discovered that under certain oxidation conditions of niobium oxygen can be dissolved in the lattice of the metal above the range noted by Seybolt. The lattice of the niobium is distorted toward being tetragonal; it is assumed [12] that this phase is a suboxide of the Nb<sub>2</sub>O composition. In addition, Gurlen [13] noted another phase also closely associated with the structure of niobium. He designated these two phases as NbO<sub>x</sub> and NbO<sub>y</sub>. Only at niobium oxidation temperatures above 600°C and oxygen pressures of 1 mm of mercury are the phases NbO and NbO<sub>2</sub> revealed in the oxide film from his data obtained by electron diffraction.

It should be noted, however, that no systematic investigations of the structure and composition of oxide films that form on niobium in the different periods of oxidation have been conducted. It is also known that when niobium is heated above 300°C in oxygen or air, depending upon time, oxidation products can form on the specimens which can be arbitrarily divided into four groups:

- (a) thin films of a golden color up to 1000 Å thick that can be studied only by the electron diffraction method;
- (b) thicker black films; they are very strongly linked with the metal and are difficult to process with abrasives; these films are thick enough to be investigated by the electron diffraction and the x-ray photographic method;

(c) a white scale that forms after a certain oxidation time that is characteristic for each temperature; this scale flakes off the specimen easily upon cooling;

(d) a black sublayer of oxide located under the white scale.

This paper reports the results of electron diffraction and x-ray photographic investigation of the phase composition of oxidation products that form on niobium in relation to temperature and oxidation time with isothermic soaking in oxygen (150 mm of mercury) in the temperature range 400-1100°C. A metal was used for the research for which data had already been obtained under the same conditions on the kinetics of oxidation [14].

### Research Methodology

A study of the phase composition of oxides that form on the surface of niobium specimens during isothermic oxidation was made using the electron diffraction and the x-ray photographic method with reflection. The scale which separates from the specimens upon cooling is also studied by the x-ray photographic method (the powder method).

The electron diffraction investigation of oxide films were conducted with a vertical electron diffractor made at MIFI. The distance  $L$  from the object to the photographic plate in the equipment is 50 cm, the size of the photographic plate is 9 x 12 (12 photographic plates are loaded simultaneously into the device), the accelerating voltage can vary from 40 to 80 kilovolts. The constant of the device  $\lambda L$  (where  $\lambda$  is the wave length of the electrons in Å) was determined using a constant standard --a thin layer of aluminum. The standard was put under the first bundle of electrons at a fixed distance (12 cm) from the photographic plate. As a result, two systems of rings were simultaneously photographed: rings from the specimen investigation and from the standard (Figure 1).

Determination of the constant of the equipment led to measurement of the diameters of the very clearly expressed lines of the standard using a comparator and multiplication of the results that were obtained by a scale factor that was found earlier for each step of accelerating voltage. The accuracy in determining the interplanular distances in this method was an average of 0.5%. The x-ray investigation was conducted on copper radiation with a nickel filter obtained using a clearly focused x-ray tube at a voltage of 45 kilovolts. The x-ray photographs were taken in a camera RKU 114 mm in diameter. The research material was technical niobium remelted in a vacuum of 99.9% purity.

The preparation of the surfaces of the specimens for the study using the "reflection" method was the same as for kinetic investigations [14]. In some cases, mainly when thin oxide films were studied, to reduce the oxidation rate in the first moment the surface of the specimens

after being polished with emery paper of different grades was carefully polished with a cloth. Before oxidation the specimens were heated in a vacuum of the order of  $10^{-6}$  mm of mercury to an assigned temperature. Only then was oxygen permitted in the system. After the exposure the heating of the specimen was stopped (the furnace was lowered) and oxygen was simultaneously pumped out of the equipment.

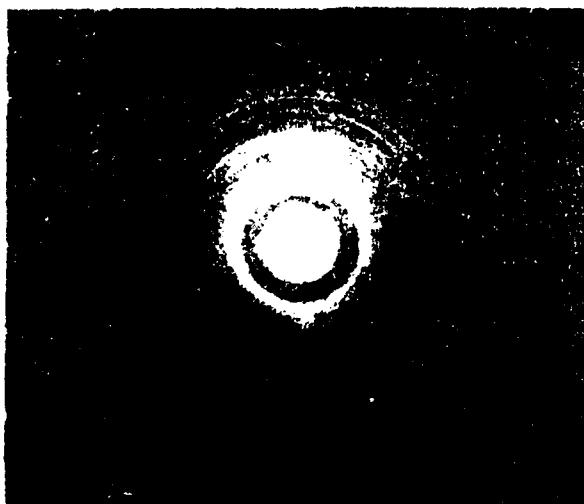


Figure 1. An Electron Diffraction Photograph Obtained Simultaneously From the Surface of a Niobium Specimen Oxidized at 800°C for Five Seconds and a Standard-- a Thin Film of Aluminum.

Table 1 gives the temperatures and the oxidation times of specimens and the characteristics of the oxidation products that form.

Table 1

Length of Oxidation of Niobium Specimens at a Given Temperature Until an Oxide Film of a Definite Type Appears

Temperature, °C	Oxidation time until appearance		
	Thin golden film up to 1000 Å thick	Black film	White scale
400	10 minutes	13 hours	-
500	80 seconds	5 minutes	120 minutes
600	20 "	1 "	120 "
700	10 "	40 seconds	120 "
800	5 "	30 "	180 "
900	5 "	30 "	120 "
1000	3 "	20 "	120 "
1100	-	10 "	120 "

#### A Discussion of the Research Results

The results of electron diffraction and x-ray photographic investigation of the structure and composition of oxide films and of thicker layers--scale--that form on niobium at different temperatures and with different oxidation times are given in Tables 2 and 3. In Table 2 data are given on the interplanular distances of the oxide lattice that forms in the first moment of oxidation (in the first 5-10 seconds) for the temperature range 400-1100°C in the form of thin oxide films of a golden color (Column 1) after some time when the film becomes black (Column 2), and after a longer time sufficient for transformation of the black oxide film into a white oxide (Column 3--sublayer, 4--white scale).

Figure 2, a and b, gives the characteristic x-ray photographs obtained using reflection from the surface of oxidized specimens of niobium. In the same figure (c and d) are the x-ray photographs obtained using the powder method which are characteristic for the white scale which flakes off the specimens. On the basis of data concerning the relative intensities of the lines and the interplanular distances a number of general conclusions concerning the structure and the phase composition of the oxides that form on the surface of niobium during its oxidation in oxygen in relation to temperature and heating time can be made.

Table 2

Interplanular Distances  $d(\text{\AA})$  for Oxides Formed on the Surface  
of Niobium in Oxygen (150 mm of mercury)

At temperatures 400-1100°C (numbers in parentheses are  
intensities of lines: I - strong; II - average; III - weak).

Columns: 1 and 2 - from electron diffraction; 3 and 4 - from x-ray analysis  
(Cu  $K_{\alpha}$ -radiation); 1, 2, and 3 - reflection method; 4 - powder method.

NbO [2]	NbO <sub>2</sub> [2]	Nb <sub>2</sub> O <sub>5</sub>			400° C	
		$\alpha$	M	$\beta$	1	2
		[7]	[1]	[7]		
—	—	3,93 (I)	—	—	3,93 (I)	3,94 (I)
—	—	—	3,76 (I)	3,73 (I)	—	—
—	—	—	3,65 (III)	—	—	—
—	—	—	—	3,62 (I)	—	—
—	—	—	3,57 (I)	—	—	—
—	3,46 (I)	3,48 (III)	—	3,48 (I)	—	—
—	3,37 (III)	—	3,37 (III)	3,34 (II)	—	—
—	—	3,145 (I)	—	3,14 (I)	3,14 (I)	3,14 (I)
—	—	3,085 (I)	—	—	—	—
2,95 (II)	—	—	—	—	—	—
—	2,82 (III)	—	—	2,82 (II)	—	—
—	—	—	2,78 (I)	2,76 (I)	—	—
—	2,73 (III)	2,73 (III)	—	—	—	—
—	—	2,60 (III)	—	—	—	—
—	2,55 (I)	—	2,52 (III)	2,53 (II)	—	2,50 (III)
—	2,44 (III)	2,46 (II)	—	2,47 (II)	2,46 (II)	2,44 (II)
2,42 (II)	—	2,43 (II)	—	—	—	—
—	—	—	2,32 (II)	2,30 (II)	—	—
—	2,26 (III)	—	—	—	—	—
2,10 (I)	2,08 (III)	2,11 (III)	—	2,10 (II)	2,14 (III)	2,12 (II)
—	—	2,01 (II)	2,05 (II)	2,05 (II)	—	—
—	1,98 (III)	1,96 (II)	—	—	—	—
—	1,90 (III)	—	1,91 (II)	1,90 (I)	—	—
1,87 (II)	—	1,87 (III)	—	1,87 (III)	—	—
—	—	1,83 (II)	1,82 (II)	—	1,82 (II)	1,82 (II)
—	1,76 (I)	1,79 (II)	1,78 (II)	1,78 (II)	—	—
1,71 (II)	1,71 (I)	1,74 (III)	1,75 (II)	—	—	—
—	1,64 (III)	1,66 (II)	1,68 (II)	1,68 (I)	1,64 (II)	1,65 (II)
—	1,61 (III)	1,63 (II)	—	—	—	—
—	1,57 (III)	1,57 (II)	1,57 (II)	1,58 (II)	—	—
—	1,54 (II)	—	1,52 (III)	1,52 (III)	—	1,54 (III)
1,48 (I)	—	—	1,45 (III)	—	—	1,48 (II)
1,40 (II)	1,43 (II)	—	1,40 (II)	1,40 (III)	1,41 (II)	—
—	1,37 (II)	—	—	1,39 (III)	—	—
1,38 (II)	—	1,32 (II)	—	—	1,31 (II)	1,33 (III)
—	—	—	1,30 (II)	1,31 (III)	—	—

Table 2 (continued) Part 2

500° C				600° C			
1	2	3	4	1	2	3	4
—	—	3,94 (II)	3,91 (I)	3,93 (II)	—	3,91 (II)	3,91 (I)
—	—	—	—	—	—	—	—
—	—	—	—	—	—	—	—
—	—	—	—	—	—	—	—
—	—	3,48 (III)	—	—	—	3,49 (III)	—
—	—	—	—	—	—	3,46 (III)	—
3,14 (I)	3,13 (I)	3,14 (I)	3,13 (I)	3,14 (I)	3,14 (I)	3,14 (I)	3,13 (I)
—	—	—	3,08 (III)	—	—	—	3,08 (III)
—	—	2,95 (III)	—	2,95 (III)	2,95 (II)	2,91 (III)	—
—	—	—	—	—	—	—	—
—	—	—	—	—	—	—	—
—	2,73 (III)	2,74 (III)	—	—	—	2,74 (III)	—
—	—	2,60 (III)	—	—	—	2,61 (III)	—
—	—	2,52 (II)	—	—	—	2,50 (III)	—
2,46 (III)	2,46 (II)	2,46 (II)	—	2,46 (II)	—	2,45 (III)	2,45 (III)
—	—	2,42 (II)	2,43 (II)	—	—	2,42 (III)	2,42 (III)
—	—	2,34 (I)	—	—	—	2,32 (III)	—
—	—	2,24 (I)	—	—	2,27 (II)	—	—
2,14 (II)	2,13 (II)	2,08 (III)	2,11 (II)	2,11 (III)	2,08 (II)	2,08 (II)	2,11 (II)
—	—	2,02 (III)	—	—	—	2,03 (III)	2,01 (III)
—	1,95 (II)	1,97 (II)	1,95 (II)	—	—	1,97 (II)	1,96 (II)
—	—	1,91 (III)	—	—	—	1,90 (III)	—
—	—	—	—	—	—	—	—
1,82 (II)	1,82 (II)	—	1,81 (II)	1,82 (II)	1,81 (II)	—	1,82 (I)
—	—	1,78 (III)	1,78 (III)	—	—	1,78 (I)	1,78 (III)
—	—	—	—	—	1,75 (II)	1,70 (III)	—
1,64 (II)	1,66 (II)	1,66 (II)	1,66 (II)	1,66 (II)	1,65 (II)	1,68 (III)	1,66 (II)
—	—	1,60 (II)	1,62 (III)	—	—	1,60 (II)	—
—	—	1,57 (II)	1,56 (III)	—	—	—	1,57 (II)
—	1,54 (III)	1,52 (II)	1,53 (III)	—	1,51 (II)	1,52 (II)	—
1,48 (II)	1,48 (II)	1,46 (III)	1,45 (II)	1,48 (II)	1,46 (II)	1,46 (III)	1,44 (II)
—	1,42 (II)	1,40 (III)	—	1,42 (I)	1,41 (II)	—	—
—	—	1,37 (II)	1,37 (II)	—	1,37 (III)	—	1,35 (II)
—	1,33 (III)	1,33 (II)	—	1,32 (III)	1,32 (III)	1,32 (II)	1,32 (III)
—	—	—	—	—	—	—	—

Table 2 (continued) Part 3

700° C				800° C			
1	2	3	4	1	2	3	4
—	3,93 (II)	3,93 (III)	3,91 (I)	—	—	—	3,91 (I)
—	3,74 (II)	3,75 (III)	—	—	3,74 (I)	3,74 (II)	—
—	—	—	—	3,68 (I)	—	—	—
—	3,61 (II)	—	—	3,62 (II)	3,62 (II)	3,62 (III)	—
—	—	—	—	—	—	—	—
—	3,49 (III)	3,48 (III)	—	—	3,49 (III)	3,48 (II)	—
—	—	—	—	3,36 (II)	3,32 (II)	—	—
3,14 (III)	3,14 (III)	3,14 (I)	3,13 (I)	—	—	3,14 (I)	3,13 (I)
—	—	—	3,08 (II)	—	—	—	3,08 (I)
2,94 (II)	2,94 (II)	2,91 (III)	—	2,94 (II)	2,94 (I)	2,94 (II)	—
—	—	—	—	2,83 (III)	2,83 (III)	—	—
—	—	—	—	2,77 (III)	2,77 (III)	2,78 (II)	—
—	—	2,74 (III)	—	—	—	—	—
—	2,59 (III)	2,61 (III)	—	—	—	2,62 (III)	—
2,52 (III)	—	2,50 (II)	—	2,50 (II)	2,51 (III)	2,50 (III)	—
2,45 (II)	2,46 (II)	2,44 (II)	2,45 (II)	—	—	2,46 (II)	2,45 (II)
—	—	—	2,41 (II)	—	—	—	2,41 (II)
2,30 (III)	2,30 (II)	2,32 (II)	—	2,33 (III)	2,32 (III)	2,32 (III)	—
—	—	2,26 (III)	—	2,22 (III)	2,24 (III)	—	—
—	2,11 (III)	2,08 (II)	2,10 (III)	2,10 (III)	2,10 (III)	2,08 (II)	2,10 (II)
—	—	2,03 (III)	2,00 (III)	—	2,02 (III)	2,00 (II)	—
1,97 (II)	1,97 (III)	1,98 (I)	1,96 (II)	—	1,97 (III)	1,97 (II)	1,96 (I)
—	—	1,93 (II)	—	1,90 (I)	1,90 (I)	1,92 (II)	—
1,87 (II)	—	1,88 (III)	—	1,86 (II)	1,86 (III)	1,87 (III)	—
—	—	—	1,81 (I)	1,81 (III)	1,82 (II)	—	1,82 (II)
—	—	1,78 (I)	1,78 (II)	1,76 (II)	1,77 (II)	1,78 (II)	1,78 (II)
1,74 (II)	1,73 (II)	1,73 (III)	—	1,72 (III)	—	1,73 (III)	—
1,69 (II)	—	1,67 (III)	1,65 (I)	1,67 (II)	1,67 (III)	1,68 (III)	1,65 (II)
—	—	1,62 (II)	1,62 (II)	—	1,63 (II)	1,62 (III)	1,62 (III)
—	1,57 (II)	1,57 (II)	1,57 (II)	1,58 (III)	—	1,58 (II)	1,56 (III)
1,54 (II)	1,51 (III)	1,53 (II)	1,53 (II)	1,52 (III)	1,51 (III)	1,52 (III)	1,53 (III)
1,45 (II)	1,44 (II)	1,46 (III)	1,45 (II)	1,44 (II)	1,45 (II)	1,45 (III)	1,45 (III)
1,42 (II)	—	1,40 (III)	1,42 (III)	1,40 (II)	1,40 (II)	—	1,41 (III)
1,35 (III)	1,37 (III)	1,35 (II)	1,34 (III)	1,37 (III)	1,38 (III)	—	—
1,32 (III)	1,32 (III)	—	1,32 (III)	—	1,34 (III)	1,32 (III)	1,33 (II)
—	—	—	—	—	—	—	—

Table 2 (continued) Part 4

900° C				1000° C				1100° C	
1	2	3	4	1	2	3	4	2	4
—	—	3,94 (III)	—	—	—	—	—	—	—
3,75 (I)	3,73 (I)	3,73 (I)	3,72 (I)	3,75 (I)	3,72 (I)	3,73 (I)	3,73 (I)	3,76 (I)	3,72 (II)
—	—	—	—	—	3,68 (III)	—	—	—	—
—	—	3,60 (III)	3,62 (I)	—	—	—	—	—	—
3,55 (II)	3,55 (II)	—	—	3,55 (II)	—	3,54 (III)	—	3,56 (II)	—
—	—	3,47 (III)	3,47 (I)	—	—	—	3,48 (I)	—	3,47 (I)
3,36 (II)	3,35 (II)	3,35 (III)	3,35 (III)	3,36 (II)	3,34 (II)	—	3,35 (III)	3,36 (III)	3,33 (II)
—	3,16 (III)	3,14 (III)	—	—	3,14 (III)	—	—	—	—
—	—	3,07 (III)	—	—	—	—	—	—	—
—	—	2,96 (III)	—	—	—	2,96 (II)	—	—	—
2,81 (II)	—	—	2,82 (II)	2,81 (II)	—	—	2,82 (II)	—	2,82 (II)
—	2,78 (I)	2,78 (II)	2,77 (II)	—	2,78 (I)	—	2,76 (II)	2,78 (I)	2,76 (II)
—	—	—	2,70 (III)	—	—	—	2,70 (II)	—	2,70 (II)
—	—	2,60 (III)	—	—	—	—	—	—	—
2,53 (III)	2,51 (III)	2,51 (III)	2,53 (III)	2,53 (II)	2,52 (III)	2,52 (III)	2,53 (II)	2,53 (III)	2,53 (II)
—	—	2,46 (III)	2,50 (II)	—	—	—	2,48 (III)	—	2,48 (III)
—	—	—	—	—	—	2,40 (III)	—	—	—
2,32 (III)	2,30 (III)	2,31 (III)	2,30 (II)	2,32 (II)	2,33 (II)	—	2,31 (III)	2,32 (III)	2,31 (II)
—	—	—	—	—	—	2,24 (III)	—	—	—
—	2,08 (III)	2,08 (III)	—	—	—	2,08 (II)	2,08 (II)	—	2,08 (II)
—	—	2,02 (III)	—	—	—	2,02 (II)	2,03 (II)	—	—
—	—	—	—	—	—	—	—	—	—
1,90 (I)	1,90 (II)	—	1,90 (I)	1,90 (I)	1,90 (I)	1,91 (III)	1,90 (I)	1,90 (III)	1,90 (I)
1,87 (III)	1,86 (III)	1,87 (II)	—	1,87 (III)	1,86 (II)	1,86 (I)	—	—	—
—	—	1,83 (III)	1,82 (II)	—	1,82 (III)	1,82 (III)	1,81 (III)	—	1,81 (II)
1,78 (II)	1,76 (II)	1,78 (II)	1,78 (II)	1,78 (II)	1,77 (III)	1,78 (III)	1,78 (II)	1,78 (III)	1,78 (III)
—	—	1,74 (II)	1,73 (III)	—	—	1,74 (III)	1,73 (III)	—	1,73 (II)
1,68 (I)	1,68 (I)	—	1,68 (II)	1,68 (I)	1,68 (I)	1,68 (II)	1,68 (II)	1,68 (I)	1,68 (I)
—	—	1,63 (III)	—	—	1,62 (III)	1,62 (III)	1,63 (II)	—	1,62 (II)
1,58 (III)	1,57 (III)	1,58 (III)	1,57 (II)	1,58 (III)	—	—	1,56 (II)	1,58 (I)	1,58 (III)
1,52 (II)	1,51 (II)	1,52 (III)	1,53 (III)	1,52 (II)	1,52 (II)	1,52 (II)	1,52 (II)	—	1,52 (II)
—	—	1,45 (III)	1,45 (III)	—	—	1,45 (III)	1,45 (III)	1,45 (II)	1,45 (II)
1,40 (III)	1,40 (II)	1,41 (III)	1,40 (II)	1,40 (II)	1,40 (II)				
—	—	—	—	—	—	—	—	—	—
—	1,33 (II)	1,33 (III)	—	—	—	—	—	—	—
1,30 (III)	1,30 (II)	—	1,30 (III)	1,30 (III)	1,30 (III)	—	1,30 (III)	1,30 (III)	1,30 (III)

Table 3

Oxide Phases That Form on the Surface of Niobium  
in Relation to Temperature and Oxidation Time

Temperature °C	Thin oxide film up to 1000 Å thick	Thick oxide film up to 10 microns thick		White scale
		Electron diffraction	X-ray photography	
400	$\alpha'$ -Nb <sub>2</sub> O <sub>5</sub>	$\alpha'$ -Nb <sub>2</sub> O <sub>5</sub>	—	—
500	$\alpha'$ -Nb <sub>2</sub> O <sub>5</sub>	$\alpha'$ -Nb <sub>2</sub> O <sub>5</sub>	$\alpha'$ -Nb <sub>2</sub> O <sub>5</sub> + NbO*	$\alpha$ -Nb <sub>2</sub> O <sub>5</sub>
600	$\alpha'$ -Nb <sub>2</sub> O <sub>5</sub>	$\alpha'$ -Nb <sub>2</sub> O <sub>5</sub> : NbO*	$\alpha'$ -Nb <sub>2</sub> O <sub>5</sub> + NbO* + NbO*	$\alpha$ -Nb <sub>2</sub> O <sub>5</sub>
700	$\alpha'$ -Nb <sub>2</sub> O <sub>5</sub> : + NbO*	$\alpha'$ -Nb <sub>2</sub> O <sub>5</sub> + NbO* : $\beta$ - Nb <sub>2</sub> O <sub>5</sub>	$\alpha'$ -Nb <sub>2</sub> O <sub>5</sub> + $\beta$ - Nb <sub>2</sub> O <sub>5</sub> + NbO*	$\alpha$ -Nb <sub>2</sub> O <sub>5</sub>
800	$\beta'$ -Nb <sub>2</sub> O <sub>5</sub>	$\beta$ -Nb <sub>2</sub> O <sub>5</sub> : NbO*	$\alpha'$ -Nb <sub>2</sub> O <sub>5</sub> : $\beta$ - Nb <sub>2</sub> O <sub>5</sub> + NbO*	$\beta$ -Nb <sub>2</sub> O <sub>5</sub>
900	$\beta'$ -Nb <sub>2</sub> O <sub>5</sub>	$\beta'$ -Nb <sub>2</sub> O <sub>5</sub> + $\alpha'$ - Nb <sub>2</sub> O <sub>5</sub>	$\beta$ -Nb <sub>2</sub> O <sub>5</sub> : $\alpha$ - Nb <sub>2</sub> O <sub>5</sub> + NbO*	$\beta$ -Nb <sub>2</sub> O <sub>5</sub>
1000	$\beta'$ -Nb <sub>2</sub> O <sub>5</sub>	$\beta'$ -Nb <sub>2</sub> O <sub>5</sub>	$\beta'$ -Nb <sub>2</sub> O <sub>5</sub> + NbO*	$\beta$ -Nb <sub>2</sub> O <sub>5</sub>
1100	—	$\beta'$ -Nb <sub>2</sub> O <sub>5</sub>	—	$\beta$ -Nb <sub>2</sub> O <sub>5</sub>

\* Oxides designated arbitrarily.



Figure 2. X-Ray Photographs Obtained From the Surface of Niobium Specimens Oxidized for Two Hours: a--800°C, a black sublayer (reflection method); b--800°C, a white scale (powder method); c--900°C, a black sublayer (reflection method); d--900°C, a white scale (powder method).

First, it can be noted that the composition of the white scale that flakes off the specimen corresponds to that of niobium pentoxide  $Nb_2O_5$ . Up to 800°C inclusively the structure of this oxide corresponds to the alpha-modification (the low-temperature form) and at 900°C and above it corresponds to the beta-modification. These data agree well with the results obtained in the work of Gol'dshmidt [7] on niobium specimens when they oxidize in air. The values of the relative intensities and the interplanular distances that we obtained agree well with the values given in this work.

There was not such close agreement between the indicated tabular data, however, for oxides in the form of thin oxide films that form on

niobium in the first moment of oxidation or in the form of a dark sublayer which always occurs between the metal and the fluffy white scale in the later stage of oxidation. According to the electron diffraction and x-ray photographic data obtained by reflection, the composition of the indicated oxide layers on the niobium correspond also basically to the oxide  $\text{Nb}_2\text{O}_5$ .

However, the structure of this oxide is somewhat different from the well known phases alpha- and beta- $\text{Nb}_2\text{O}_5$  in the electron diffraction and x-ray photographs obtained from the surfaces of specimens oxidized at temperatures up to  $800^\circ\text{C}$  this difference is revealed first of all by the absence of strong lines with  $d = 3.08$  and  $2.42$  Å. The ratios of the intensities of certain lines also can be distorted (see Figure 2). At  $900^\circ\text{C}$  and above an oxide phase similar in structure to beta- $\text{Nb}_2\text{O}_5$  is revealed in these films. As seen from Table 2, this phase can be identified just as the M-modification of Brauer [1]. Considering the data of Gol'dshmidt [7] the M-phase should be considered to be a variation of the structure beta- $\text{Nb}_2\text{O}_5$ . Considering the differences in the structure of the oxide phases observed in the films strongly bound to the metal and the structure of oxides that flake off the metal (alpha- and beta-modifications of  $\text{Nb}_2\text{O}_5$ ), we designated the first oxide as alpha'- and beta'- $\text{Nb}_2\text{O}_5$ . Figure 2 gives the x-ray photographs obtained by reflection from the black sublayer and by the powder method from the white scale. They illustrate the differences in the phases at  $800^\circ\text{C}$  (a, b) and  $900^\circ\text{C}$  (c, and d).

As seen from Table 2, the structure of the primary oxide films that form on niobium in the first moment of oxidation undergo a change during growth in isothermic oxidation. The character of the structural changes depends basically on the oxidation temperature. Thus, at  $500$ - $800^\circ\text{C}$  the golden film alpha'- $\text{Nb}_2\text{O}_5$  that formed in the first moment of oxidation (see Table 2, Column 1), after a certain time is transformed into alpha- $\text{Nb}_2\text{O}_5$ . In the electron diffraction photographs corresponding to the dark films firmly linked to the metal (see Table 2, Column 2), in addition to the lines corresponding to the alpha prime-modification of  $\text{Nb}_2\text{O}_5$ , a number of lines not inherent to this modification are revealed.

It was not possible to compare the values of the interplanular distances  $d$  from any phase in the niobium-oxygen system. There is only approximate agreement with the values  $d$  published for phases  $\text{NbO}$  and  $\text{NbO}_2$ . In the x-ray photographs obtained from these same specimens but oxidized for a longer time (see Table 1) similar systems of lines were obtained (a number of lines appeared as a result of the low thickness of the film correspond to the cubic lattice of niobium). Judging from the intensity of the lines on the electron diffraction photographs and the x-ray photographs the amount of phase alpha'- $\text{Nb}_2\text{O}_5$  in the film is increased as thickness increases. In the final analysis, as was noted above, the structure of the scale that flakes off the specimen which formed at  $400$ - $800^\circ\text{C}$  corresponds to the oxide alpha- $\text{Nb}_2\text{O}_5$ . At a temperature of  $800^\circ\text{C}$  and above in the first moment of oxidation there is formed a thin oxide film close with respect to structure to the medium-temperature

modification  $\beta'$ - $\text{Nb}_2\text{O}_5$ . With the passage of time of isothermic oxidation at  $900^\circ\text{C}$  and above there is observed a gradual transition of  $\beta'$ - $\text{Nb}_2\text{O}_5$  to the  $\beta$ -modification. In the dark oxide films that form at temperatures below  $900^\circ\text{C}$  some amount of  $\alpha$ -modification of  $\text{Nb}_2\text{O}_5$  is also revealed.

The fact of the formation of the low-temperature form of  $\alpha$ - $\text{Nb}_2\text{O}_5$  on niobium at temperatures above  $800^\circ\text{C}$  and its transformation into the  $\beta$ -modification agrees with the conclusions of Gol'dshmidt [7]. The formation of the high-temperature modification of  $\text{Nb}_2\text{O}_5$  in the first period of oxidation beginning from  $700^\circ\text{C}$  (see Table 3), established in this research, also does not contradict the results of this work. The formation of this modification on the surface of niobium, as is known was normally observed at temperatures only above  $800^\circ\text{C}$  [5, 7]. The appearance on electron diffraction and x-ray photographs of lines of the  $\beta'$ - $\text{Nb}_2\text{O}_5$  phase is associated with the short-time increase in the temperature of the specimens surface in the initial moment of isothermic oxidation. Measurement of the temperature of the surface of specimens during their oxidation showed that the oxidation temperature can be  $100^\circ\text{C}$  higher than the temperature of the furnace due to the heat of the formation of oxides.

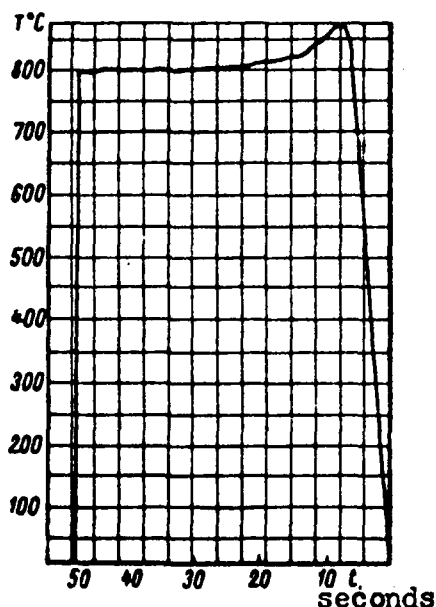


Figure 3. Graph of the Automatic Recording of the Temperature of a Specimen From the Moment it is Placed Into the Furnace Heated to  $800^\circ\text{C}$ .

These data were obtained using a Chromel-Alumel thermocouple 0.1 mm in diameter fastened to the specimen. Figure 3 shows the graph of the temperature of the specimen inscribed in the equipment EPP-09 in the first moment of oxidation. As seen from the graph, the overheating of the surface of the specimen at 800°C lasted 10 seconds in all. This overheating can be explained by the formation of an oxide phase corresponding to higher temperatures on the surface of niobium at 700°C and above.

It also should be noted that at temperatures above 700°C textured oxides were revealed in the dark films that are firmly linked to the metal. In addition, during the process of growth of the oxide films slight structural changes are observed which are manifest in a change in the relative intensities, formation of new doublets, and a change in the position of certain diffraction lines.

### Conclusions

Electron diffraction and x-ray photographic investigation of the phase composition of oxides on niobium in contact with metal and flaked off of it after oxidation in oxygen (150 mm of mercury) in the temperature range 400-1100°C was conducted. As a result, it was established that:

1. The structure of oxide films firmly bonded to the metal, in relation to the temperature, more or less are different from niobium oxides that have already flaked off the specimen.
2. In the temperature range 700-900°C a mixture of the phases  $\alpha'$ -Nb<sub>2</sub>O<sub>5</sub> and  $\beta'$ -Nb<sub>2</sub>O<sub>5</sub> is observed in these oxide films. As the temperature is raised the amount of the phase  $\alpha'$ -Nb<sub>2</sub>O<sub>5</sub> is reduced and the amount of  $\beta'$ -Nb<sub>2</sub>O<sub>5</sub> is increased.

### BIBLIOGRAPHY

1. G. Z. Brauer, Z. anorgan. und allgem. Chem., Nr 248, 1941, page 1.
2. V. Elliott, Problemy sovremennoy metallurgii (Problems of Modern Metallurgy), Nr 5, Moscow, Publishing House of Foreign Literature, 1960, page 128.
3. L. Frevel and H. Rinn, Analytical Chemistry, Nr 27, 1955.
4. M. Schafer, A. Durkop, and M. Jori, Z. anorgan. und allgem. Chem., Nr 275, 1954.
5. D. Bridges and W. Fassel, Journal of the Electrochemical Society, Vol 103, 1956.

6. F. Holtzberg, A. Reisman, M. Berry, and M. Berkenblit, Journal of the American Chemical Society, Vol 79, 1957.
7. Gol'dshmidt, V sb.: Niobiy i tantal (In the collection: Niobium and Tantalum), Editor: O. P. Kolchin, Moscow, Publishing House of Foreign Literature, 1960.
8. M. Schafer and R. Roy, Z. Kristallogr., Vol 110, 1958.
9. V. I. Arkharov, A. F. Gerasimova, and T. V. Ushakova, Fizika metallov i metallovedeniye, Vol 12, Nr 5, 1961, page 761.
10. Klopp, Sims, and Jaffee, V sb.: Problemy sovremennoy metallurgii (In the collection: Problems of Modern Metallurgy) Nr 3, Moscow, Publishing House of Foreign Literature, 1960, page 51.
11. A. Seybolt, Journal of Metals, Nr 6, 1954.
12. G. Brauer and H. Muller, Mineral Chemistry, Butterworth, London, 1958.
13. T. Gurlen, V sb.: 26-y Mezhdunarodnyy kongress liteyshchikov (In the collection: 26-th International Congress of Founders), Moscow, Mashgiz, 1961.
14. B. N. Revyakin, I. I. Korobkov, A. I. Yevstyukhin, and V. S. Lyashenko, V sb.: Metallurgiya i metallovedeniye chistykh metallov (In the collection: Metallurgy and Metal Science of Pure Metals), Nr III, Moscow, Gosatomizdat, 1961, page 175.

6306

CSO: 1879-D

INVESTIGATION OF THE KINETICS OF THE OXIDATION OF  
IODIDE NIOBIUM REFINED BY THE ELECTRON-BEAM METHOD

I. I. Korobkov  
B. N. Revyakin  
Chen' Khe-Min

In investigating the kinetics of the oxidation of niobium [1] two phenomena were noted which to some degree can be associated with additions in the metal. They are the basic scattering of the values of the oxidation rate in isothermic oxidation of niobium of different melts and the anomalous relation of the oxidation rate to temperature in the range 800-900°C. To clarify these phenomena this problem was examined once again and experiments were conducted on specimens of purer metal.

Since publication of our first paper, works have appeared which are devoted to investigation of the oxidation of niobium in oxygen and in air [2-5]. As a result of these investigations certain features of the kinetics of metal oxidation were established and partly confirmed. They include the reduction in the oxidation rate of niobium upon an increase in temperature in the range 600-650°C [2, 3, 5] when the metal and the oxide that forms on it do not undergo polymorphic transformations. The anomalously high oxidation rate of niobium in air at 800°C that was noted in the work of Klopp and others [6] was subsequently confirmed when it was oxidized in oxygen [1, 4]. In our opinion, however, the reduction in the oxidation rate with an increase in temperature in the range 800-900°C should be considered an anomaly. This effect, according to our data, and also the data of other works [1, 4], is associated with the formation at these temperatures of different modifications of the oxide Nb<sub>2</sub>O<sub>5</sub>: alpha-Nb<sub>2</sub>O<sub>5</sub> at 800°C and beta-Nb<sub>2</sub>O<sub>5</sub> at 900°C.

This paper reports the results of research on the oxidation kinetics of niobium of high purity in the temperature range 350-1200°C in intervals of 20-30°. Data on the relation of the oxidation rate of niobium to the oxygen pressure for temperatures 400, 625, and 1000°C are also reported.

## The Research Materials and Methodology

To refine the initial niobium (99.9% pure) of additions it was subjected to iodide refining by the methodology developed in the laboratory of MIFI [7]. Then, rods of the iodide niobium were remelted in an electron-beam furnace in a vacuum of the order of  $10^{-5}$  mm of mercury; the Brinell hardness of the remelted niobium was  $40 \text{ kg/mm}^2$ . That is, it was considerably lower than in other types of niobium (the hardness of niobium remelted in an electron-beam furnace without iodide refining was  $70-75 \text{ kg/mm}^2$ ). The ingot of metal that was obtained was cold rolled without intermediate anneals into a sheet 1 mm thick. Then specimens were cut from this sheet for kinetic investigations. The specimens were  $17 \times 8 \times 0.9 \text{ mm}$ . The kinetics of the oxidation of niobium were studied using the method of continuous measurements of the gain in weight of the specimens in special vacuum glass micro-scales in an atmosphere of oxygen.

Basically the research was conducted at an oxygen pressure of 150 mm of mercury which corresponds approximately to the partial pressure in air. Besides, at 400, 625, and  $1000^\circ\text{C}$  the kinetics of oxidation of niobium were studied in the range of oxygen pressures from 20 to 760 mm of mercury. The oxygen was obtained and cleaned using the methodology described earlier [1]. At temperatures of 350, 400, and  $450^\circ\text{C}$  a study of the kinetics of oxidation of niobium was conducted on torsion micro-scales [1] with a sensitivity of  $2 \times 10^{-6}$  grams and at temperatures of  $500^\circ$  and above-- on specially designed quartz spring scales with a sensitivity of  $3 \times 10^{-6}$  grams (Figure 1).

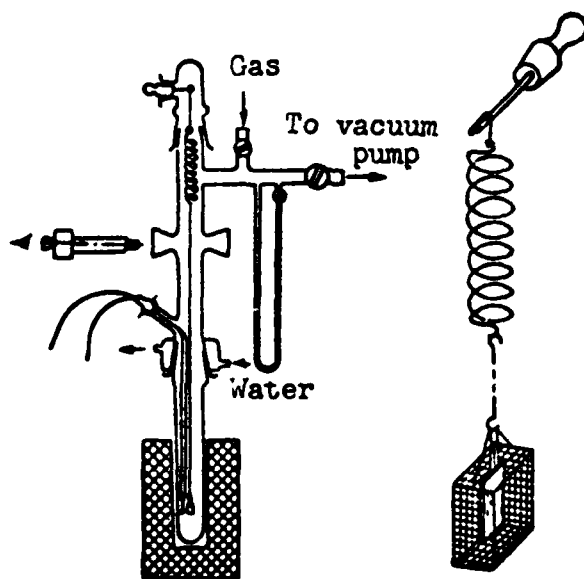


Figure 1. Drawing of Glass Vacuum Micro-Scales With a Quartz Spring.

So that the flaking off of scale during oxidation would not affect the weighing results, the niobium specimen was suspended on a platinum wire 0.1 mm in diameter inside a basket made from fine platinum wire in which the scale was caught. The basket with the specimen was hung on the balance arm of the scales or a spring using a quartz filament. The specimen was fitted with a platinum-rhodium thermocouple to measure the temperature of the specimen. After the scales were evacuated to a vacuum of the order of  $10^{-6}$  mm of mercury a furnace heated to the required temperature was mounted on a quartz hood in which the specimen was placed. In 20 minutes a thermal balance was reached in the working space and then oxygen was admitted for 30 seconds. The temperature in the furnace was maintained with an accuracy of plus or minus  $3^{\circ}\text{C}$ .

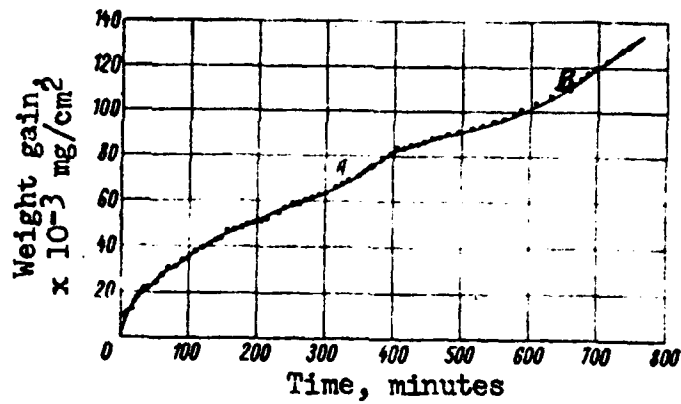
Before investigation the specimens were carefully polished on emery paper of different grades up to No. 20 and then were washed in acetone and alcohol. Data were obtained for each temperature, as a rule, in three specimens. The reproducibility of the results in oxidation of different specimens under these conditions was satisfactory; deviations from average values did not exceed 5%.

### Results of the Research

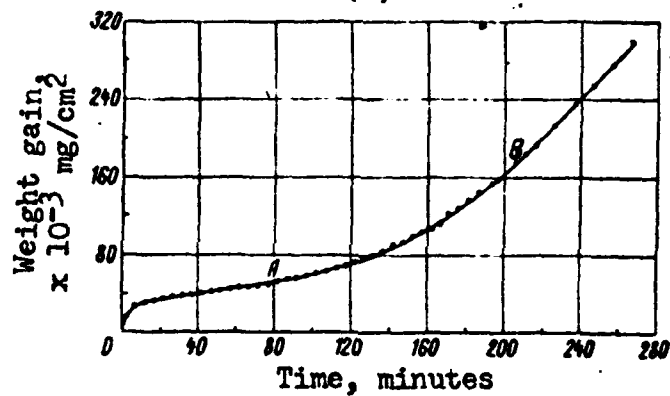
Figures 2-4 give the results of investigation of the kinetics of the oxidation of niobium in oxygen at a pressure of 150 mm of mercury in the temperature range  $350-1200^{\circ}\text{C}$ . Different features in the kinetics of metal oxidation were observed depending upon temperature.

In the temperature range  $350-400^{\circ}\text{C}$  (see Figure 2), on the curves of the oxidation in the coordinates weight-time there are clearly expressed two sections which characterize the different periods of niobium oxidation. In the first period there is a parabolic time law if the very beginning stage of oxidation which lasts several seconds is not considered. This is confirmed by the data presented in Figure 5 where the relation of the squares of the weight gain to time is shown for each temperature.

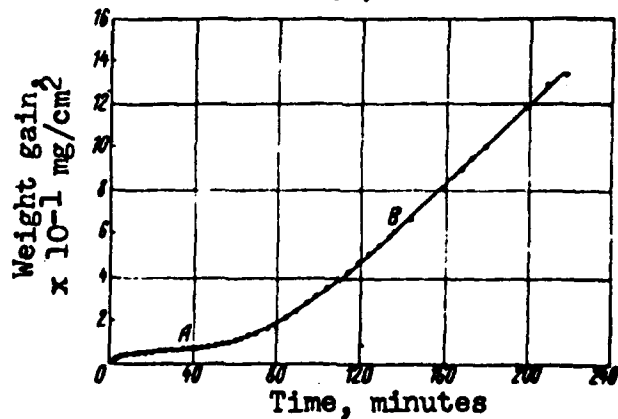
After some time the parabolic law becomes linear which is characteristic for the second period of oxidation. The transition to the linear law occurs after a gradual increase in the oxidation rate over the rate observed at the end of the parabolic segment. This so-called transitional stage is designated in Figure 2 by AB. Figure 6 shows that the duration of the first period of oxidation and also of the initial stage depends basically on the temperature of oxidation. The time in which the parabolic law is observed (the first stage) is shortened with an increase in temperature (see Figure 6) according to the exponential law. According to this same law the duration of the transitional stage also is shortened. But the gain in weight corresponding to the beginning of the accelerated oxidation, in the temperature range  $350-500^{\circ}\text{C}$ , remains the same and is 0.5 milligrams per square centimeter.



(a)



(b)



(c)

Figure 2. Oxidation of Niobium in the Temperature Range 350-400°C in Oxygen at a Pressure of 150 mm of Mercury: a-350°C; b-375°C; c-400°C.

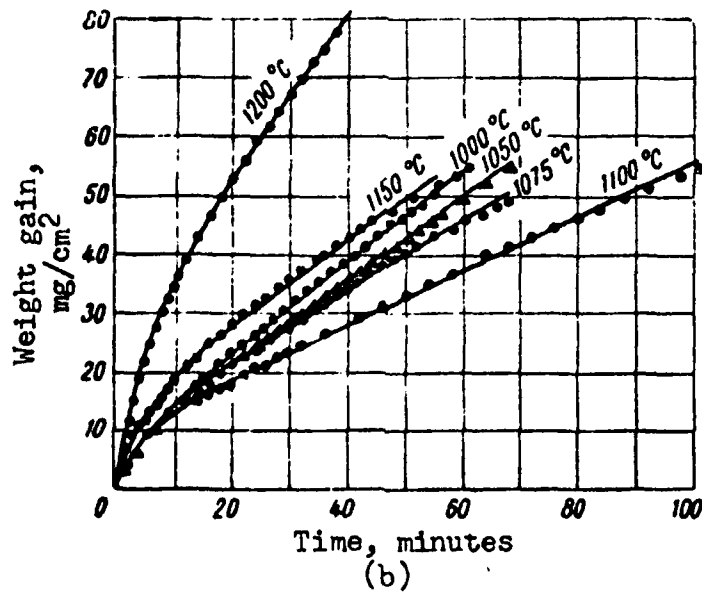
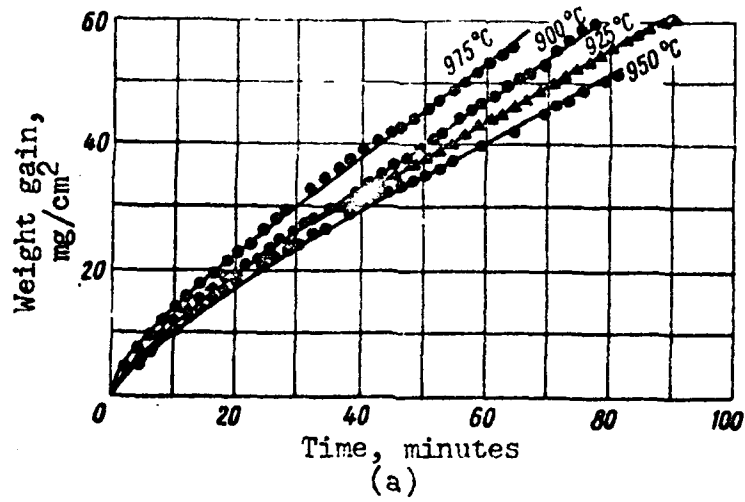


Figure 3. Oxidation of Niobium in the Temperature Range 900-1200°C in Oxygen at a Pressure of 150 mm of Mercury: a--950-975°C; b--1100-1200°C.

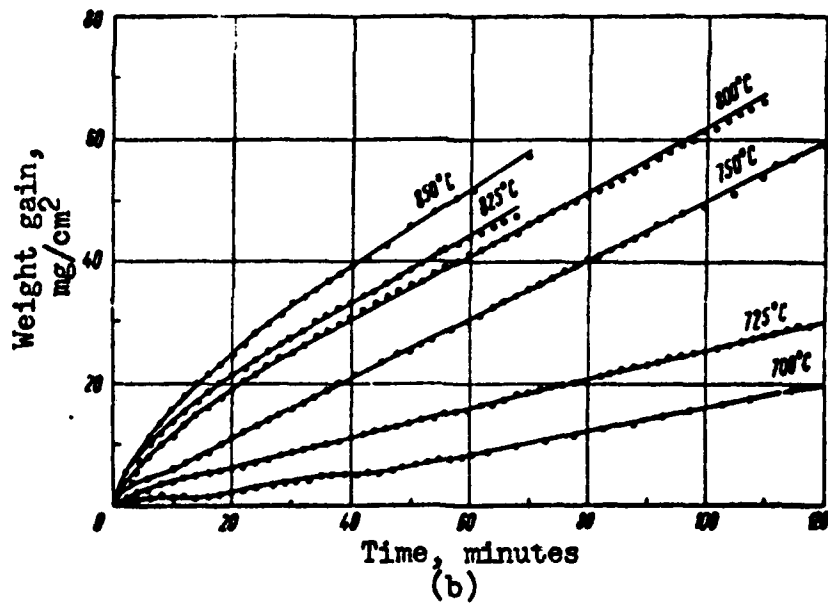
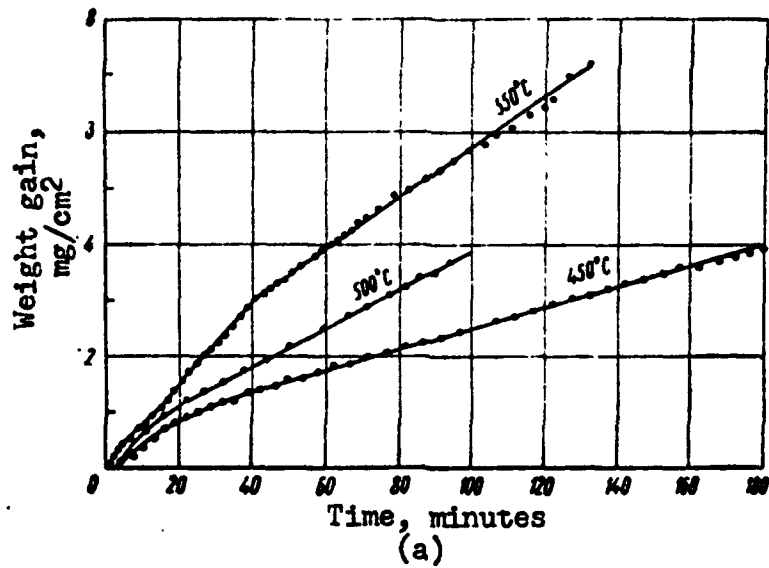


Figure 4a and b. Oxidation of Niobium in the Temperature Range 450-850°C in Oxygen at a Pressure of 150 mm of Mercury: a--450-550°C; b--600-675°C.

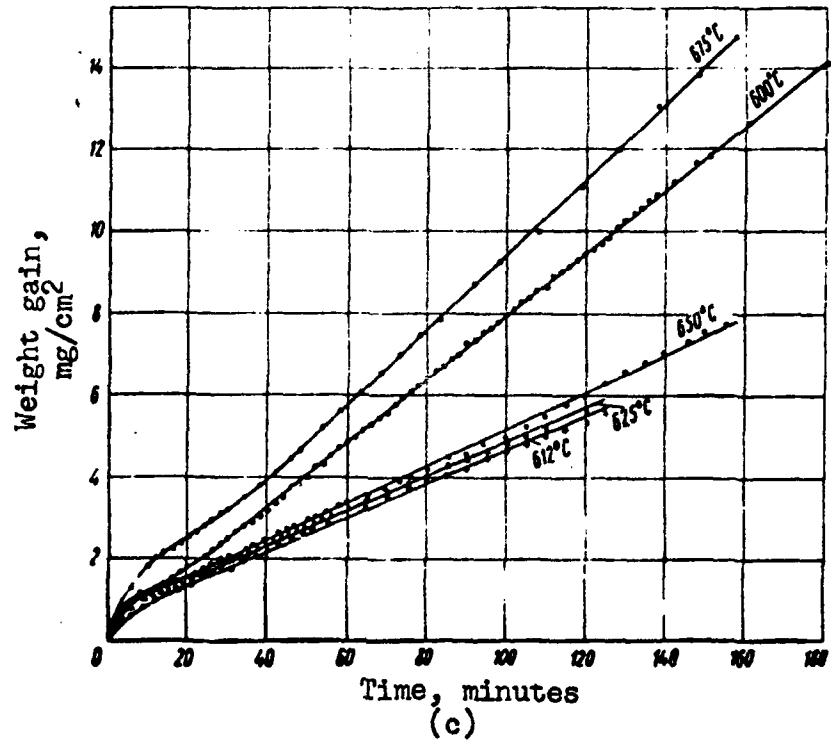


Figure 4c. Oxidation of Niobium in the Temperature Range 450-850° C in Oxygen at a Pressure of 150 mm of Mercury: c -- 700-850° C

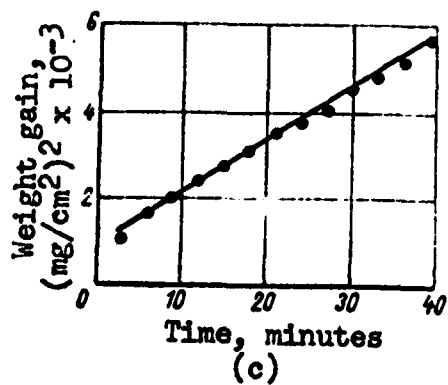
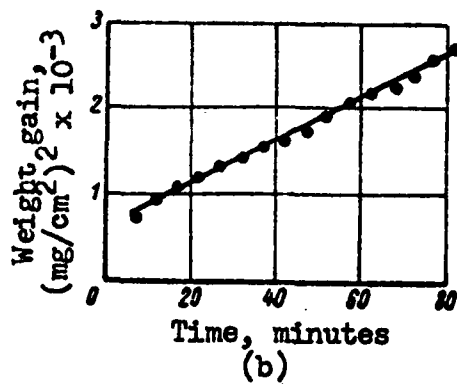
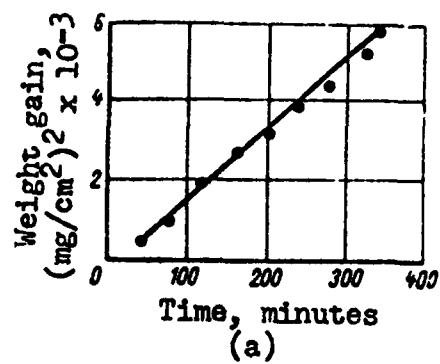


Figure 5. Relation of the Squares of the Weight Gains to Time:  
 a--350°C; b--375°C; c--400°C.

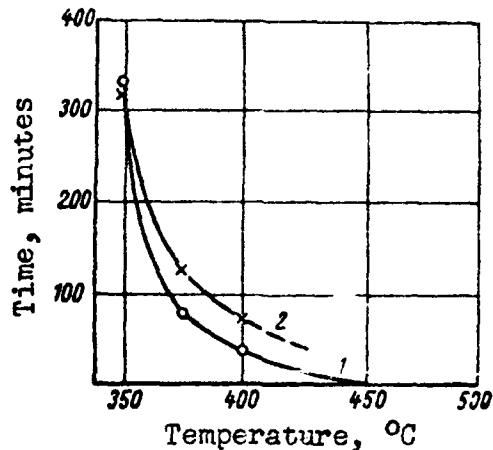


Figure 6. Relation of Oxidation Time According to the Parabolic Law (1) and the Transitional Stage (2) to Temperature.

From visual observation the parabolic law of oxidation occurs in the formation on the specimens surface of a continuous oxide film that is black or dark gray in color and is firmly bonded to the metal. An increase in the oxidation rate of niobium and the transition to the linear law coincide with the appearance on the surface of the specimens of a white oxide which has a very porous structure. The white oxide is not firmly bonded to the lower layer of oxide and flakes off the specimen easily when it is cooled.

We also observed the formation of oxide films of a dark color at higher temperatures. However, their duration at temperatures above 500°C was less than 1 minute.

Figure 7 is a microphotograph of a specimen of oxidized niobium. A sublayer of black oxide film can be clearly seen on the boundary with a metal. The greatest part of the scale is the exfoliating white oxide. Therefore, it can be concluded that the cracking of the white scale occurs parallel to the metal surface. It should be noted that the white oxide that formed at low temperatures (up to 450°C) is a powdery product and at higher temperatures (above 700°C) the white oxide flakes off the specimen in plates of the same size as the oxidized surface of the metal (Figure 8). With an increase in the oxidation temperature the strength of the layer of scale that is white is increased. This is especially noticeable at temperatures in the range 900-1200°C.



3

Figure 7. Microphotograph of an Oblique Cross Section of a Niobium Specimen Oxidized at 612°C for Two Hours: 1--metal; 2--sublayer of oxide; 3--white scale.

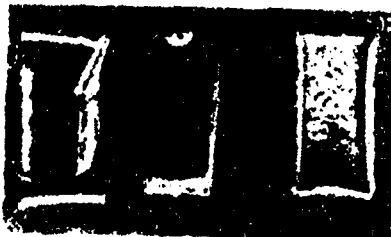


Figure 8. External Appearance of Specimens and Exfoliated Scale After Oxidation at Various Temperatures: a--600°C; b--800°C; c--1100°C.

At temperatures of 450 and 500°C parabolic segments on the curves of oxidation, as seen in Figure 3, have short duration. At temperatures above 500°C, on the oxidation curves neither the parabolic segment nor the transitional stage which are characteristic for lower temperatures are revealed. At certain temperatures (550, 650, 675, 700°C and others) the linear law is established only 40-50 minutes after the beginning of oxidation. During the period before the establishment of the linear law a periodic increase and reduction in the oxidation rate is observed; these fluctuations in the oxidation rate are not reproduced accurately from experiment to experiment. However, the over-all character of the oxidation curves is retained.

Thus, on the basis of what has been given, it can be concluded that the oxidation process in all of the investigated temperature ranges (350-1200°C) can be described by the linear equation

$$\Delta m = Kt + c$$

where  $\Delta m$  is the weight gain, grams/sq cm;  $t$  is the time, seconds;  $K$  is the constant of the linear law of oxidation, grams/sq cm x seconds;  $c$  is the constant characterising the unestablished process.

The table below gives the values of the constant  $K$  for various temperatures and Figure 9 shows the relation of  $\lg K$  to  $\frac{1}{T}$  where  $T$  is absolute temperature. It can be seen from Figure 9 that the linear relation of the logarithm of the constant of the linear law to the reverse absolute temperature which is normal for most metals occurs for niobium only in the temperature range 400-600°C. The value of the energy of activation of niobium oxidation computed from this segment of the line was equal to 13 kilocalories/mol.

Table of the Values of Constant  $K$  of the Linear Law of Oxidation Rate of Iodide Niobium in Oxygen (150 mm of Mercury)

Temperature °C	$K$ , grams/ cm <sup>2</sup> · second	Temperature °C	$K$ , grams/ cm <sup>2</sup> · second
350	$5.5 \cdot 10^{-8}$	800	$8.13 \cdot 10^{-6}$
375	$3.34 \cdot 10^{-8}$	825	$8.93 \cdot 10^{-6}$
400	$1.53 \cdot 10^{-7}$	850	$1.07 \cdot 10^{-5}$
450	$3.41 \cdot 10^{-7}$	900	$1.17 \cdot 10^{-5}$
500	$6.53 \cdot 10^{-7}$	925	$9.17 \cdot 10^{-6}$
550	$7.92 \cdot 10^{-7}$	950	$8.43 \cdot 10^{-6}$
600	$1.31 \cdot 10^{-6}$	975	$1.21 \cdot 10^{-5}$
612	$6.9 \cdot 10^{-7}$	1000	$1.24 \cdot 10^{-5}$
625	$7.15 \cdot 10^{-7}$	1050	$1.12 \cdot 10^{-5}$
650	$7.65 \cdot 10^{-7}$	1075	$9.91 \cdot 10^{-6}$
675	$1.49 \cdot 10^{-6}$	1100	$7.54 \cdot 10^{-6}$
700	$3.28 \cdot 10^{-6}$	1150	$11.1 \cdot 10^{-6}$
750	$7.5 \cdot 10^{-6}$	1200	$2.42 \cdot 10^{-5}$

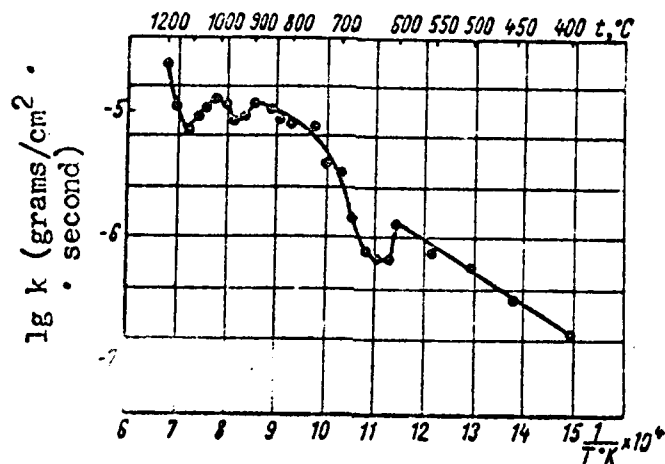


Figure 9. The Relation of the Logarithm of the Constant of the Linear Law of the Oxidation Rate of Niobium to the Reverse Absolute Temperature

At temperatures above  $600^\circ\text{C}$  the relation of the oxidation rate of niobium to temperature is complex. The over-all feature as at lower temperatures is an increase in the oxidation rate with an increase in the temperature. However, it is seen from the table that in the temperature range from  $600$  to  $1200^\circ\text{C}$  there are intervals where the oxidation rate is reduced with an increase in temperature. Thus, upon an increase in temperature from  $600$  to  $612^\circ\text{C}$  the oxidation rate is reduced from  $1.31 \times 10^{-6}$  to  $6.9 \times 10^{-7}$  grams/sq cm x second. With an increase in temperature above  $612^\circ\text{C}$  the oxidation rate increases right up to  $900^\circ\text{C}$  and then it once again begins to drop. This reduction in the oxidation rate is observed in the temperature range  $900$ - $950^\circ\text{C}$ . The slight increase in the oxidation rate of niobium upon an increase in temperature above  $950^\circ\text{C}$  is once again followed by a significant reduction in it (from  $1.24 \times 10^{-6}$  to  $7.54 \times 10^{-6}$  grams/sq cm x second) in the temperature range from  $1000$  to  $1100^\circ\text{C}$ .

Thus, in the temperature range  $600$ - $1200^\circ\text{C}$  there are three intervals in which an anomalous temperature relation of the oxidation rate of niobium

is observed. As a result of these anomalies in the temperature relation of the oxidation rate the curve on Figure 9 at temperatures above 600°C is jagged with three clearly expressed peaks.

As was pointed out above, there is always a continuous sublayer of dark oxide on the boundary with the metal throughout the entire range of oxidation temperatures. Polished specimens oxidized at various temperatures for a time sufficient to establish the linear law of oxidation were used for metallographic investigation of this sublayer. As a result of the sublayer being thin its microscopic investigation was done on oblique cross sections of specimens and the angle between the surface of the specimen and the plane of the cross section did not exceed 10°. For convenience of preparing the slides the specimens were poured with wedges in glass plastics.

On the basis of these microphotographs of the oblique cross sections a semi-quantitative evaluation of the average thickness of the sublayer for the temperature range 400-700°C was made. Analysis of preliminary data showed that with an increase in oxidation temperature the thickness of the dark sublayer of oxide is increased. In the temperature range 600-612° there is a sharp increase in the thickness of the sublayer. At 600°C the thickness of the sublayer is about 12 microns and at 612°C it reaches 23 microns. Thus, in this temperature range there is a significant increase in the thickness of the dark sublayer and a reduction in the oxidation rate.

Figure 10 shows the relation of the oxidation rate of niobium to the pressure of oxygen at temperatures of 400, 625, and 1000°C. For each of these temperatures kinetic curves of oxidation at oxygen pressures of 20, 150, 420, and 760 mm of mercury were drawn. As seen on the graph, as the oxygen pressure increases at all of the investigated temperatures the oxidation rate of niobium is increased. However, this is true only for the stage of oxidation that is characterized by the linear law. When a protective dark oxide film is formed on the specimens (400°C) whose growth is subject to the parabolic law an increase in the oxygen pressure in these limits has no effect on the oxidation rate of the metal (see Figure 10a). However, the time to the transition from the parabolic law to the linear law is noticeably reduced.

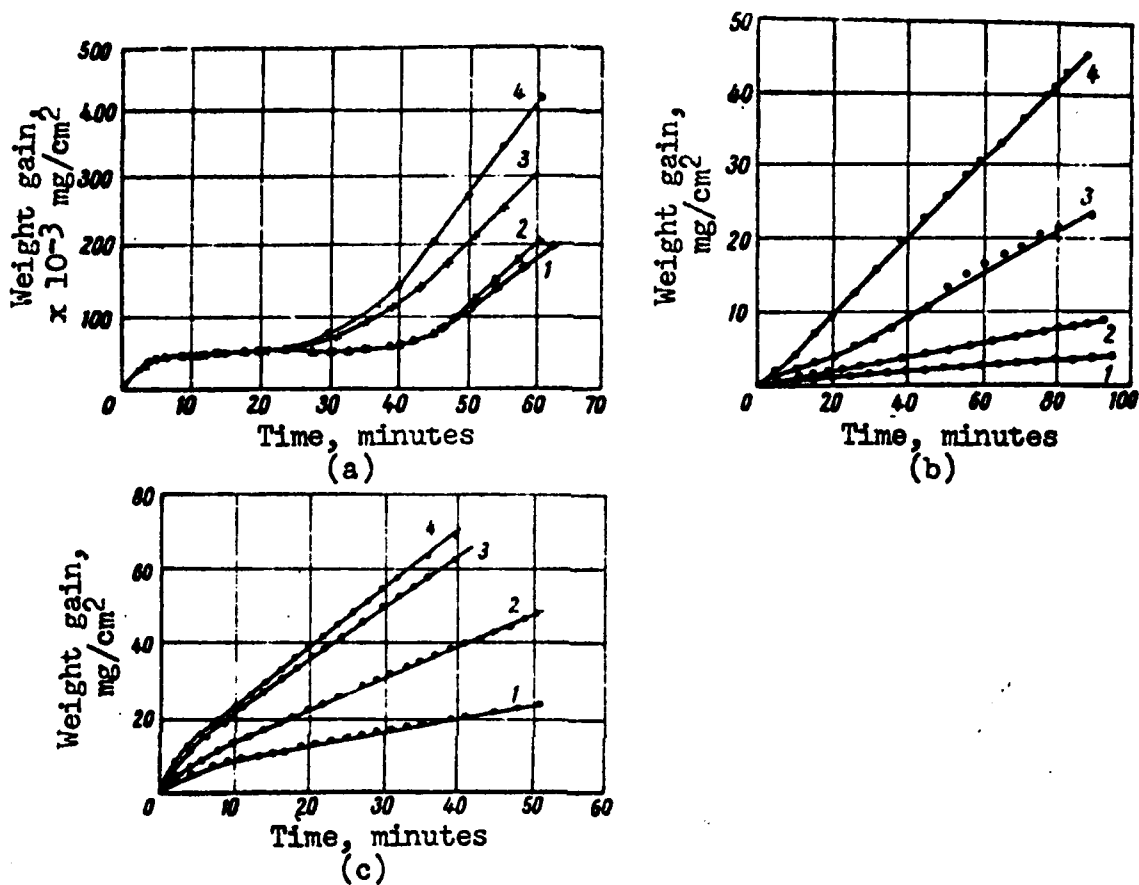


Figure 10. Relation of the Oxidation Rate of Niobium to Oxygen Pressure: a--400°C; b--625°C; c--1000°C; 1--20 mm of mercury; 2--150 mm of mercury; 3--420 mm of mercury; 4--760 mm of mercury.

### Discussion of Results

We note first that iodide refining of technical niobium and subsequent remelting in an electron-beam furnace made it possible to obtain metal of high purity. Up to now there had been no data on the kinetics of oxidation of this type of niobium in literature. Also, they are of definite interest since they can help solve the contradictions arising in comparisons of results of the work of various researchers who used metal of different purity.

Comparing the results of this work with data obtained by us earlier it can be concluded that generally the linear rate of oxidation of a purer niobium is considerably higher than of the initial technical metal with the

exception of the temperatures 700 and 800°C at which approximately the same oxidation rates were observed. Consequently, niobium can be classed as a metal in which additions increase scale resistance in contrast, for example, to zirconium in which additions lower its corrosion resistance [8, 9].

Published data on the kinetics of niobium oxidation contain contradictions which are evidence to some extent of the complexity of this process. In addition to them, a number of important moments that agree in the research of various authors can be noted. Thus, in the oxidation of niobium in the temperature range 350-450°C in our and in other research [2, 3, 10, 11] two periods of oxidation were observed: the first is characterized by the parabolic law of oxidation and the second by the linear law. The transition from the parabolic law of oxidation to the linear law occurs simultaneously with the transformation of the dark film into a white porous oxide.

The data obtained in our work also confirm the anomalous effect of a reduction in the oxidation rate with an increase in temperature above 600°C which was noted in works [2, 3, 10]. According to our data, this phenomenon is observed at temperatures of 600-612°C. That is, it is observed in a smaller range than indicated in other works [2, 3]. A similar effect was noted by us earlier in an investigation of technical niobium in the temperature range 800-900°C. This effect showed up in purer niobium at higher temperatures (900-950°C). Also, this work revealed a third temperature range of 1000-1100°C where there is also observed a considerable reduction in the oxidation rate with an increase in temperature. The kinetics of niobium oxidation in this temperature range has been studied little. Therefore, it is still not clear to what extent the additions in niobium affect this anomaly.

Thus, comparison of the more important facts of the kinetics of niobium oxidation shows that the results published in the various works are not contradictory to the extent that might have been thought earlier. Actually, this work established all the anomalies noted earlier in the temperature relation of linear oxidation rate of niobium. Depending upon the purity of the metal the extent to which these anomalies appear varies and the temperature intervals can be changed. However, the character of the relation of the linear rate of oxidation to temperature is retained.

In works [11, 12] no anomalies in the temperature relation of the oxidation rate of niobium were observed. It is true that sometimes this was because the temperature ranges of isothermic oxidation which the author selected were too broad and the kinetics of oxidation were not studied at the extreme temperatures.

The data in this work on the effect of oxygen pressure on the oxidation process agree well with the results of other works [5, 13].

Now, describing the possible mechanism of niobium oxidation, we first note that the retention of surface defects and special inert indicators (gold and others) after oxidation of the metal indicates mainly diffusion of oxygen through the oxide film through the metal. The possibility of such a mechanism is attributed to the nature of the niobium pentoxide which is an n-type semiconductor with insufficient anions [14].

The oxidation rate in the first stage characterized by the parabolic law is determined by the growth in the protective oxide film. The most probable oxidation mechanism at this stage is diffusion of the oxygen ions through the oxide film and subsequent dissolution of it in the metal. At a certain oxygen concentration in the metal one of the phase oxides ( $\text{NbO}$ ,  $\text{NbO}_2$ , and  $\text{Nb}_2\text{O}_5$ ) or a mixture of them is formed.

Depending upon temperature the composition and the protective properties of the oxide film during niobium oxidation can change considerably. After a certain (critical) thickness of the oxide film is reached it begins to break down due to internal stresses caused by the great difference in the amounts of metal and oxide.

The process of breakdown of the oxide film is characterized on the kinetic curves by the transitional segment. The established oxidation process, as noted above, is described by the linear law. This process occurs when there is simultaneously a dark oxide sublayer firmly bonded to the metal and a white porous oxide which exfoliates easily from the specimen. In the oxidation process the amount of porous scale is increased with the passage of time; but the thickness of the dark sublayer is obtained approximately constant. This can be presented as follows. At the point where the continuous oxide film breaks down the metal is exposed directly to the oxygen. As a result of the interaction of oxygen with the metal a new segment of new oxide film is formed which grows until it reaches a certain critical thickness and then once again breaks down. This process proceeds along the entire surface of the specimen and as a result a certain average rate of oxidation is established. Naturally, it is possible in this case to measure only the average thickness of the dark oxide sublayer. Thus, in our opinion, the dark oxide sublayer observed on the specimen in all cases of oxidation basically determines the linear oxidation rate of niobium in the established process.

As the research showed, as the temperature increases the average thickness of the dark oxide sublayer increases sharply in the temperature range 600-612°C. The observed anomaly in the temperature relation of the linear rate of oxidation of niobium in this temperature range apparently is caused by this phenomenon.

The question of anomalies in the temperature relation of the oxidation rate is thus reduced to an explanation of the circumstances causing the nonuniform growth in the thickness of the oxide sublayer in the temperature range. This can be that case when an increase in the mobility

of oxygen in the oxide layer and in the metal is excessively compensated by an increase in the thickness of the oxide sublayer which is a barrier preventing the oxygen from reaching the metal.

### Conclusions

The kinetics of oxidation of iodide niobium remelted in an electron beam in oxygen at 350-1200°C was studied by the method of continuous weighing. As a result it was established:

1. In the temperature range 350-400°C the oxidation process in the initial period it is described by a parabolic law and then there is a transitional stage which is characterized by an increase in the oxidation rate.
2. The established process of niobium oxidation in all of the temperature ranges that were studied corresponds to the linear law.
3. In the temperature relation of the constants of the rate of the linear law of oxidation there are three temperature ranges (600-612°C, 900-950°C, and 1000-1100°C) in which the oxidation rate is reduced with an increase in temperature.
4. The anomaly in the temperature relation of the constant of the oxidation rate of niobium in the temperature range 600-612°C is associated with the sharp increase in the thickness of the dark oxide sublayer.
5. The oxidation rate of niobium according to the linear law increases with an increase in oxygen pressure while the oxygen pressure has no noticeable effect on the rate of the process described by the parabolic law.

### BIBLIOGRAPHY

1. B. N. Revyakin, I. I. Korobkov, A. I. Yevstyukhin, and V. S. Lyashenko, V sb.: Metallurgiya i metallovedeniye chistykh metallov (In the collection: Metallurgy and Metal Science of Pure Metals), Nr III, Moscow, Gosatomi, dat, 1961, page 175.
2. B. Argent and B. Phelps, Journal of the Institute of Metals, Vol 82, 1959, page 301.
3. D. Aylmore, S. Gregg, and W. Iepson, Journal of the Electrochemical Society, 1960, page 107.

4. V. I. Arkharov, A. F. Gerasimova, and T. V. Ushakova, Fizika metallov i metallovedeniye (Physics of Metals and Metal Science), Vol 12, Nr 5, 1961, page 761.
5. P. Kofstad and H. Kjolldal, Transactions of the Metallurgical Society, 1961, page 221.
6. Klopp, Sims, and Jaffee, V sb.: Problemy sovremennoy metallurgii (In the collection: Problems of Modern Metallurgy), Nr 3, Moscow, Publishing House of Foreign Literature, 1960, page 51.
7. V. S. Yemel'yanov, G. A. Leont'yev, and A. I. Yevstyukhin, "Study of the Iodide Refining of Niobium", V sb.: Metallurgiya i metallovedeniye chistykh metallov (In the collection: Metallurgy and Metal Science of Pure Metals), Nr II, Moscow, Atomizdat, 1960, page 93.
8. Metallurgiya tsirkoniya (Metallurgy of Zirconium), Moscow, Publishing House of Foreign Literature, 1959.
9. I. I. Korobkov and A. I. Yevstyukhin, V sb.: Metallurgiya i metallovedeniye chistykh metallov (In the collection: Metallurgy and Metal Science of Pure Metals), Nr II, Moscow, Atomizdat, 1960, page 93.
10. D. Bridges and W. Fassel, Journal of the Electrochemical Society, 1956, page 103.
11. Gul'bransen and Endryu, V sb.: Niobiy i tantal (In the collection: Niobium and Tantalum), Moscow, Publishing House of Foreign Literature, 1960.
12. H. Jnougé, Special Report series No. 5, Metallurgical Society ADME, 1956.
13. T. Hurlen, Journal of the Institute of Metals, Nr 8, 1961, page 89.
14. K. Hauffe, Oxidation von Mettallen und Metallegirungen, Springer-Berlin, 1956.

6306

CSO: 1879-D

REACTION OF AUSTENITE CHROMIUM-NICKEL STEEL  
WITH LIQUID LITHIUM

N. M. Beskorovaynyy,  
M. T. Zuyev,  
V. S. Yeremeyev

Austenite chromium-nickel steel possesses higher heat resistance, better technical properties -- deformability and weldability, higher plasticity and indicates good corrosion stability in sodium coolant up to 700-800° C as compared with ferrite steel.

Attempts to use austenite chromium-nickel steels for lithium coolant gave negative results: chromium-nickel stainless steel as well as chromium stainless steel with 2% nickel are not resistant to corrosion in lithium [1].

These steels were tested at 800° C for 230 hours in reaction vessels made of technical iron, containing about 0.04% of carbon. Interaction of lithium with chromium-nickel steels was intercrystalline in nature and the depth of corrosion reached 2.78 mm/year. Mechanical properties were also changing: specific elongation decreased from 45-50 to 4-6%; the yield strength decreased from 69 to 61 kg/mm<sup>2</sup> (tests were conducted on flat specimens 0.7 mm in thickness). It was established that content of nickel, chromium, silicon and tungsten in these alloys also decreased, i.e., in liquid lithium leaching of these components of chromium-nickel steel occurred. The rate of corrosion calculated from the weight loss for different steels comprised from 0.06 to 0.034 g/mm<sup>2</sup>·hr. Due to transfer of carbon from reaction vessels the content of carbon in the investigated steels in all cases increased to 0.6-0.7%.

The rapid drop of plastic properties after holding in lithium was also observed in steel with 17% Cr, 2% Mo and 1% Nb in the presence of 2.0-2.5% Ni [1]. The depth of corrosion was reaching 5.6 mm/year. Chromium stainless steels were found to be more stable in lithium if they

were additionally alloyed with molybdenum, tungsten and niobium. However, the results of other works do not show strong corrosion destruction of austenite chromium-nickel steels in lithium.

At 800-1000° C pure chromium and particularly nickel dissolve in lithium to a significant extent, which one would think is the cause for rapid destruction of 1Kh18N9T steel (Table 1).

Table 1

Solubility of Iron, Chromium, Nickel and Titanium in Lithium

Testing temperature, °C	Content of elements in lithium, weight %			
	Fe	Cr	Ni	Ti
700	—	—	0,15	—
750	—	—	0,5	—
800	—	0,012	—	—
850	—	—	1,36	—
900	0,01	—	—	0,014
950	—	0,8	3,2	—
1000	0,02	—	—	—
1200	0,35	3,96	—	—

However, upon testing 1Kh18N9T steel it was found that transfer of chromium and nickel atoms into liquid lithium is drastically lowered (Table 2).

Table 2

Solubility of Components of 1Kh18N9T Steel in Lithium at 975° C [3]

Li	Testing time, hours	Content of elements in lithium, weight %		
		Fe	Cr	Ni
Distilled	110	0,0019	10 <sup>-4</sup>	10 <sup>-4</sup>
	240	0,001	0,0012	0,029
C 1,0% N <sub>2</sub>	110	0,0008	0,48	0,020
C 0,99% O <sub>2</sub>	110	0,0019	10 <sup>-4</sup>	0,031
C 1,12% O <sub>2</sub>	240	0,0012	0,0026	0,109

It follows from Table 2 that in distilled lithium after testing 1Kh18N9T steel one finds 100 times less chromium and nickel than after testing pure metals. Nitrogen impurity in lithium increases leaching out of chromium from 1Kh18N9T steel. Oxygen in lithium increases leaching out of nickel.

Mechanical properties of 1Kh18N9T steel after testing in lithium also changed very little. The reaction vessels and specimens were made of the same metal (Table 3).

Table 3

Mechanical Properties of 1Kh18N9T Steel After Testing  
Rods 3 mm in Diameter in Lithium [3]

Li	Testing temperature, °C	Time of testing, hours	$\sigma_b$ , kg/mm <sup>2</sup>	$\delta$ , %	$\psi$ , %
Distilled	975	110	60	63	52
	975	240	60,5	58,2	48,1
	1150	81	59,1	59,6	51,9
C 1,1% O <sub>2</sub>	975	240	62	52,1	46,9
C 0,41% O <sub>2</sub>	1150	81	62,6	56,8	49,0
C 1,7% N <sub>2</sub>	975	120	63,5	52,6	43,3
C 0,45% N <sub>2</sub>	1150	81	65,8	54,2	38

The above data indicate that high strength and plasticity of 1Kh18N9T steel is preserved after tests in distilled lithium. Even lithium contaminated with large quantities of nitrogen and oxygen had little effect on the plastic properties of this type of steel, while in one of the works [1] its plasticity dropped catastrophically.

In the distilled lithium the corrosion boundary layer is almost completely absent and only after testing in lithium which contained significant quantities of nitrogen and oxygen surface destruction and

intercrystalline corrosion was observed. However, the degree of corrosion destruction of the structure of 1Kh18N9T steel during contamination of lithium with oxygen and nitrogen is not so great as to change significantly the plastic properties under the indicated test conditions.

During analysis of the data in Table 3 one should remember that in the work of Yu. F. Bychkova et al [3] mechanical properties were determined on rods 3 mm in diameter and in the work of V. S. Lyashenko et al [1] on bars 0.7 mm in thickness and 3 mm wide. If one takes, for example, that the thickness of the corrosion layer, the properties of which are significantly poorer, is equal to approximately 0.1 mm, then for circular cross section specimens the area of corrosion layer comprises 13% of the total cross sectional area while for bar specimens it comprises 30%.

The results of testing of bars made of 1Kh18N9T steel 1 mm thick and 3 mm wide in reaction vessels made of the same material, in pure lithium are given in Table 4.

Table 4

Mechanical Properties of 1Kh18N9T Steel After  
Testing in Argon Atmosphere in Liquid  
Helium (bars 1 x 3 x 14 mm)

Testing temperature, °C	Time of testing, hours	$\sigma_b$ , kg/mm <sup>2</sup>		$\delta$ , %		No. of backward and forward bends (technical test)	
		Ar	Li	Ar	Li	Ar	Li
1000	100	59.7	58.0	57.6	54.3	28	29
1200	100	52.4	50.2	54.3	54.0	34	21

Note: Originally  $\sigma_b = 65.7$  kg/mm<sup>2</sup>;  $\delta = 48.4\%$ .

The above results show that in the case of bars the strength of 1Kh18N9T steel after testing in lithium at high temperatures remain sufficiently high and change very little as compared with tests in argon medium. At the indicated temperatures the grain size increases significantly, but the corrosion surface layer with changed structure and also intercrystalline corrosion are found. Only after testing in lithium at 1200° C the surface layer shows point inclusions and increased microhardness: microhardness on the surface is equal to 244-285 kg/mm<sup>2</sup> while in the interior of the specimen it is equal to 119-185 kg/mm<sup>2</sup> (Fig. 1).



Figure 1. Microstructure of 1Kh18N9T steel. Tests were conducted in lithium at 1200° C for 100 hours. The grain size is large with indications of  $\alpha$  phase and the surface shows point inclusions (200 x).

At 800-1000° C the solubility of chromium-nickel steel remains practically the same and only at 1200° C it significantly increases (Table 5).

The welding seams on 1Kh18N9T steel also behave sufficiently well in lithium (Table 6).

Table 5

Rate of Corrosion of Chromium-Nickel Steel  
in Lithium, Calculated from the  
Weight Loss of Specimens

Temperature, °C	Rate of corrosion, g/m <sup>2</sup> ·hr
800	0.06-0.034 [1]
1000	0.034*
1200	0.388*
* 1Kh18N9T steel.	

Table 6

Mechanical Properties of Welding Seams of 1Kh18N9T Steel  
After Testing in Argon Atmosphere and in Liquid Lithium  
(specimens are bars and argon arc welding was used)

Temperature, °C	Time of testing, hours	$\sigma_b$ , kg/mm <sup>2</sup>		$\delta$ , %		No. of backward and forward bends (technical test)	
		Ar	Li	Ar	Li	Ar	Li
Initial state		59.9		27.2		23	
1000	100	52.0	50.7	41.2	37.1	17	23
1200	100	49.7	50.2	59.0	53.4	29	23

Note: Destruction in all cases occurred not along the welding seam, but along the transition zone.

The welding seam had flowing structure in many cases contaminated with foreign inclusions which are located along the grain boundaries as well as in the grains themselves. After annealing in argon at 1000° C the flowing structure of the welding seam changed little. At 1200° C a significant growth of grains occurred. The structure of welding seam and the transition zone after testing in lithium would not show difference in comparison with annealing in argon.

The unsatisfactory corrosion stability of chromium-nickel steels in lithium found in the work of V. S. Lyashenko et al [1] is apparently associated with the fact that tests were conducted in reaction vessels made of technical iron, containing about 0.04% carbon, as a result of which chromium-nickel steel was saturated with carbon to the extent of 0.6-0.7% and resulted in the formation of carbides in the structure.

It was established in [4] that change of structure in technical iron and carbon steel after testing in lithium is associated with diffusion of lithium. Lithium destroys iron carbides as a result of which inter-crystalline corrosion is developed. The higher the content of carbon in the iron and in carbon steel is the higher the concentration of lithium in surface layers is.

The same phenomenon is observed in chromium-nickel steel [1]. Thus in 4Kh14N14B2M steel (0.4% carbon) the mean content of lithium comprised  $7 \cdot 10^{-2}\%$  and in 1Kh18N9T steel (0.1% carbon) --  $2 \cdot 10^{-3}\%$ .

Thus a transfer of carbon from iron reaction vessels into chromium-nickel steel may create favorable conditions for diffusion of lithium. Lithium destroys chromium carbides causes development of intercrystalline corrosion (Fig. 2).

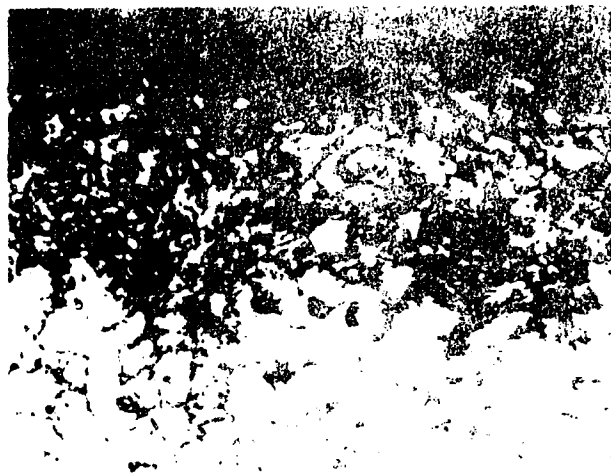


Figure 2. Development of intercrystalline corrosion on the surface of 1Kh18N9T steel after testing in lithium at 1000° C for 100 hours in iron vessel (200 x).

Investigations show that diffusion of lithium in 1Kh18N9T steel during testing in reaction vessels made of technical iron proceeds quite intensely: in 100 hours at 1000° C the concentration of lithium in the surface layer reaches 0.16% and the depth of its penetration comprises about 0.2 mm. In 500 hours the concentration of lithium increases to 0.72% and its penetration to 0.3 mm (Fig. 3).

In addition during testing of chromium-nickel steel in reaction vessels made of technical iron due to the difference in metals leaching of chromium and nickel from steel is increased. Thus, after testing technical iron in lithium in reaction vessels made of 1Kh18N9T steel at 1000° C one observes transfer of chromium and nickel from stainless steel into the iron, which is indicated by the increase of microhardness of the surface layer in the course of 100 hours of testing from 109 to 800 kg/mm<sup>2</sup>.

The weak corrosion effect of lithium on the structure and strength characteristics of 1Kh18N9T steel obtained in the work of Yu. F. Bychkova et al [3] at 975-1150° C and duration from 30-240 hours and also the results of this work at 1000-1200° C and duration of 100 hours indicate the possibility of using chromium-nickel steel for work in lithium media. Apparently in the case of identical materials and in the absence of

transfer of carbon the stability of austenitic chromium-nickel steel in lithium must be significantly higher. The weak corrosion of 1Kh18N9T steel in lithium, found in this work, may be explained as follows.

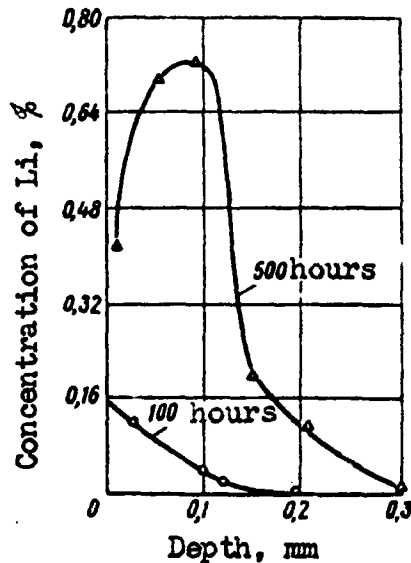


Figure 3. Concentration curves of the distribution of lithium in the surface layer of 1Kh18N9T steel after testing in lithium at 1000° C in iron vessels.

In the absence of transport of carbon the prolonged testing of 1Kh18N9T steel at 1000 and 1200° C in lithium aids transfer of carbides, existing in the steel along the grain boundaries, and also of other impurities into solid solution. In this case the grain growth is made easier, but apparently the diffusion of lithium along the "clean" grain boundaries is hindered, and intercrystalline corrosion is not developed. Certain leaching out of chromium and of nickel and also of lithium into the surface layer may, to a certain extent, change its composition and aid the formation of ferrite structure. However, the change of composition of only a thin surface layer in the absence of intercrystalline corrosion is insufficient to change significantly the strength characteristics of 1Kh18N9T steel.

#### Conclusions

1. After testing 1Kh18N9T steel in lithium contained in vessels made of the same steel at 1000 and 1200° C no significant changes of mechanical properties of steel are observed in comparison with identical treatment in

argon medium. In accordance with these indications 1Kh18N9T steel possesses sufficient corrosion resistance in lithium at 1000 and 1200° C for a period of 100 hours.

2. No significant corrosion effects of lithium on welding seams of 1Kh18N9T steel were found.

3. The rate of corrosion of 1Kh18N9T steel is calculated from weight losses of specimens (apparently associated with leaching out of chromium and nickel) at 1000° C comprises 0.034 g/m<sup>2</sup>·hr and at 1200° C -- 0.388 g/m<sup>2</sup>·hr.

4. During testing of 1Kh18N9T steel in reaction vessels made of technical iron lithium diffuses into the surface layer of steel to a significant depth, which may aid the development of intercrystalline corrosion.

#### BIBLIOGRAPHY

1. V. S. Lyashenko et al, Trudy Vtoroy mezhdunarodnoy konferentsii po mirnomu ispol'zovaniyu atomnoy energii (Works of the 2nd International Conference on Peaceful Uses of Atomic Energy), Geneva, 1958, Reports of Soviet Scientists, Vol. 3, Nuclear Fuels and Reactor Metals, Moscow, Atomic Publishing House, 1959, page 642.

2. N. M. Beskorovaynyy, Ye. I. Yakovlev, Collection Metallurgiya i metallovedeniye chistykh metallov (Metallurgy and Metallography of Pure Metals), No. 2, Moscow, Atomic Publishing House, 1960, page 189.

3. Yu. F. Bychkov et al, Metallurgiya i metallovedeniye chistykh metallov, No. 2, Moscow, Atomic Publishing House, 1960, page 78.

4. N. M. Beskorovaynyy, V. S. Yeremeyev and Yu. Ya. Tomashpol'skiy, Metallurgiya i metallovedeniye chistykh metallov, No. 3, Moscow, State Atomic Publishing House, 1962, page 233.

6101

CSO: 1879-D

## CORROSION RESISTANCE OF IRON IN LITHIUM

N. M. Beskorovaynyy  
V. S. Yerameyev  
M. T. Zuyev  
V. K. Ivanov  
Yu. Ya. Tomashpol'skiy

Study of corrosion resistance properties of iron in lithium presents significant interest since iron is the principal component of stainless chromium and chromium-nickel steels. These alloys may be used as structural materials when lithium is used as a coolant.

Iron dissolves little in lithium. Thus, at 1000° C solubility does not exceed 0.03-0.04% [1]. When lithium is contaminated with oxygen and nitrogen to the extent of 1-2% the solubility of iron in lithium increases by about 15% [2]. The mechanical properties of iron change insignificantly (Table 1).

Table 1

Effect of Oxygen and Nitrogen Content in Lithium  
on Mechanical Properties of Technical Iron at  
800° C and When Duration of Test Was  
152 hrs [2]

Li	$\sigma_b$ , kg/mm	$\delta$ , %
Distilled	30.3	27.2
1% O <sub>2</sub> . . . . .	29.1	23.6
1% N <sub>2</sub> . . . . .	27.2	23.1

Lithium has significant diffusion mobility in industrial iron. During tests in liquid lithium surface layers of industrial iron change both the structure and properties [3].

In this work corrosion tests were conducted on industrial iron and on iron remelted in  $10^{-1}$  -  $10^{-2}$  mm Hg vacuum (Table 2). A significant effect of carbon was found on diffusion of lithium [3].

Table 2

Chemical Composition of Investigated Iron (in %)

Fe	C	Mn	Si	S	P	O <sub>2</sub>
Industrial . . . .	0.047	0.17	0.17	0.041	0.007	0.017
Vacuum fused . . .	0.009	0.08	0.09	0.046	0.008	0.007-0.010

Reaction vessels with specimens were filled with lithium in argon atmosphere. To insure minimum contamination of lithium with gas impurities (oxygen and nitrogen), argon was purified by scrubbing through fused lithium files. Periodically tests were conducted in lithium contaminated with oxygen and nitrogen (saturated in air).

During testing in lithium the surface layer of iron dissolves. Dissolution occurs predominantly along the grain boundaries and it increases with increase of temperature and with duration of tests. The purity of iron also has significant effect on its solubility. For example, the destruction of surface and grain boundaries of vacuum fused iron at 600° C in 500 hours is less than destruction of industrial grade iron in 50 hours (Fig. 1, 2). At 1000° C boundaries of  $\gamma$ -iron are dissolved. In the course of cooling when  $\gamma$ -phase new thin boundaries are formed without traces of corrosion (Fig. 3).

The polished surfaces of specimens become rough due to dissolution. This roughness is well fixed by profiling the surface (Fig. 4). The properties of the surface layer of industrial iron are also changing: the hardness and strength are lowered and plasticity increases (Table 3 and Fig. 5). The parameter of crystal lattice is also lowered from 2.8620-2.8630 to 2.8605-2.8607 kX, which corresponds to lattice parameter of pure iron [4]. [Note: 1 kX = 1.00202 Å]. The impurities of carbon and nitrogen change most significantly the lattice parameters of  $\alpha$ -iron (Table 4).



Fig. 1. Surface of vacuum fused iron after testing in lithium at 600° C for 500 hours (270 x).

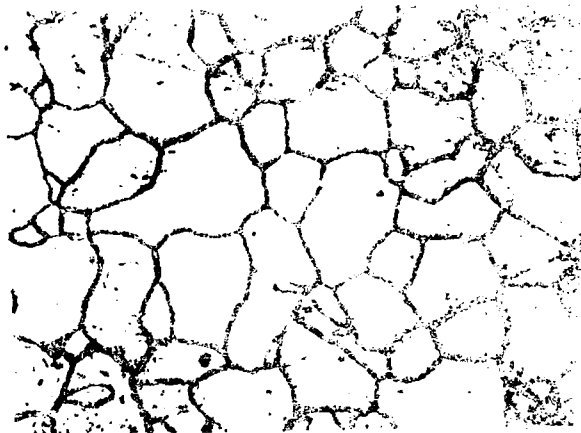


Fig. 2. Surface of industrial iron after testing in lithium at 600° C for 50 hours (270 x).



Fig. 3. Surface of industrial iron after testing in lithium at 1000° C for 50 hours. In addition to destruction along the austenite grain boundary thin boundaries are seen without corrosion marks. (270 x).

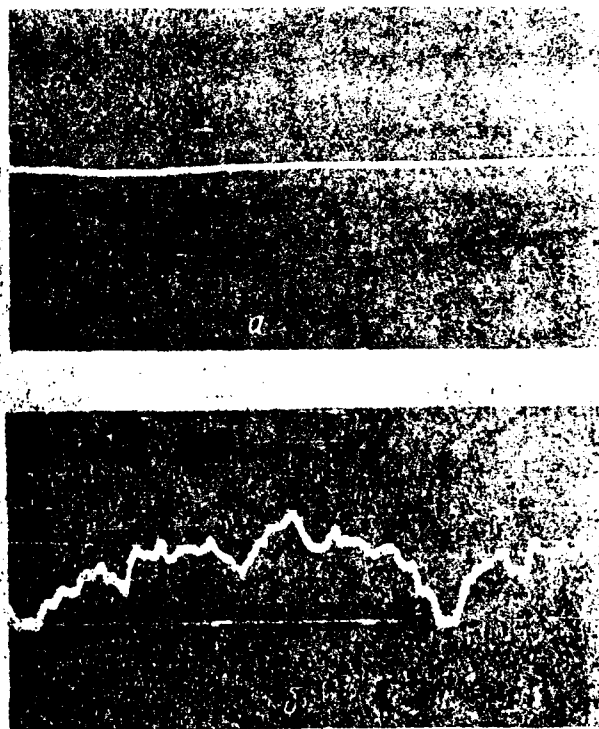


Fig. 4. Profile graph of the surface of industrial iron. a - initial state; b - after testing in lithium at 1000° C for 50 hrs. Vertical magnification is x 2500 x 6.5 and horizontal magnification x 20 x 6.5.

Table 3

Mechanical Properties of Industrial Iron After Testing for 100 hours in Argon and in Liquid Lithium

Temperature of testing, °C	$\sigma_b$ , kg/mm <sup>2</sup>		$\delta$ , %	
	Ar	Li	Ar	Li
1000	26,3	24,3	25,6	25,7
1200	28,2	23,1	18,0	26,0

Table 4

Effect of Impurities on Crystal Lattice Parameter of  $\alpha$ -iron (the lattice parameter of pure iron is 2.8605-2.8607 kX) [4]

C		Mn		Si		N <sub>2</sub>		O <sub>2</sub>	
Content, atom %	Parameter kX								
0,004	2,8605	0,47	2,8608	2,5	2,8591	0,004	2,8605	0,03	2,8599
0,011	2,8609	—	—	—	—	0,015	2,8610	—	—
0,015	2,8612	—	—	—	—	0,10	2,8627	—	—

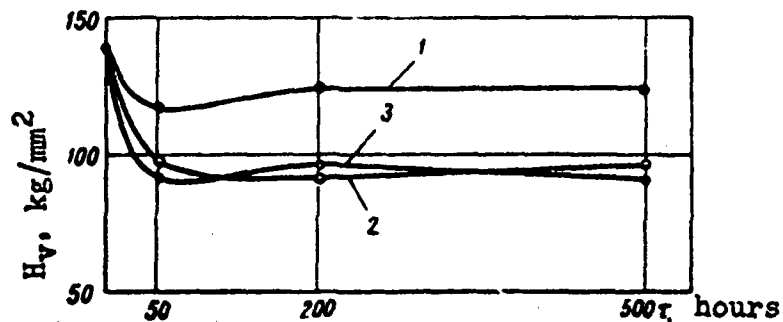


Figure 5. Change of microhardness of the surface of specimens of industrial iron after testing it in lithium at 600° C (1), 700° C (2) and 1000° C (3).

These changes take place due to decrease of the impurity content in the surface layer of industrial iron, since all impurities (C, Mn, Si, P, O<sub>2</sub>, N<sub>2</sub>), with the exception of sulfur increase the strength and hardness of iron. Sulfur is the only impurity which does not affect the strength characteristics of iron when its content is as high as 0.175% [5].

During testing of vacuum fused iron in lithium despite the overall decrease of impurity content, the decrease in hardness also occurs (Fig. 6), which verifies the existence of refining process in vacuum fused iron. However, after testing of vacuum fused iron in lithium the surface layer was enriched in sulfur [1]. Sulfur diffuses from deeper lying layers. In this case the concentration of sulfur at the surface increases while in deeper lying layers it decreases (Fig. 7). It follows from Fig. 6 that microhardness does not reflect this process.

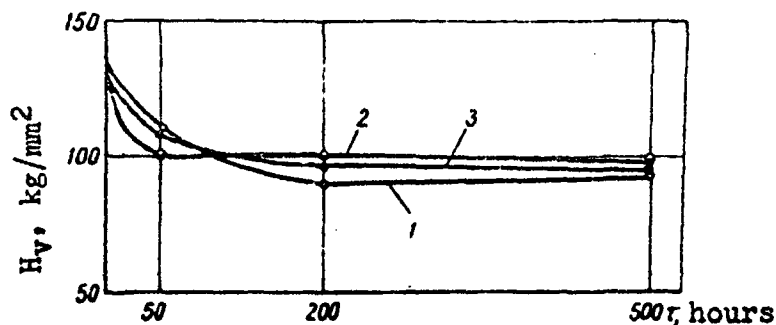


Figure 6. Change of microhardness of the surface of specimens of vacuum fused iron after testing in lithium at 600° C (1), 700° C (2) and 1000° C (3).

Oxygen and nitrogen impurity in lithium does not affect the surface properties of the surface layer of vacuum fused iron (Table 5).

Table 5

Effect of Contamination of Lithium with Oxygen and Nitrogen on the Properties of the Surface Layer of the Vacuum Fused Iron upon Testing for 50 Hours at 1000° C

Li	Microhardness of surface (kg/mm <sup>2</sup> )	Lattice parameter on the surface kX
"Pure" (reaction vessels were filled in argon atmosphere) . . . . .	99	2.8614
"Impure" (reaction vessels were filled in air) . .	94	2.8615

The first results on the study of the diffusion of lithium in industrial iron and carbon steels [3] have shown that the most significant changes in structure and properties of the surface layer, which characterize the corrosive effect of lithium, occur only there where lithium is present in bulk.

In this work the diffusion of lithium was investigated with cylindrical specimens 12-15 mm in diameter and 35 mm high. Layers, 0.02-0.03 mm thick, were removed from the side surfaces of these rods. Lithium, in the obtained shavings was determined according to N. M. Beskorovaynyy and others.

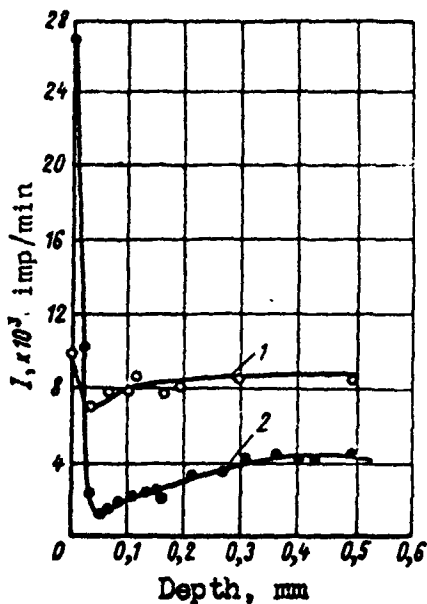


Fig. 7. Distribution of S35 in vacuum fused iron after testing lithium at 600° C (1) and 1000° C (2).

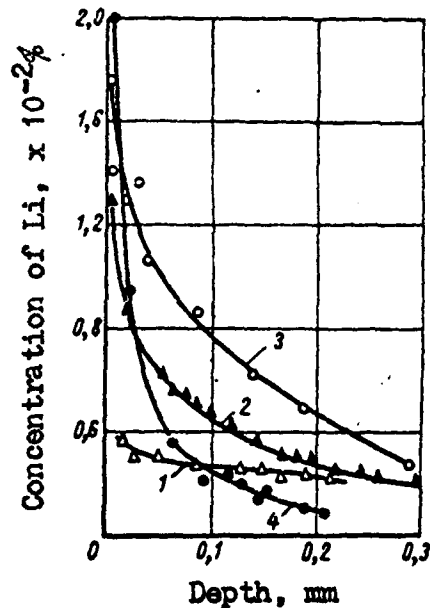


Fig. 8. Distribution of lithium in vacuum fused iron after testing for 100 hrs at 380 (1), 550 (2), 620 (3) and 670° C (4).

The distribution curves of lithium in vacuum fused iron the particle size of which was about 0.11-0.14 mm after testing at 380, 550, 620 and 670° C for 100 hours are given in Figure 8. It is apparent from the figure that lithium behaves uniquely. Its diffusion mobility in  $\alpha$ -iron does not increase, but decreases with increase of temperature.

These results show that diffusion of lithium in  $\alpha$ -iron is significantly effected by impurities such as carbon and others.

$\alpha$ -iron may dissolve at the most 0.04% of C at 723° C. At lower temperature solubility of carbon decreases and tertiary cementite is

liberated along the grain boundaries of ferrite (Fig. 9 b). Oxygen behaves analogously. Solubility of oxygen in  $\alpha$ -iron comprises about 0.11% at 715° C [6]. With lowering of temperature solubility of oxygen in iron falls as a result of which grain boundaries may be enriched with oxides. Sulfur impurity also distributes itself along the grain boundaries.



Figure 9. Microstructure of industrial iron after testing in lithium at 400° C for 25 hours (270 x).  
a - 0.2 mm depth where lithium is present; corrosion along grain boundaries; b - 0.3 mm deep without lithium; liberation of cementite along the grain boundaries is indicated with arrows.

Consequently, at lower test temperatures the grain boundaries of iron are enriched with impurities which have a significant chemical similarity to lithium. In addition, grain boundaries are more enriched with defects -- vacancies, clusters of vacancies, micropores, etc. Thus favorable conditions are established for diffusion of lithium along the

intergrain layer, which consists of boundary layers of grains enriched with impurities and defects. When lithium interacts with metals of intergranular layer corrosion products are formed and grain boundaries are thickened -- intercrystalline corrosion in iron on "purity" of boundaries is verified by distribution curves of lithium in industrial iron. The increased content of lithium in it as compared with vacuum fused iron causes much deeper penetration of lithium and much greater concentrations of the latter in the surface layer (Fig. 11, compared with Fig. 8).



Fig. 10. Microstructure of industrial iron at a depth of 0.19 mm. where lithium is present. Tests were conducted at 700° C for 200 hours. Intercrystalline corrosion can be observed along the grain boundaries. (270 x)

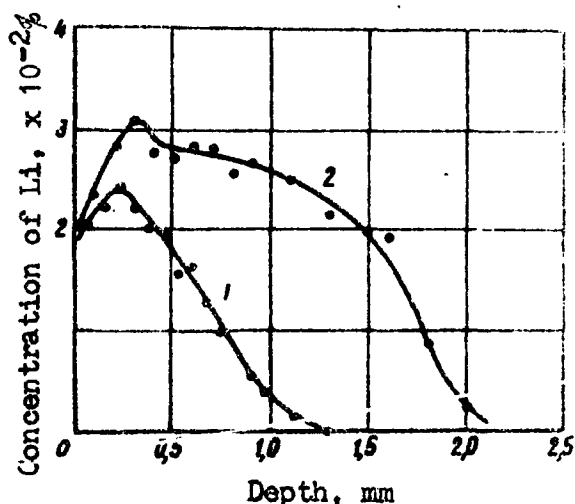


Fig. 11. Distribution of lithium in industrial iron after testing at 400° C (1) and 600° C (2) for 100 hours.

The effect of grain boundaries on the diffusion of lithium is also shown in Figures 12 and 13. The level of diffusion mobility in iron with finer grain size is significantly higher than in large grain iron.

The dependence of the diffusion of lithium on the amount of impurity along the grain boundary is also verified by tests at higher temperatures, 800-1000° C. At 800° C and to a greater extent at 1000° C (when  $\alpha \rightarrow \gamma$  transition occurs) the principal mass of impurities along the grain boundaries of iron transforms into solid solution and boundaries become "cleaner." Apparently, a decrease of the number of structural defects along grain boundaries occurs. As a result of this the diffusion mobility of lithium is sharply lowered. The penetration depth of lithium in vacuum fused iron at 800° C and 1000° C decrease approximately by a factor of 2-3 as compared with penetration depth at 620 and 670° C. Lithium distribution

curves at 800 and 1000° C practically coincide (Fig. 14). In the industrial iron at 800° C due to large impurity content a large diffusion mobility of lithium is still preserved, but it is already smaller than at 600° C. At 1000° C the diffusion penetration of lithium is lowered so much that it becomes equal in the depth to diffusion of lithium in vacuum fused iron at 550-670° C.

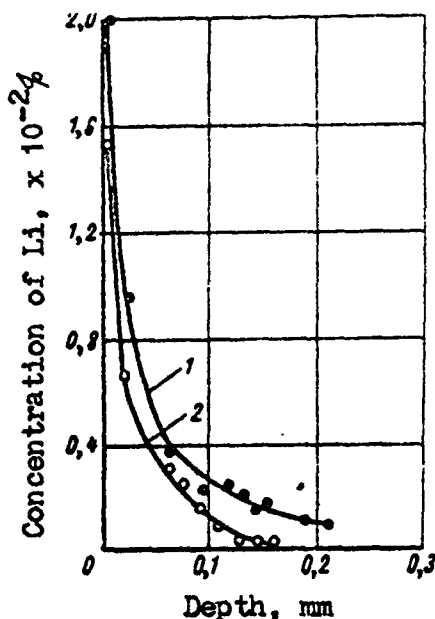


Fig. 12. Distribution of lithium in fine and large grain vacuum fused iron after testing at 670° C for 100 hours.  
1 - grain size 0.11 mm;  
2 - grain size 0.48 mm.

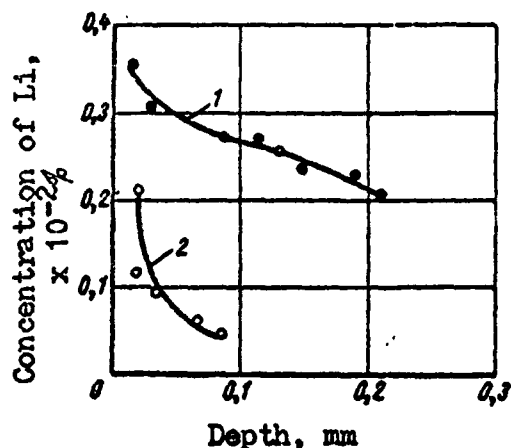


Fig. 13. Same as Fig. 12, but after testing at 380° C.  
1 - grain size 0.11 mm; 2 - grain size 0.48 mm.

Contamination of lithium with oxygen and nitrogen has little effect on the diffusion of lithium in industrial iron (Fig. 15). In vacuum fused iron the overall content of impurities is much lower than in industrial iron. Grain boundaries are also "pure." Despite this the surface layer, about 0.02-0.05 mm in thickness in vacuum fused iron, has about the same concentration of lithium as in industrial iron. In this layer the corrosion in vacuum fused iron developed not only along the grain boundaries, but also along the boundaries of the substructure -- fractionation of large grains into smaller ones occurs (Fig. 16).

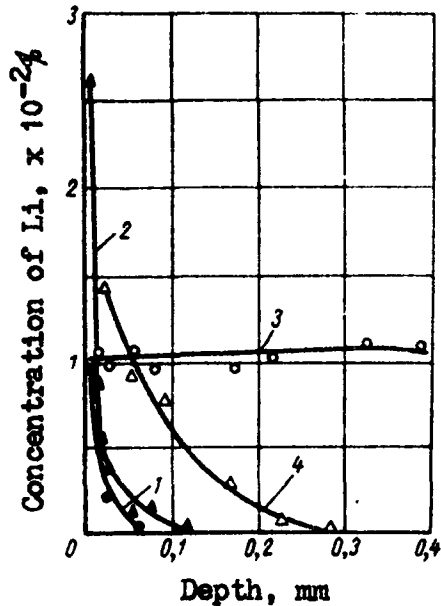


Fig. 14. Distribution of lithium in vacuum fused and in industrial iron after testing at 800 and 1000° C for 100 hours:  
 1 - vacuum fused iron, 800° C;  
 2 - same iron, 1000° C; 3 - industrial iron, 800° C; 4 - the same, 1000° C.

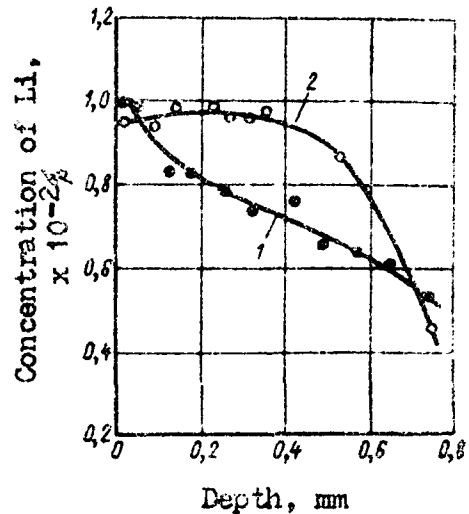


Fig. 15. Distribution of lithium in industrial iron after testing in "pure" (1) and in "contaminated" (2) lithium at 800° C for 25 hours.

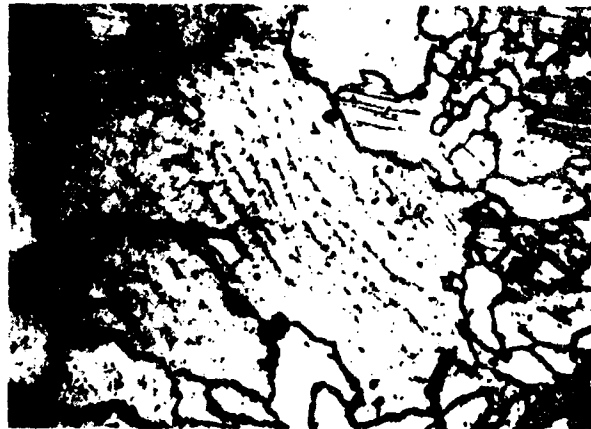


Fig. 16. Microstructure of vacuum fused iron at a depth of 0.05 mm after testing for 200 hours at 700° C. One may see corrosion destruction along the grain boundaries and in grains as well as fractionation of large grains into a large number of smaller grains (270 x).

Increase of concentration of lithium on the surface of vacuum fused iron and development of intercrystalline and intragranular corrosion in the surface layer may be caused by redistribution of sulfur from deeper layers to the surface (see Fig. 7) and by the formation of corrosion products which are sufficiently strongly retained on the surface layer.

Thus, it may be considered to have been established that diffusion of lithium in iron is determined by the content and distribution of carbon, oxygen, sulfur and other impurities in iron which have significant chemical affinity to lithium. The reaction of lithium with impurities causes intercrystalline corrosion and corrosion along the boundaries of substructure. It is possible that the presence of the indicated impurities in structural materials, including gases, has greater effect on the corrosion stability of structural materials in lithium than contamination of lithium with gases. This must be thoroughly investigated, but at least it is quite clear that improvement of the production of technology of structural materials for work in lithium media (vacuum fusion and others) must significantly increase the corrosion stability.

Since diffusion of lithium in iron proceeds by interaction with impurities, the diffusion coefficient calculated by normal methods gives only an approximate figure for the mobility of lithium in iron (Table 6).

Table 6

Diffusion Mobility of Lithium in Iron

Iron	Temperature of diffusion testing, °C	Order of magnitude of diffusion coefficient, cm <sup>2</sup> /sec
Vacuum fused	380	10 <sup>-8</sup>
	550	10 <sup>-10</sup>
	620	10 <sup>-10</sup>
	670	10 <sup>-10</sup>
	800	10 <sup>-11</sup>
	1000	10 <sup>-11</sup>
Industrial	400	10 <sup>-8</sup>
	600	10 <sup>-8</sup>
	1000	10 <sup>-9</sup>

### Conclusions

1. During testing of iron in lithium its surface becomes coarse and dissolution proceeds predominantly along the grain boundaries. Due to the refining effect of lithium the strength is lowered and plasticity of the surface layer of iron is increased.

2. Diffusion of lithium in iron proceeds along the grain boundaries and boundaries of substructure and is directly related to contamination of boundaries with impurities of carbon, sulfur, etc., to which lithium has a significant chemical affinity. The interaction of lithium with the indicated impurities causes intercrystalline corrosion.

3. In vacuum fused as well as industrial iron the diffusion mobility of lithium as a function of temperature is evaluated by quantities which are given in Table 6.

4. To improve the stability of structural materials in lithium it is necessary to direct particular attention to the technology of their production -- use of vacuum fusion and other methods which aid in obtaining pure metals and alloys with respect to gaseous and other impurities.

### BIBLIOGRAPHY

1. N. M. Beskorovaynyy and Ye. I. Yakovlev, "Investigation of Corrosion of Iron and Chromium Steels in Liquid Lithium," Metallurgiya i metallovedeniye chistykh metallov (Metallurgy and Metallography of Pure Metals), No. 2, Moscow, Atomic Publishing House, 1960, page 189.

2. Yu. F. Bychkov et al, "Corrosion Stability of Ya1-T Steel in Metal with Oxygen and Nitrogen Impurities," Metallurgiya i metallovedeniye chistykh metallov, No. 2, Moscow, Atomic Publishing House, 1960, page 78.

3. N. M. Beskorovaynyy, V. S. Yeremeyev and Yu. Ya. Tomashpol'skiy, "Diffusion Mobility of Lithium in Iron and Steels," Metallurgiya i metallovedeniye chistykh metallov, No. 3, Moscow, State Atomic Publishing House, 1962, page 233.

4. W. Pearson, A Handbook of Lattice Spacings and Structures of Metals and Alloys, 1958.

5. P. Obergoffer, Tekhnicheskoye zhelezo (Technical Iron), Moscow, Metallurgical Publishing House, 1933.

6. S. T. Rostovtsev, Teoriya metallurgicheskikh protsessov (Theory of Metallurgical Processes), Moscow, Metallurgical Publishing House, 1955.

7. P. L. Gruzin et al, Inzhenerno-fizicheskiy zhurnal (Journal of Engineering Physics), Vol. 1, No. 6, 1958, page 64.

## CORROSION RESISTANCE OF TITANIUM IN LITHIUM

N. M. Beskorovaynyy  
M. T. Zuyev

Titanium is an important structural material since it possesses valuable physical and mechanical properties: strength and good plastic properties ( $\sigma_b \approx 55 - 65 \text{ kg/mm}^2$ ;  $\delta \approx 25 - 30\%$ ), low density ( $d_{20} = 4.5 \text{ g/cm}^3$ ) and high corrosion resistance. However, titanium has sufficiently significant capture cross section of thermal neutrons ( $\sigma_a = 5.6 \text{ barn}$ ) and in connection with this it did not find any special application in reactors.

The corrosion stability of titanium in lithium was investigated very little. According to data of Yu. F. Bychkova et al [1], titanium is very little soluble in lithium at  $900^\circ \text{C}$  --  $0.014\%$ . Its stability at  $800-900$  is limited [2].

In this work tests were conducted on technical titanium with impurities of  $0.12\%$  C and  $0.09\%$  Fe, as well as Ti + Al alloy containing  $2.2\%$  Al,  $1.3\%$  Mn and  $0.045\%$  C. Prior to tests in lithium specimens were cleaned from oxides by polishing. Tests were conducted in reaction vessels made of technical titanium.

After testing lithium a change in weight of samples was observed (Table 1).

Technical titanium after testing in lithium gives changes in mass which at  $800-1000^\circ \text{C}$  increase with time of testing and at  $1200^\circ \text{C}$  they decrease in prolonged tests, since after a certain time dissolution of titanium in lithium becomes significant.

Change in Weight of Specimens of Titanium and Ti + Al Alloy  
After Testing in Lithium at 800, 1000 and 1200° C

Material	Time of testing, hours	Change in weight of specimens, mg/cm <sup>2</sup>		
		800° C	1000° C	1200° C
Technical titanium	50	-0.25	-0.10	-0.94
	100	-0.46	-0.56	-0.47
Ti + Al alloy	50	-0.09	-2.46	-4.12
	100	-0.23	-2.44	-4.31

During air heating titanium is coated with a sufficiently strong oxide-nitride film which prevents it from further oxidation at 400-500° C. With increase of temperature the chemical activity of titanium increases and due to high solubility of oxygen and nitrogen in titanium the dissolution of oxide-nitride film is possible and increase of Brinell's hardness to 400-450 kg/mm<sup>2</sup> [3]. After testing in lithium specimens of titanium form surface films and the hardness of the surface increases significantly (Fig. 2). All this shows the ability of titanium to absorb gases from lithium at 800-1200° C.

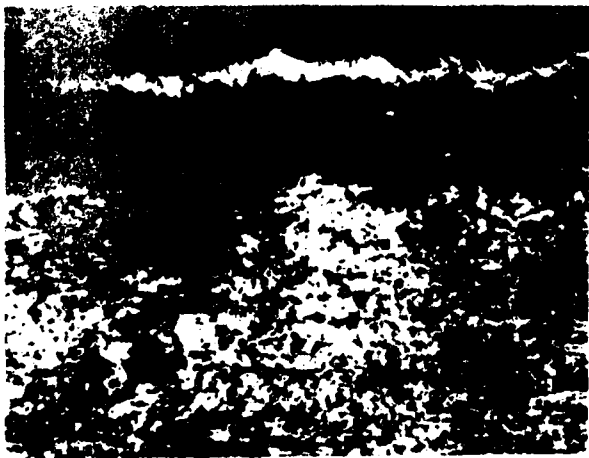


Fig. 1. Microstructure of technical titanium after testing in lithium for 100 hours at 800° C. The surface displays a film but no other changes in structure are observed (200 x).

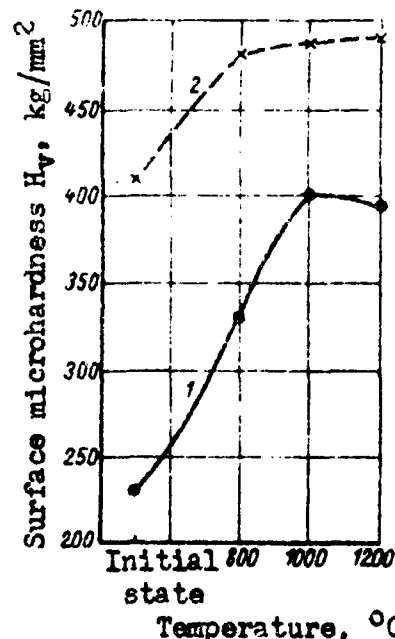


Fig. 2. Change of surface microhardness as a function of temperature after testing in lithium for 100 hours. 1 - technical titanium; 2 - Ti + Al alloy.

Ti + Al alloy displays at all temperatures dissolution processes of the surface layer in lithium which progresses with increase of temperature (Fig. 3). The hardness of the surface increases (see Fig. 2).



Fig. 3. Microstructure of Ti + Al alloy after testing in lithium at 1000° C for 100 hours. Traces of surface solubility in lithium are apparent. The structure is large needle and large grain type (200 x).

The dissolution process of Ti + Al alloy in lithium is aided by the fact that at 800-1200° C one of the components of the alloy -- aluminum -- forms an unlimited region of liquid solutions with lithium [4]. However, during static tests an equilibrium condition is rapidly achieved and increase of the duration of testing of Ti + Al alloy in lithium does not cause increase in solubility.

The mechanical properties of the investigated alloys after testing in lithium are given in Tables 2 and 3.

Table 2

Mechanical Properties of Titanium After Testing for 100 Hours in Argon Atmosphere and in Liquid Lithium (the specimens were bars 1 x 3 x 14 mm)

Testing temperature, °C	$\sigma_b$ , kg/mm <sup>2</sup>		$\delta$ , %	
	Ar	Li	Ar	Li
800	61.1	64.5	23.4	23.1
1000	56.0	57.0	20.7	13.4
1200	60.7	63.9	16.3	4.3

Note: In the initial state  $\sigma_b = 61.5$  kg/mm<sup>2</sup> and  $\delta = 20.4\%$ .

Table 3

Mechanical Properties of Ti + Al Alloy After Testing for 100 Hours in Argon Atmosphere and in Liquid Lithium (the specimens were bars 1 x 3 x 14 mm)

Testing temperature, °C	$\sigma_b$ , kg/mm <sup>2</sup>		$\delta$ , %	
	Ar	Li	Ar	Li
800	66.4	63.7	20.2	21.7
1000	65.3	44.2	13.7	8.8
1200	63.4	48.5	8.1	10.0

Note: In the initial state  $\sigma_b = 70.6$  kg/mm<sup>2</sup> and  $\delta = 17.5\%$ .

The strength characteristics of titanium and of Ti + Al alloy after testing in lithium for 100 hours at 800° C practically do not change. There were no significant changes found in the microstructure with the exception of the thin surface film of increased hardness.

At 1000 and 1200° C titanium and Ti + Al alloy go over into the  $\beta$  phase region and after 100 hours of testing in argon drastic enlargement of structure occurs: grains of enlarged to 3-5 mm in cross section and they have large needles (see Fig. 3). In connection with the formation of large grained structure plastic properties are decreasing (see tests in argon) particularly in Ti + Al alloy.

After testing in lithium at 1200° C the plastic properties of titanium are lowered to a still lower extent since in addition to large grain structure the lowering of plasticity is effected by gases which are absorbed by titanium from lithium. The strength in comparison with tests conducted in argon did not change.

The Ti + Al alloy, due to preferential dissolution of aluminum in metal after testing at 1000 and 1200° C softens and at the same time loses its plasticity. The welding seam of Ti + Al alloy behaves similarly in lithium (Table 4).

In the initial state the welding seam had large grain microstructure. After firing in argon and after testing in lithium at 800° C recrystallization occurred causing formation of smaller grains. At 1000 and 1200° C again large grain structure was formed.

Table 4

Mechanical Properties of Welding Seam of Ti + Al Alloy After Testing for 100 Hours in Argon Atmosphere and in Liquid Lithium (bars 1 x 3 x 14 mm)

Testing temperature, °C	$\sigma_b$ , kg/mm <sup>2</sup>		$\delta$ , %	
	Ar	Li	Ar	Li
800	68,0	65,5	12,7	12,5
1000	64,7	49,5	7,5	5,9
1200	54,9	56,6	5,4	8,8

Note 1: In the initial state  $\sigma_b = 73.8$  kg/mm<sup>2</sup>,  $\delta = 10.4\%$ .

Note 2: Destruction occurred not along the welding seam, but along the transition zone or along the principal metal.

#### Conclusions

1. Technical titanium and Ti + Al alloy have satisfactory stability in lithium at 800° C in the course of 100 hours.
2. During testing of titanium in lithium the former absorbs dissolved gases causing formation of surface films of increased hardness and lowering of plasticity after testing at 1000 and 1200° C. At 1200° C significant dissolution of titanium occurs.
3. In the Ti + Al alloy in connection with the presence of aluminum dissolution processes are developed in the 800-1200° C range. The change of composition causes drastic lowering of the strength and of plasticity after testing at 1000 and 1200° C.
4. The welding seam of Ti + Al alloy behaves in lithium analogously to the alloy itself.

#### BIBLIOGRAPHY

1. Yu. F. Bychkov, A. N. Rozanov and V. B. Rozanova, Metallurgiya i metallovedeniye chistykh metallov (Metallurgy and Metallography of Pure Metals), No. 2, Moscow, Atomic Publishing House, 1960, page 178.
2. P. A. Andreyev, A. A. Kanaev and Ye. D. Fedorovich, Zhidkometallicheskiye teplonositeli yadernykh reaktorov (Liquid Metal Coolants of

Nuclear Reactors), Leningrad. State Publishing House of the Ship Building Industry, 1959.

3. V. N. Yeremenko, Titan i yego splavy (Titanium and Its Alloys), Kiev, Publishing House of the Academy of Sciences of the Ukrainian SSR, 1960.

4. A. Ye. Vol, Stroyeniye i svoystva dvoynykh metallicheskih sistem (Structure and Properties of Binary Metallic Systems), Vol. 1, Moscow, Publishing House of Physics and Mathematics, 1959.

CSO:

CSO: 1879-D

CHANGES OF PROPERTIES DURING CYCLIC THERMAL TREATMENT,  
DURABILITY AND INTERNAL FRICTION OF SAP

A. I. Dashkovskiy  
A. N. Rozanov  
Yu. F. Bychkov  
I. D. Laptev

Multiple heating and cooling causes residual changes of dimensions of metals and alloys under conditions that parameters of cycle have corresponding values.

The changes of shape of metal during cyclic thermal treatment depend on crystal lattice of metal, composition and phase diagram of alloy as well as the shape of tested specimens.

According to the data of A. A. Bochvar et al [1], to obtain a significant residual change of dimensions it is insufficient to have a definite temperature drop, but it is also necessary for the higher temperature of cycle to be above certain value. This upper temperature must be higher than the temperature for intense development of diffusion phenomena.

It is known [1], that aluminum changes significantly its linear dimensions upon repeated heating and cooling. In deformed aluminum the direction and the magnitude of residual deformation under the influence of thermal cycles is practically independent of the degree of deformation and the direction of cutting of specimen with respect to direction of rolling [1], where the length and width of specimen are increasing and thickness is decreasing.

SAP [Spechennaya Alyuminevaya Pudra; Sintered Aluminum Powder] above 350° C surpasses in strength characteristics all deformable aluminum alloys. Consequently it is worthwhile to utilize it as structural material for elevated temperature work. In connection with this the behavior of SAP under cyclic temperature changes is of interest.

In this work the behavior of SAP-1, SAP-2 and technical aluminum AD-1 was investigated during cyclic changes of temperature.

### Procedure and Materials

For cyclic thermal treatment flat specimens were used in the form of 100 x 100 mm plates 0.5 - 1 mm in thickness and specimens in the form of rods 10 - 11 mm in diameter and approximately 90 mm in length. The plates were cut out of rolled sheets and rods were machined from drawn large diameter rods.

The average speed of changes of temperature for plate specimens comprised about 100° C per minute during heating and about 1000° C per second during cooling in water, and for rod specimens 60° C per minute and 600° C per second respectively. Specimens were held at maximum temperature from 10 to 40 min.

The chemical composition of investigated materials SAP-1 and SAP-2 correspond to standard specifications (Table 1).

Table 1

#### Chemical Composition of Materials, %

Material	Al <sub>2</sub> O <sub>3</sub>	Fe	Oils	Moisture
SAP-1	6-11	>0.25	>0.25	>0.1
SAP-2	11-17	>0.25	>0.35	>0.1

In addition to SAP prepared by ordinary means a sheet of SAP produced by rolling briquet, which was annealed in a vacuum for 2 hours at 700° C, was also investigated.

### Results of Investigation

Dimensional Stability. Plates were subjected to cyclic thermal treatment with maximum temperature of cycle being 500, 550 and 600° C. The minimum temperature in all cases comprised 20° C. During cyclic treatment the aluminum specimens obtained the form of Maltese cross. Table 2 gives the average measurements of the length of specimens. Changes of dimensions near the center of plates were much smaller than near the edges.

Table 2

Changes of Dimension of Plate Specimens During  
Thermal Cyclic Treatment

Material	Temperature of cycle, °C (annealing for 10 min.)	Number of cycles	Mean changes of dimensions, %
SAP-1	500-20	240	0
"	550-20	120	-0.2
"	600-20	110	-0.5
SAP-1 from vacuum fired briquet	600-20	110	-0.7
Aluminum	500-20	110	+ 7.0
"	500-20	240	+14.0
"	550-20	120	+ 8.0
"	600-20	110	+11.0

It can be seen from the table that dimensions of aluminum specimens increase significantly in about the same magnitude along the edges, but SAP-1 displays a slight decrease in dimensions. The mean measurements of dimensions of rod specimens during cycling are given in Table 3.

Changes of dimension of cylindrical specimens, as it can be seen from Table 3, occur in the same direction as for plates.

Table 3

Changes of Length of Cylindrical Specimens During  
Thermal Cyclic Treatment

Conditions of cycle	Number of cycles	Change of length, %		
		Al	SAP-1	SAP-2
500-20° C, annealing for 10 min.	90	+0.5	0	0
	210	+1.1	0	0
550-20° C, " " " "	120	+1.0	0	0
600-20° C, " " " "	100	+0.7	-0.3	-0.7

Occurrence of Blisters and Cracks. As the maximum temperature is increased above  $500^{\circ}\text{C}$  during cyclic treatment of plates of SAP, the surface of material begins to show blisters. Their number and dimensions increase rapidly with increase of temperature and blisters tear away from the metal.

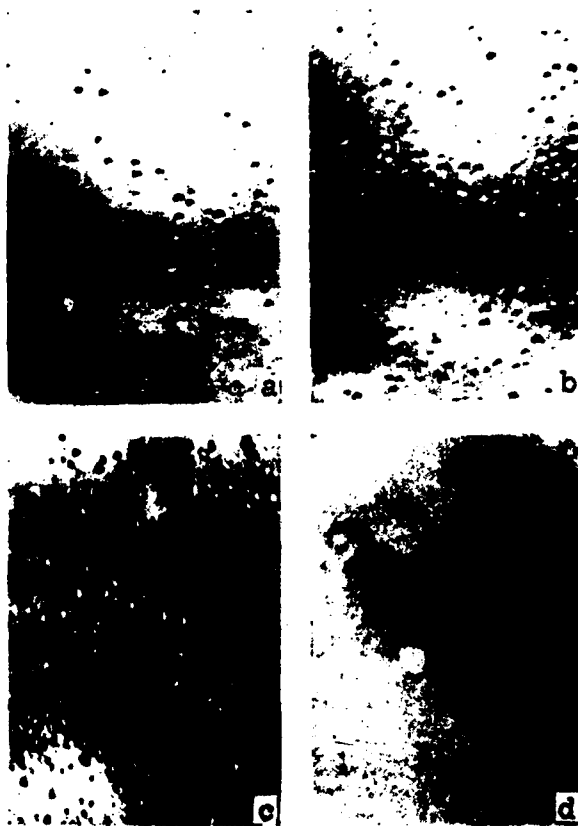


Fig. 1. External view of the same section of surface of SAP-1 plate, subjected to thermal cyclic treatment in  $600-20^{\circ}\text{C}$  range with 10 min. annealing.  
a - after 20 cycles; b - after 50 cycles; c - after 110 cycles; d - rolled from vacuum fired briquet ( $700^{\circ}\text{C}$ , 2 hours) of SAP-1 after 110 cycles.

Figure 1 shows the same section of specimen surface of SAP-1, subjected to cyclic treatment in  $600-20^{\circ}\text{C}$  range with annealing at the maximum temperature for 10 min., after 20, 50 and 110 cycles. The same figure shows a specimen of SAP-1 which was preliminarily annealed in a vacuum at  $700^{\circ}\text{C}$  for 2 hours. After 110 cycles in  $600-20^{\circ}\text{C}$  range this specimen had smooth surface without any evidence of blister formation. It follows that vacuum treatment of SAP enables one to increase significantly its stability to thermal cyclic treatment.

After 110 cycles in 600-20° C range the largest blisters layered forming some sort of scale. Specimens showed cracks which passed through places of formation of blisters. The formation and growth of blisters occurs during firing in the furnace. After cooling new heating to the same temperature does not result in further growth of already existing blisters, but only leads to formation of new ones. The conditions of cycle, as will be shown later, affect significantly the formation of blisters.

Figures 2 a, b and c show photographs of specimens subjected to 30 cycles at 550-20° C. It is apparent that increase of annealing time at maximum temperature of cycle leads to sharp increase of the number and dimensions of blisters. Figure 2 d shows a specimen held isothermally at 550° for 7.5 hours. The specimen in Figure 2 e, passed 18 cycles in 600-20° C range with 15 min. annealing. Here observation was made of a definite section of surface of specimen after each cycle. These observations have shown that growth of blister occurs only during continuous holding in the furnace. After cooling the blisters which have been formed do not display any external changes in the course of subsequent heating. Only new blisters occur. All large blisters under the indicated conditions of treatment were formed during the first four cycles. Blisters are oriented along the direction of rolling, which is extremely noticeable in the case of small blisters (see Fig. 2).

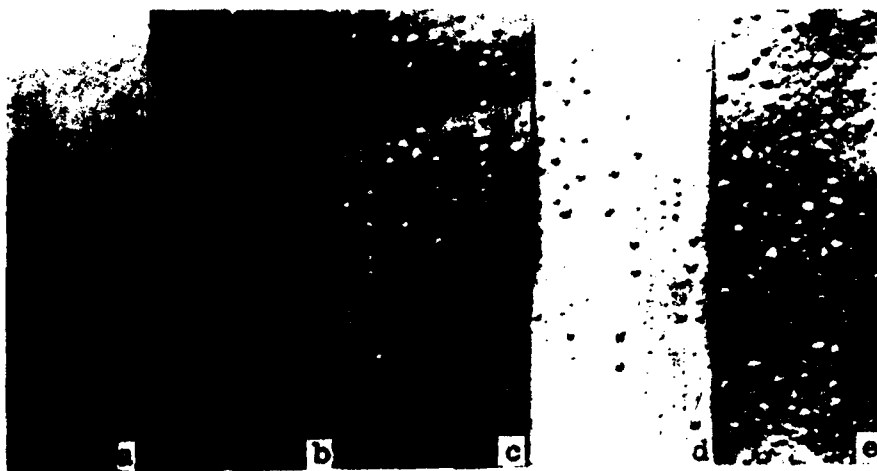


Fig. 2. Surface of SAP-1 plate after different treatments.  
a - after 30 cycles at 550-20° C, annealing for 20 min, air cooled;  
b - after 30 cycles at 550-20° C, annealing for 20 min, water cooled; c - after 30 cycles at 550-20° C, annealing for 40 min, water cooled; d - annealing at 550° C for 7.5 hours; e - after 18 cycles at 600-20° C, annealing for 15 min, water cooled.

The internal surface of blisters after multiple cycling or prolonged annealing at maximum temperature is black, but initially after formation of blister, for example 5 min. after annealing at 600° C, it is absolutely light, not differing from the appearance of fresh break in SAP.

The rod specimens of SAP do not have a significant number of blisters upon cycling, but the occurrence of cracks is more rapid than in the case of plates. During cyclic treatment at 600-20° C significant cracks occurred on the surface of rods after 30 cycles. Cracks are directed along the axes of specimens and their number increases with increase of the number of cycles (Fig. 3 a). During cycling from 550° C cracks did not appear even after 120 cycles (see Fig. 3 b).



Fig. 3. External appearance of rods Al (I), SAP-2 (II) and SAP-1 (III) after cyclic treatment.  
a - after 100 cycles at 600-20° C, annealing for 10 min, (1.0 x);  
b - after 120 cycles at 550-20° C, annealing for 10 min, (0.85 x).

**Mechanical Properties.** Table 4 shows mean results of three-four specimens of mechanical properties of sheet SAP-1 at room temperature after different conditions of thermal treatment.

As it is apparent from Table 4, thermal cycling leads to lowering of strength and plasticity of SAP. With increase of annealing time at maximum temperature of cycle  $\sigma_b$  and  $\delta$  decrease (see specimens No. 4 and 5 in Table 4). At low rates of cooling mechanical properties of material are better than after the same number of cycles yet with faster rate of cooling (see

specimens No. 4 and 6 in Table 4). After annealing at 550° C without cycling the properties of SAP become worse and even poorer than after cycling: after 20 hours at 550° C specimens which passed 120 cycles with 10 min. annealing properties changed less than after 15.5 hours of annealing at the same temperature (see specimens No. 3, 7, 8 in Table 4). As a result of thermal cycling from 600° C the strength limit of vacuum annealed SAP at 700° C was somewhat lowered and relative elongation increased significantly (see specimens No. 9, 10 in Table 4).

Table 4

Mechanical Properties of SAP-1 Sheet at Room Temperature  
After Various Thermal Cyclic Treatments

Specimen number	Treatment	Yield strength $\sigma_b$ , kg/mm <sup>2</sup>	Relative elongation, %
1	Initial state . . . . .	39.7	3.5
2	240 cycles at 500-20° C with 10 min. annealing, water cooled . . . . .	32.9	2.7
3	120 cycles at 550-20° C with 10 min. annealing, water cooled . . . . .	34.1	3.4
4	30 cycles at 550-20° C with 20 min. annealing, water cooled . . . . .	30.1	1.7
5	30 cycles at 550-20° C with 40 min. annealing, water cooled . . . . .	26.8	1.2
6	30 cycles at 550-20° C with 20 min. annealing, air cooled . . . . .	33.0	2.3
7	Annealing at 550° C, 7.5 hours . . . . .	30.8	2.1
8	Annealing at 550° C, 15.5 hours . . . . .	29.7	2.1
9	Sheet made from briquet, fired in vacuum at 700° C for 2 hours . . . . .	33.2	5.2
10	Same + 110 cycles at 600-20° C, with 10 min. annealing, water cooled . . . . .	29.3	9.4

Microstructure. The structure of hot rolled strip is characterized by clearly expressed line distribution of oxide phase particles. Thermal cycling of SAP-1 plates in 600-20° C range with 10 min. annealing at maximum temperature leads to formation of a large number of approximately equal in size fine pores which are uniformly distributed (Fig. 4). The formation of cracks occurs by conglomeration of a group of smaller pores into a larger pore. As a result of gas pressures inside the pore great local stresses occur in the surrounding material and cracks are developed which pass through the neighboring small pores. Formation of cracks near the surface of the specimen leads to formation of blister. Fig. 5 shows a

section of crack near the surface of specimen in the initial moments of formation of blister. At 550° C pores which are formed are smaller and cracks are shorter and consequently the number of blisters and their dimensions on the surface decrease.

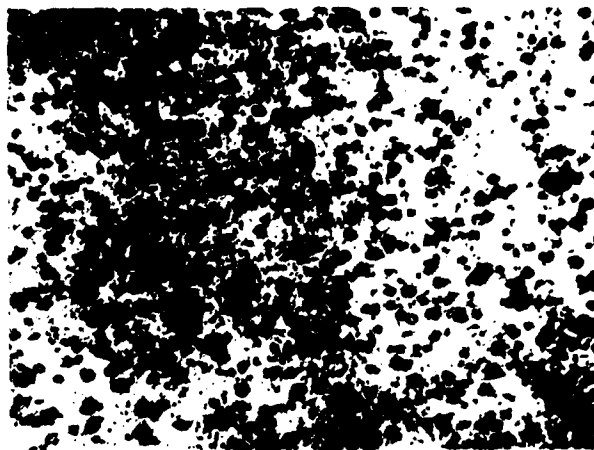


Fig. 4. Microstructure of SAP-1 after 110 cycles at 600-20° C and 10 min. annealing at maximum temperature (600 x).



Fig. 5. Microstructure of SAP-1 after 110 cycles at 600-20° C and 10 min. annealing at maximum temperature. The area of crack formation and formation of blister (600 x).

The microstructure of SAP-1 rods after 120 cycles in 550-20° C interval with 10 min. annealing is shown in Fig. 6. Sheet aluminum tested under the same conditions after 110 cycles in 600-20° C interval (annealed at 600° C for 10 min.) had larger number of thin cracks and aluminum rods had many large round pores located along the grain boundaries.

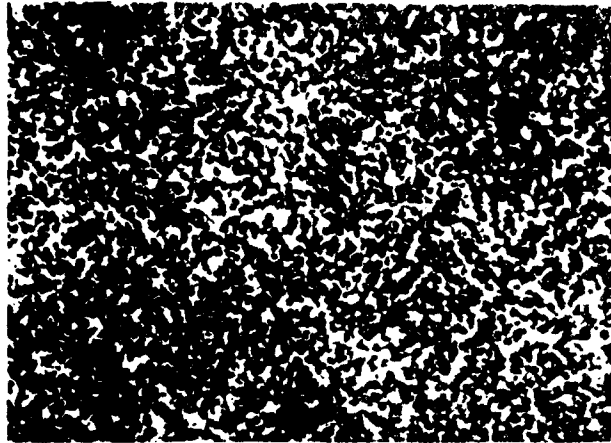


Fig. 6. Microstructure of SAP-1 rod after 120 cycles at 550-20° C with 10 min. annealing (450 x).

#### Discussion

The experiments on dimensional stability have shown (see Tables 2 and 3) that significant changes in dimension of SAP plates occur when the maximum temperature of cycle is 550° C or higher and for rods -- 600° C, i.e. higher than the temperature of normal use of these materials.

To obtain a significant residual change of dimensions it is necessary [1] for upper temperature of cycle to be not lower than the temperature at which recrystallization occurs or the temperature of sufficiently strong development of diffusion phenomena.

During study of recrystallization of SAP it was found [2] that in cold deformed SAP (less alloyed  $Al_2O_3$ ) the processes of growth of recrystallization centers are separated by a significant temperature interval. The formation of nuclei begins at the same temperature as in pure aluminum, i.e. about 175-200° C, and their growth only at 350-375° C, i.e. when self diffusion of aluminum becomes sufficiently intense. The formation of recrystallization nuclei has smaller effect on weakening of material than their growth.

Considering short duration of cycles and greater content of  $Al_2O_3$  in these specimens than in the work of S. S. Gorelka et al [2] it is

possible to consider significant changes of SAP dimensions during cyclic thermal treatments, starting at  $550^{\circ}\text{C}$ , are in good agreement on recrystallization data of this material.

Changes of mechanical properties of SAP during cycling are apparently the result of large pores and cracks, accompanied by formation of surface blisters. These processes are on one hand dependent on duration of high temperature treatment (formation of pores and uniting of pores to form larger pores, formation of cracks) and on the other hand on the rate of cooling (formation of thermal stresses). Therefore, the increase of time of annealing at the maximum temperature of cycle and increase of the rate of cooling leads to more significant lowering of mechanical properties of SAP.

It is very significant that SAP-1 plate rolled from vacuum annealed briquet at  $700^{\circ}\text{C}$  for 2 hours, after 110 cycles in  $600-20^{\circ}\text{C}$  range had no cracks, blisters or large pores.

#### Durability of SAP-1

Durability tests were conducted on SAP-1 specimens 3 mm in diameter and working length of 20 mm at  $375$ ,  $450$  and  $550^{\circ}\text{C}$  under the influence of various stresses. Figures 7 and 8 show graphs of time prior to destruction of specimen as a function of applied stress for  $375$  and  $450^{\circ}\text{C}$ . Since each point represents a test of individual specimen a significant scattering of experimental data is observed. Thus graphs are bounded by two lines, where the included area contains all points.

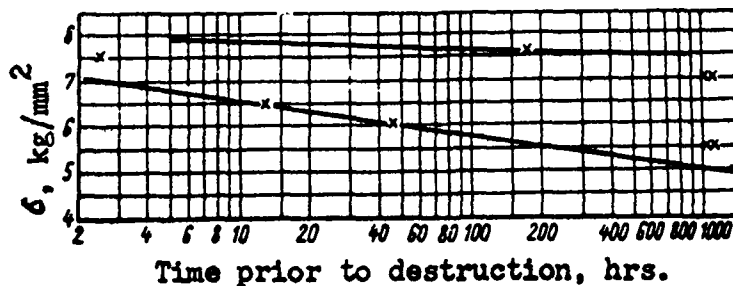


Fig. 7. Durability of SAP-1 at  $375^{\circ}\text{C}$ .

It is possible to assume that the lower boundary of the region may be taken as the criterion of strength of SAP at indicated temperatures. It follows that SAP is quite thermally stable, surpassing thermal stability characteristics of the most stable aluminum alloys. Thus, for example, the durability (100 hours) strength of sheet material D-20 at  $350^{\circ}\text{C}$  is  $4\text{ kg/mm}^2$ , AK-4 alloy --  $3\text{ kg/mm}^2$ , VD-17 alloy at  $320^{\circ}\text{C}$  --  $3.5\text{ kg/mm}^2$  [3].

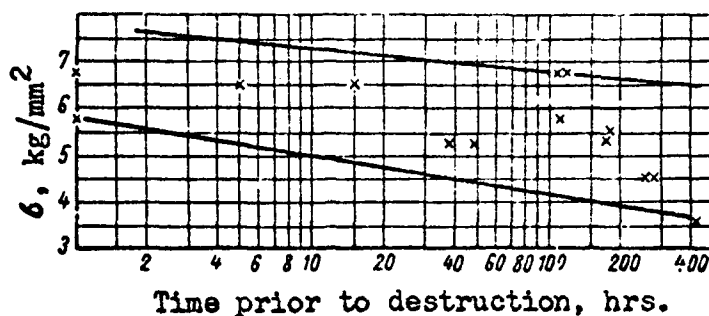


Fig. 8. Durability of SAP-1 at 450° C.

It is apparent from Figures 7 and 8 that material from sintered aluminum powder SAP-1 has 100 hour durability at 375° C in 5.5-7.5 kg/mm<sup>2</sup> limits and at 450° C -- from 4.0 to 6.5 kg/mm<sup>2</sup>.

At 375° C destruction of specimens occurred without residual elongation and at 450° C a residual elongation was observed of the order of 0.5%. The specimens tested at 550° C broke primarily at the point of transition from the working part to the head. It is interesting that specimens with special notches were not broken in the place of the notch. This shows that at 550° C structural changes cause the predominant effect on destruction of specimens. These structural changes occurred in SAP in this temperature interval even in the absence of load -- formation of porosity and cracks.

The durability (100 hours) of SAP at 500° C is equal to 5 kg/mm<sup>2</sup> [4]. The fact that some samples displayed high values of durability indicates the possibility of increasing the durability of SAP to values which are close to the upper boundary of the region by improving the production technology.

#### Internal Friction of SAP-1

Investigations were conducted on the relaxation behavior of SAP-1 in order to clarify the effect of finely dispersed second phase (aluminum oxide) in the metallic matrix. Specimens of two compositions were investigated with aluminum oxide content of 3-4 and 7-11%. Specimens were in the shape of wire 3 mm in diameter and 320 mm long. Investigations were conducted on the vacuum set-up of the twisting pendulum type [5]. The temperature dependence of the internal friction and of shear modulus were determined. The internal friction  $Q^{-1} = \delta/\pi$ , where  $\delta$  is a logarithmic decrement of damping of free twisting oscillations of specimens and shear modulus  $G$  is determined in the frequency function of oscillations.

The investigated alloys having a matrix of technically pure aluminum containing finely dispersed second phase of aluminum oxide. Aluminum oxide is present in these materials in the form of fine scales since in the

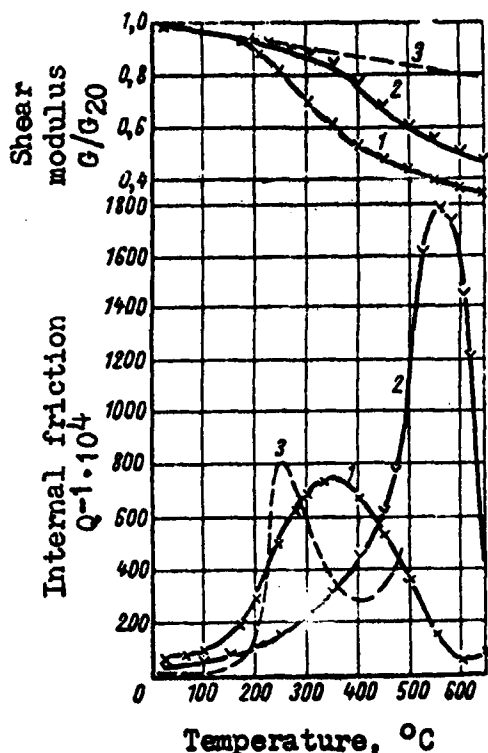


Fig. 9. Internal friction and shear modulus of SAP as a function of temperature.  
 1 - 3-4%  $Al_2O_3$ ; 2 - 7-11%  $Al_2O_3$ ; 3 - Al (from the data of [6]).

specimens containing 3-4%  $Al_2O_3$ , 560° C for specimens containing 7-11%  $Al_2O_3$  at frequencies 1.86 and 1.68 cycles per second respectively. As a result of vacuum annealing above 500° C the maximum on the curve lowered somewhat and for large grained recrystallized specimens, annealed for 5 minutes at 650° C it almost completely disappeared.

In work [7] the internal friction of SAP made MD-2100 was investigated. Here an internal friction peak was found lying in the 254-321° C interval during changes of frequency from 0.9 to 1.8 cycles per second. In our case for specimens containing 3-4%  $Al_2O_3$  the internal friction peak at 1.86 cycles per second was observed at 350° C. In the specimen of the same composition after annealing at 500° C (for 20 minutes) the internal friction peak lowered somewhat shifted in the direction of higher temperature and was observed at 380° C.

In one of the works [8] data are given on the modulus of elasticity of SAP and it is indicated that its damping ability is very great: the logarithmic decrement is approximately 20 times larger than for pure aluminum.

process of production of semifinished products from SAP destruction of oxide film occurs. Breaking up of powder particles and distribution of aluminum oxide in the form of finely dispersed inclusions throughout the whole volume. The specimen containing a large amount of aluminum oxide is characterized by finer grain size and more uniform structure than the specimen with smaller content of  $Al_2O_3$ .

The internal friction was investigated in the temperature interval from 20 to 650° C.

Figure 9 shows the temperature dependence of internal friction of SAP-1 specimens containing 3-4%  $Al_2O_3$  (curve 1) and containing 7-11%  $Al_2O_3$  (curve 2). For comparison temperature dependence on the internal friction of polycrystalline aluminum is given (curve 3) from the data of V. S. Postnikov [6].

For fine grain specimens of SAP-1, not recrystallized after drawing wire the internal friction curve displayed a peak lying at 335° C for

As it is apparent from Figure 9 the internal friction at room temperature in SAP is higher than aluminum. However, at 600° C the internal friction of SAP is much lower than in aluminum at 400° C. According to the work of V. S. Postnikov [6] the level of internal friction at elevated temperatures is associated with heat resistance of the material: the more heat resistant is the material the lower is the internal friction. This is verified by the example of aluminum and SAP.

In the work [8] the following values of moduli are given: normal modulus of elasticity of aluminum 6700-7000 kg/mm<sup>2</sup>, normal modulus of elasticity of SAP on the average 7500 kg/mm<sup>2</sup>, shear moduli for SAP and for aluminum within 2500-3000 kg/mm<sup>2</sup> limits.

We determined the values of moduli at room temperature for SAP of two compositions: with 3-4 and 7-11% Al<sub>2</sub>O<sub>3</sub>. The shear modulus was determined on the same set-up as the internal friction. The normal modulus of elasticity was determined by the resonance method during bending oscillations of specimens. The following values were obtained: for SAP with 3-4% Al<sub>2</sub>O<sub>3</sub> shear modulus is 2400 kg/mm<sup>2</sup> and the normal modulus of elasticity 6500 kg/mm<sup>2</sup>, and for SAP with 7-11% Al<sub>2</sub>O<sub>3</sub> the shear modulus is 2600 kg/mm<sup>2</sup> and the normal modulus of elasticity 7350 kg/mm<sup>2</sup>.

The nature of peaks of the internal friction in SAP differs from the grain boundary peak in polycrystalline aluminum. Although the height of maximum is associated with grain size, the large widths of maxima and the dependence of their heights on the amount of second phase indicates that relaxation in the SAP is a completely dependent process from grain boundary relaxation in the single phase aluminum alloys.

The occurrence of internal friction peak is accompanied by the relaxation of shear modulus, which is more significant specimens with lower content of aluminum oxide. After high temperature annealing, leading to lowering of the internal friction peak, the relaxation of shear modulus is also decreased.

Investigations were conducted on the internal friction in SAP made MD-2100 [7] and the energy of activation of relaxation for this alloy was determined, which was found to be approximately equal to 6 k cal/mole, i.e. its magnitude is significantly less than the activation energy for spontaneous diffusion in single phase aluminum alloys, which is approximately 36 k cal/mole. The authors of [7] believe that the internal friction peak in SAP occurs as a result of time dependent initiation of dislocations from grain boundaries in the specimen.

It is possible to assure that the increase of content of Al<sub>2</sub>O<sub>3</sub> in SAP leads to increase of the energy of activation for the formation of dislocation centers along the grain boundaries. In connection with this the internal friction peak in specimens with high Al<sub>2</sub>O<sub>3</sub> content is observed at higher temperatures and the shape of peak changes so that its height increases and width decreases.

The powder which is used for production of SAP with lower  $Al_2O_3$  content had smaller elementary particle size than powder for production of SAP with higher  $Al_2O_3$  content.

In the process of production of powder lumping occurs -- formation of larger particles due to sticking together of elementary particles of aluminum. The lesser is the  $Al_2O_3$  content in the powder the larger is the nonuniformity in size of clumped particles. Since grains in the specimen are crushed during pressing and drawing clumped powder particles, the structure of ready specimen will depend to a significant extent on its production technology. With all other things being equal specimens with lower  $Al_2O_3$  content have greater nonuniformity of structure in grain size as well as in dimensions of dispersed particles of aluminum oxide.

Thus, different peak heights on internal friction curves may be associated with different grain size in the specimens, and the large width of these peaks -- with the presence of not just one relaxation time, but the whole spectrum of closely spaced relaxation times.

#### Conclusions

1. TsTO [Tsiklicheskaya Termicheskaya Obrabotka; cyclic thermal processing] causes significant changes in SAP with maximum temperature of cycle being  $550^\circ C$  and higher. Here a decrease of longitudinal and increase of lateral dimensions takes place.
2. As a result of TsTO at  $500^\circ C$  and above the material becomes more brittle and brittleness increases with increase of the number of cycles. The mechanical properties are degenerating. The yield strength and plasticity are decreasing.
3. In the temperature range up to  $500^\circ C$  SAP along with highly favorable mechanical properties is also dimensionally stable during TsTO.
4. The SAP plate rolled from a briquet, annealed in a vacuum at  $700^\circ C$  for 2 hours, possesses higher plasticity and somewhat lower strength as compared with normal SAP and does not have any cracks or blisters upon TsTO with heating up to  $600^\circ C$ .
5. SAP-1 of standard composition possesses greater thermal stability than other aluminum alloys. Its durability (100 hours) comprises  $5.5-7.5 \text{ kg/mm}^2$  at  $375^\circ C$  and  $4.0-6.5 \text{ kg/mm}^2$  at  $450^\circ C$ .
6. SAP-1 in fine grained unrecrystallized state has an internal friction peak, the height and position of which on the temperature curve depends on the grain size and the content of the second finely dispersed phase in the aluminum --  $Al_2O_3$ .

## BIBLIOGRAPHY

1. A. A. Bochvar et al, "The Effect of Cyclic Heating and Cooling on Dimensional and Structural Stability of Various Metals and Alloys," Trudy Vtoroy Mezhdunarodnoy Konferentsii po Mirnomu Ispol'zovaniyu Atomnoy Energii. Doklady Sovetskikh Uchenykh (Works of the Second International Conference on the Peaceful Uses of Atomic Energy. Reports of Soviet Scientists), (Geneva, 1958), Vol. 3, Yadernoye Goryucheye i Reaktornyye Metally (Nuclear Fuel and Reactor Metals), Moscow, Atomic Publishing House, 1959, page 554.
2. S. S. Gorelik, A. I. Litvintsev and E. P. Belova, "Characteristics of Recrystallization of SAP," Teploprochnyy Material iz Spechenoy Alyuminiyevoy Pudry (SAP) (Refractory Material from Sintered Aluminum Powder), Moscow, State Defense Publishing House, 1961, page 88.
3. M. V. Mal'tsev, T. A. Barsukova and F. A. Borin, Metallografiya Tsvetnykh Metallov i Splavov (Metallography of Nonferrous Metals and Alloys), Moscow, Metallurgical Publishing House, 1960, page 162.
4. I. N. Fridlyander, Alyuminiyevyye Deformiruyemye Splavy, Primenyayemye Dlya Raboty Pri Povyshennykh Temperaturakh v SSSR i za Granitsey (Deformable Aluminum Alloys Utilized for Work at Elevated Temperatures in the USSR and Abroad), Moscow, State Defense Publishing House, 1957.
5. A. I. Dashkovskiy, A. I. Yevstyukhin and Ye. M. Savitskiy, Metallurgiya i Metallovedeniye Chistykh Metallov (Metallurgy and Metallography of Pure Metals), Issue 2, Moscow, Atomic Publishing House, 1960, page 207.
6. V. S. Postnikov, Uspekhi Fizicheskikh Nauk (Advances in Physical Sciences), Vol. 66, No. 1, 1958, page 43.
7. G. S. Ansell and P. E. Arnold, Trans. Metallurg. Soc. AIME, Vol. 221, No. 1, 1961, page 206.
8. K. E. Mann and M. B. Boudouresques, Fuel Element Fabricat., Vol. 1, London-New York, Academy Press, 1961, page 145.

6101  
CSO: 1879-D

THE MECHANICAL PROPERTIES OF BERYLLIUM  
AFTER ZONE RECRYSTALLIZATION

I. V. Milov  
D. M. Skorov  
V. V. Nikishanov

The extensive use of beryllium as a structural material is restricted by its brittleness at room temperature. At present, several courses in studying the possibilities of obtaining plastic beryllium have become apparent. There are: mechanical and heat treatment of beryllium ingots to bring about a definite alignment of crystallites in the beryllium, the alloying of beryllium in order to fix a high-temperature  $\beta$  phase with a cubic lattice, the obtention of a fine-grained structure (up to 25  $\mu$ ) by means of power metallurgy, and finally, the purification of beryllium. In order to purify beryllium from admixtures, operations dealing with the distillation of beryllium and the thermal decomposition of its halogenides are carried out; an alternative means of purification is by means of zone recrystallization. In the published works on the zone recrystallization of beryllium it is shown that the successful purification of beryllium from admixtures favorably affects its mechanical properties [1, 2].

The present article describes results of compression tests on specimens cut out from beryllium ingots that had been subjected to zone recrystallization. Zone recrystallization was carried out by the electric arc method in a copper, water-cooled crucible in an atmosphere of purified argon. After zone recrystallization, the beryllium ingots constituted horseshoe-shaped ingots with a diameter of 80 mm and a length of 140 - 150 mm.

From the ingots, specimens were prepared not, as conventionally, for a rupture test but for a compression test. This is to be explained, in the first place, by the fact that the ingot height of 12 - 15 mm did not permit microspecimens for rupture tests to be cut out perpendicularly to the axis of the ingot; in the second place, it was impossible to cut out specimens from the ingot along its axis due to its horseshoe shape and the uneven distribution of admixtures with respect to ingot length. Visual examination of various cross sections of an ingot showed that when beryllium undergoes zone recrystallization in a copper, cooled crucible at a zone-movement rate of 0.75 mm/min, explicitly expressed acicular crystallization is observed. The grains grow from the bottom and walls of the crucible, and bend in the direction of movement of the zone

(Figure 1). In the upper part of the ingot the grains grow almost parallel to the ingot axis, forming as it were a zone of platelike grains. The length of the grains attains 40 - 45 mm, and their cross section is equal to 2 x 3 mm.

In order to study the mechanism of deformation of the polycrystalline specimens, it was desirable to determine the position of the crystallographic axes in the beryllium grains. According to the theory of the crystallization of metals from a fusion, the characteristic direction of growth for a hexagonal lattice is the direction  $[10\bar{1}0]$  [4]. X-ray studies of immobile sectors of an ingot with respect to reflection by the Laue method, carried out by us with a sharp-focus tube with Cu-radiation, showed that no sharply defined orientation of the crystallographic axes in the grains is observed under the given conditions of their growth. The x-ray photographs obtained make it possible to arrive at the conclusion that the grains constitute monocrystals with misorientation of the blocks to the extent of several degrees. Some of the photographs indicate the presence of second-order symmetry, and permit the supposition to be expressed that the base plane (0001) is approximately orthogonal to the direction of grain growth, and deviates by small angles from parallelness with the crystallization surface. It should be noted that decoding of the epigrams [rasshifrouka epigramm] also becomes more complicated due to the presence of spots caused by the reflection of internal (from the point of view of the surface photographed) beryllium grains on the planes. This orientation is observed in ingot grains at distances not closer than 1 - 1.5 mm from the bottom and walls of the crucible.

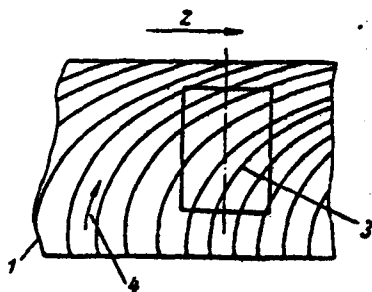


Figure 1. Diagram of grain growth in a beryllium ingot in the case of zone recrystallization in a copper, cooled crucible

- 1 - part of ingot
- 2 - direction of zone motion
- 3 - specimen for testing
- 4 - direction of grain growth

In the work of Garber et al., [4], an investigation was made of the anisotropy of the microhardness of a beryllium monocrystal. It was established that the microhardness is represented by an ellipsoid of rotation about a sixth-order axis with an axis ratio equal to 0.6 (along the  $c_6$  axis -- 350 kg/mm<sup>2</sup>, perpendicularly to axis  $c_6$  -- 217 kg/mm<sup>2</sup>). Similar research was carried out by Kaufman and collaborators, and by Russel [6]. They obtained analogous results.

We measured the microhardness of vertical (transverse to the ingot axis) sections after zone recrystallization at various distances from the beginning of the ingot after a varying number of passes. It was established that in specimens subjected to the recrystallization zone with a varying number of zone passes, the microhardness of vertical sections increases from the lower layers to the upper ones. Figure 2 shows the microhardness distribution of one of the vertical (transverse) sections. In specimens after one and two passes the microhardness of vertical sections deviated somewhat from the microhardness distribution law shown in Figure 2. Measurement of the microhardness according to the height of vertical axial sections of the ingot yielded microhardness values that differed little from one another and that were almost equal to minimal microhardness values of the upper (transverse) sections. On the basis of microhardness measurements in comparison to works [4, 5], starting with the consideration that grains in ingots constitute monocrystals and that crystallographic axes in the ingots are oriented in almost the same manner, we arrived at the conclusion that the base plane is, with small deviations, located in the ingots perpendicularly to the direction of grain growth. This conclusion confirmed the results of x-ray research. The position of planes (1010) and (1120) in a growing grain was not established.

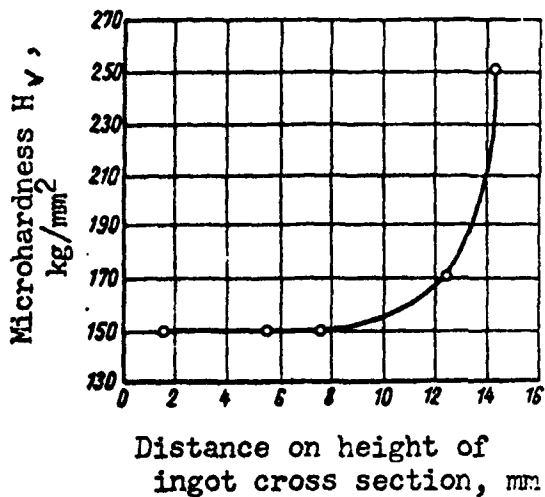


Figure 2. Microhardness of section of vertical cross section at distance of 105 mm from beginning of ingot after six zone passes at a rate of 0.75 mm/min.

This conclusion differs somewhat from the one expressed above concerning the characteristic growth direction of hexagonal lattice. However, as has been shown in the survey work of V. O. Yesin [6], as metal purity increases and, consequently, as concentrational overcooling and the crystallization rate diminish, a change can take place in the directions of the principal growth of the crystals. This has its effect on the change of the crystallographic orientation of the dendritic axes and of the texture in the acicular zone of the ingot [6]. Martins [3] and Edmunds [7] have shown that, depending on the temperature gradient and the growth rate,

in the growth of monocrystals in the case of zinc and cadmium the base may be situated perpendicularly to the axis of the specimen, i.e., parallel to the crystallization front.

The same should, apparently, be observed in the case of beryllium. Possibly that is what we did observe, since zone recrystallization takes place at very low crystallization rates and at small overcoolings. Besides, it must be noted that crystallization starts at the crucible walls, with a large number of centers of crystallization with most highly variegated crystallographic orientation; this must also complicate the crystallization process.

According to the data in the literature, the value of beryllium plasticity depends to a great extent on the predominant orientation of the grains and on their size. Therefore specimens for compression testing were cut out of the ingot in such a manner that they all have the same position of the grains and almost the same size. Specimens in the shape of cylinders were cut out of various sectors of an ingot (beginning, middle, end), perpendicularly to its axis, by the electric spark method. Then the specimens were machined on a lathe to the following dimensions: height  $9 \pm 0.01$  mm, diameter  $7 \pm 0.01$  mm. In the course thereof, layers above and below a specimen with unclearly defined orientation of the crystallographic axes in the grains were shaved off during machining. To remove the stresses that might originate in the specimens during machining the specimens were annealed at a temperature of  $900^\circ\text{C}$  for two hours. For this they were wrapped in molybdenum foil, and were placed in a quartz ampoule in which a vacuum of  $10^{-4}$  mm Hg was maintained during annealing. The surface of the specimens was painstakingly examined with a microscope in order to detect microcracks that may originate in the course of electric-spark and mechanical processing. The base planes (0001), along which, according to data in the literature, a shift takes place at room temperature, were in our specimens situated approximately at an angle of  $50^\circ$  to the axes of said specimens.

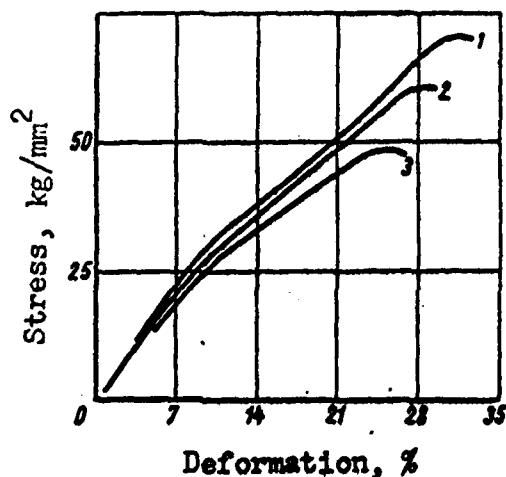


Figure 3. Compression curves of specimens cut out from a beryllium ingot after four zone passes

- 1 - beginning of ingot
- 2 - middle of ingot
- 3 - end of ingot



Compression tests of the samples were carried out on a TsNIITMash-I machine with a maximum load of 4,000 kg with recording of the curve. In case of the compression of beryllium, load-deformation curves are similar to the compression diagrams of plastic metals. Figure 3 shows compression curves of specimens cut out from a beryllium ingot after four passes of the zone. Compression curves of specimens cut out from ingots after 1, 2, 3, and six passes of the zone are similar. On all curves, the viscosity platform is missing. This may be explained by an increase in the purity of the metal and an increase in the size of its grains [8]. The results of compression testing are shown in the table. From this table it can be seen that the greatest strength and plasticity is possessed by initial sectors of the ingots. We have established that in the case of arc-type zone recrystallization of beryllium, impurities both metallic and non-metallic are generally shifted to the end of the specimen. The initial portions of the ingots are freest of all from admixtures. Therefore it may be considered that as the content of impurities in beryllium increases, its strength limit and its plasticity diminish. The high values of ultimate strength and yield are possibly to be explained by the small dimensions of the specimens. It was visually observed that in compression testing, some samples curled slightly about their axis. Some of the specimens (predominantly initial ones) assumed a barrellike shape (Figure 4).



Figure 4. Specimens after compression testing (magnified 1.5 times).

After the deformation of some specimens with loads below  $\sigma_T$ , when their structure was examined under a microscope wave-shaped shift patches were observed in the base plane. With an increase in the loads, cracks appear in the base plane. At high values of deformation, i.e., at loads above  $\sigma_T$ , a shift takes place with respect to the prismatic planes, transversely to and along them. It is possible that the origination of cracks in the base plane begins to hinder slippage along this plane, and the deformation mechanism in case of the com-

pression of polycrystalline specimens of beryllium changes. One should not exclude from consideration the possibility that the pronounced block structure of the grains themselves hinders slippage along the base plane, and the fact that it is this that explains the high yield value. However, a shift with respect to prismatic planes does not contribute much to the value of the deformation. Parallel to said shift, strong slippage was also observed with respect to grain boundaries, the latter type of slippage

becoming subsequently the predominant one. Therefore it is difficult to determine which of them is more responsible for the deformation of polycrystalline beryllium at stresses in excess of the yield point. The deformation value corresponding to the yield point is also the greatest in the specimens from the beginning of the ingots, and rises as the number of zone passes is increased. It must be noted that study of the deformation and of the plastic properties of polycrystalline beryllium after zone recrystallization in a crucible is hindered by the uneven growth of grains in the ingot. Therefore it would prove useful to carry out research concerning the mechanism of the deformation of polycrystalline beryllium with normal grain growth.

#### BIBLIOGRAPHY

1. Mitchell, W. R., Mullendore, J. A., Maloof, S. R., Transactions of the Metallurgical Society AIME, 221, 824 - 826 (1961).
2. Martin, H., Graud, E., Spangler, "The Flow and Fracture Characteristic of Zone-Melted Beryllium" The Institute of Metals. Conference on the Metallurgy of Be. London, 16 - 18 October 1961
3. Martius, U. M., In the collection: Uspekhi fiziki metallov (Advances in the Physics of Metals), Vol. 1, Moscow, Metallurgizdat, 1958, p. 248.
4. Garber, R. I., et al., "Determination of the Anisotropy of the Microhardness of Crystalline Beryllium," Fizika metallov i metallovedeniye (The Physics of Metals and the Study of Metals), Vol. IX, No. 2, 1961, p. 274.
5. Collection: Berilliy (Beryllium), edited by M. B. Reyfman. Moscow. Foreign Literature Publishing House, p. 332.
6. Yesin, V. O., "The Direction of the Predominant Growth of Metallic Crystals from a Fusion," Fizika metallov i metallovedeniye, Vol. X, No. 2, 1960 [sic] p. 233.
7. Edmunds, G., Trans. ASME, 143, 183 (1941).
8. Ransin, Ya. P., "Concerning the Mechanism of the Initial Stage of the Deformation of Polycrystalline Metals," Fizika metallov i metallovedeniye, Vol. 14, No. 4, 1959, p. 631.

6306

CSO: 1879-D

INSTALLATION FOR THE X-RAY STRUCTURAL ANALYSIS  
OF RADIOACTIVE MATERIALS

Yu. I. Gribanov  
A. G. Karmilov  
I. A. Lednev

Investigation of the mechanism of radiation disruptions in the crystalline lattice of metals and alloys is a pressing task in the contemporary science of metals. This research is of applied significance as regards reactor construction, since radiation disruptions in the lattice have a significant effect on the physical and mechanical properties of structural materials.

The highly developed facilities of x-ray technology are available for study of the crystalline structure of materials. But samples of materials exposed to radiation in a reactor have strong induced activity, and themselves constitute sources of various types of radiation, the greatest amount of interference coming from  $\gamma$ -radiation. The intensity of the abovementioned type may exceed by many orders of magnitude the intensity of a useful x-ray beam. And since every detector of x-radiation is sensitive also to  $\gamma$ -radiation, direct utilization of the methods and apparatus of x-ray structural analysis under these conditions becomes difficult or simply impossible.

Of course it is possible to hold the specimen preliminarily for the period of time necessary for the induced activity to fall off to a sufficiently low level [1, 2]. However, the protracted delay of information (dozens of months) makes such a method unacceptable in the general case.

In designing installations for the x-ray structural analysis of radioactive materials, it is necessary to solve the problem of separating the useful radiation from the interfering radiation on the basis of such a one of their properties or criteria whereby it is possible sharply to reduce or completely to exclude the influence of the interfering radiation on the detector of the reflected x-radiation.

Attention should also be paid to increasing the intensity of the primary x-ray beam, for example by the use of sharp-focusing tubes, pulse feeding, etc. However, serious technological difficulties are encountered in this course. At present, it is considered very advantageous that an

installation for the x-ray structural analysis of radioactive materials be produceable from series-produced components under the conditions of an average metal-research laboratory, with a minimum of adaptation. All equipment developed over the past few years manifests a particular reliance on series-produced components.

Let us briefly consider the operating principles of the currently known installations. One of the installations [3] consists of a simple diffractometer in which the x-radiation detector is a scintillation counter [a photomultiplier with a thin NaI (Tl) crystal]. The influence of the background is reduced by the use of differential amplitude discrimination. But the circumstance that the counter is in direct view of the specimen makes it impossible to work with highly active specimens.

A number of installations have been designed on the basis of the principle of a double diffractometer, when the diffraction maxima are registered after they have been reflected from the focusing monochromator crystal. In such a case protective shields can be installed between the specimen and the radiation detector.

In the double diffractometer described in reference [4], in the process of recording the x-ray pattern the lead shields are shifted together with the radiation detector, said detector being an end-window gas counter; this restricts shielding thickness. This restriction is removed if, in place of a counter, a tube is rotated [5].

Since the gas counter is characterized by high background sensitivity and large dead time, in the double diffractometer described in reference [6] use is made of a proportional or scintillation counter, and the possibility also exists for amplitude discrimination of the input pulses.

The use of a scintillation counter is made attractive by the fact that already at a thickness of 1 mm the NaI (Tl) crystal is almost 100% effective for  $\text{CuK}_\alpha$  x-radiation, and, in addition, its dimensions may be small. In order to reduce the influence of the background of the photomultiplier itself, the level of said background being comparable to pulses from x-ray quanta, one of the installations described in reference [7] uses a system of two coincidence-connected photomultipliers operating from a single crystal.

A very valuable quality of double diffractors is the fact that a strictly monochromatic beam arrives at the radiation detector. But double diffractors also have a number of drawbacks, of which the first that should be pointed out is the sharp reduction in beam intensity as a result of reflection from the monochromator crystal. These losses may comprise up to 90% of the intensity of the primary beam, this naturally greatly lengthening the survey time. Intensity losses may be reduced through the use of

a monochromator bent in two mutually perpendicular directions for the purpose of obtaining point focusing, but such a monochromator is difficult to prepare, and the gain from its use is not very great.

Furthermore, the configuration of a double diffractometer is determined by the wavelength of the x-radiation. When tubes are replaced, the system must be readjusted. In the case of hard radiation, the angle of reflection from the monochromator becomes small; this makes it difficult to shield the detector from background radiation. Double diffractometers are complex in design.

The installation of V. I. Karpukhin and V. A. Nikolayenko is built according to a different principle. In this installation the radiation detector is an ionization chamber, the current of which is amplified by a d-c electrometric amplifier. The component of the chamber current brought about by the  $\gamma$ -radiation of the specimen is compensated for by means of batteries.

This installation makes it possible to carry out a survey of specimens that possess much greater activity than can be processed by the previously mentioned installations. It is distinguished by simplicity of design and by the absence of heavy lead shields. At the same time the installation provides a high background level. All the inconveniences connected with the necessity for amplifying small direct currents by means of batteries are manifested in the operation of this installation.

In all the preceding cases the useful and the interfering radiations create in the detector signals of one kind -- pulses in counters (although differing with respect to amplitude), direct current in the chamber (although of differing value). Experience in work with installations similar to those considered above has caused the authors of the present article to arrive at the conclusion that, for reliable operation, a qualitative distinction should be made between the useful and the background signals. In accordance therewith an installation was designed, the distinguishing singularity of which is the modulation of x-radiation with respect to intensity. In such a case there is no particular difficulty in distinguishing a signal by means of a selective amplifier tuned to the modulation frequency.

Work was started in the spring of 1957, was resumed in 1960 after a protracted interval, and was completed in the middle of 1961.

It might, of course, be first of all possible in beam-modulation installations to use tubes with a modulating electrode, but such tubes are as yet not in series production. Tubes with a split rotating anode are very complex in design. On the basis of considerations of maximum simplicity, the URS-50I standard x-ray installation was used as a basis [9].

There are in principle two ways in which the x-ray beam of tubes of the BSV type can be modulated: via the power-supply circuits of the tube and via mechanical interruption of the beam [10, 11]. Preference was given to the latter method as being the most simple one, although it does have its drawbacks to which attention will subsequently be given.

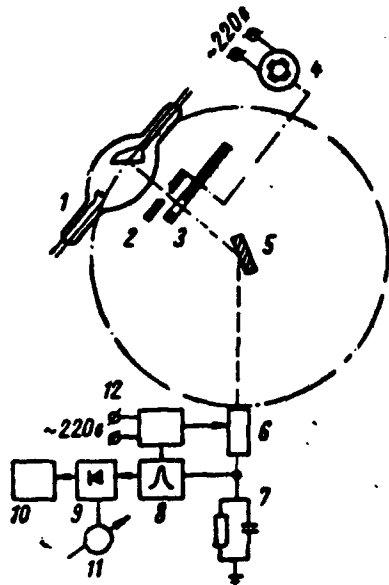


Figure 1. Block diagram explaining the principles of the installation:

- 1 - x-ray tube
- 2 - input crack
- 3 - modulator
- 4 - synchronous motor
- 5 - specimen
- 6 - radiation detector
- 7 - integrating R-C circuit
- 8 - selective amplifier
- 9 - detector
- 10 - recording potentiometer
- 11 - dial instrument
- 12 - power pack

Figure 1 shows a block diagram of the installation which explains its operation. Past the input crack, x-rays passing out of the tube window encounter a rotating disk, the thickness of which is sufficient for complete absorption of the beam. The disk has a specially shaped slit, as a result of which the intensity of the x-ray beam past the disk varies in accordance with a sinusoidal law with a cyclical frequency of  $f$  equal to the number of rotations of the disk per second. This same law of intensity change is obviously retained also in the reflected beam. Therefore the voltage on the integrating R-C circuit at the output of the detector has two components - a constant one, governed primarily by the radiation of the specimen itself, and a variable sinusoidal component, the envelope of which constitutes the diffraction pattern. The signal is differentiated and amplified by a narrow-band selective amplifier, is detected, and passes on to the recording potentiometer.

Let us assume at first that the specimen is inactive and that the radiation detector is a gas counter with small dead time. Let the diffraction pattern for this specimen be represented by the function  $\varphi(\Omega t)$ , where  $\Omega$  is the angular velocity of rotation of the goniometer, and  $t$  is the time counted off from the moment the goniometer passes some position

assumed to be the initial one. Then at an angular velocity  $\omega = 2\pi f$  of disk rotation, the intensity of the reflected x-ray beam is

$$n(t) = \varphi(\Omega t) \frac{1 - \cos \omega t}{2}. \quad (1)$$

Each  $1/\eta$ -th quantum, where  $\eta$  is the efficiency of the counter in relative units with respect to the radiation of a given wavelength, brings about the appearance of a charge  $q$  on the capacitor plates of the integrating R-C circuit. In the infinitesimally small time interval from  $\tau$  to  $\tau + d\tau$ , a charge of  $\eta q n(\tau) d\tau$  will go to the capacitance. By a certain moment in time  $t$ , the size of this charge is reduced to a value (equalling the origin of the coordinates with the moment  $\tau$ ) of

$\eta q n(\tau) e^{-\frac{t-\tau}{RC}} d\tau$ . The voltage corresponding to this charge will be

$$du = \frac{\eta q}{C} n(\tau) e^{-\frac{t-\tau}{RC}} d\tau. \quad (2)$$

The total voltage at the capacitor in an arbitrary moment in time  $t$ , thus, will be

$$u = \frac{\eta q}{C} \int_0^t \varphi(\Omega \tau) (1 - \cos \omega \tau) e^{-\frac{t-\tau}{RC}} d\tau. \quad (3)$$

For the special case of constant intensity  $N$  of the primary beam,  $\varphi(\Omega \tau) = N$ .

Carrying out the integration for this case, after simple transformations we obtain

$$u = \frac{1}{2} N q \eta R \left[ 1 - \frac{1}{\sqrt{1+a^2}} \cos(\omega t - \psi) - \frac{a^2}{1+a^2} e^{-\frac{t}{RC}} \right], \quad (4)$$

where

$$a = \omega RC = 2\pi \frac{RC}{T}.$$

The angle  $\psi$  constitutes the phase-shift angle between the voltage curve and the curve of intensity change;  $\psi = \arctg a$ . Here

$$\sin \psi = \frac{a}{\sqrt{1+a^2}}; \quad \cos \psi = \frac{1}{\sqrt{1+a^2}}. \quad (5)$$

The process of establishing the voltage is reflected in expression (4) by the exponential term, which in a steady process vanishes. The time of establishment should be assumed equal to about 5 RC.

The variable voltage component at the integrating R-C circuit takes the amplitude values in the moments in time

$$t_M = \frac{(2K+1)\pi + \psi}{\omega} \quad (6)$$

where K is any integer or zero.

The steady value of the amplitude is

$$U_M = \frac{Nq\eta}{2} \frac{R}{\sqrt{1+a^2}} \quad (7)$$

It depends on the ratio of the time constant of the integrating circuit to the modulation period, diminishing as this ratio is increased. When  $RC = T$ , for example, the amplitude of the variable component is equal to 0.157 of its maximum possible value. From equation (7) it can also be seen that, for a given time constant, the amplitude of the variable voltage component increases as the R/C ratio increases.

For the case of constant intensity of the primary beam, we define the relative mean-square reading error of the voltage amplitude at the integrating circuit. First of all it must be assumed that, during the modulation period, the radiation detector registers a sufficient number M of quanta to form the general nature of a sine law. Hence

$$l < \frac{\eta N}{M} \quad (8)$$

During the time interval from t to t+dt, the counter will register  $dn = \eta n(t)dt$  quanta with a mean-square error of  $\Delta dn = \sqrt{\eta n(t) dt}$ . At the moment of time  $t_M$  corresponding to the amplitude of the variable voltage component, the expected charge from the indicated number of quanta will be

$$dQ_M = \eta q n(t) e^{-\frac{t_M-t}{RC}} dt, \quad (9)$$

and its mean-square error will be

$$\Delta dQ_M = q \sqrt{\eta n(t) dt} e^{-\frac{t_M-t}{RC}} \quad (10)$$

Adding the dispersions of all the charges present at the capacitance at the moment in time  $t_M$ , and taking into account the fact that  $du = 1/C dQ$ , we obtain the mean square of voltage fluctuation for the moment  $t_M$

$$\overline{(\Delta U_M)^2} = \frac{q^2 \eta}{C^2} \int_0^{t_M} n(t) e^{-2 \frac{t_M-t}{RC}} dt. \quad (11)$$

The selective amplifier passes only the variable voltage component and for determination of the relative mean square of amplitude fluctuation the expression (11) must be divided by the magnitude  $U_M$ , determined from equation (7). Taking this into account, after substituting expression (1) and integrating we obtain

$$\frac{\overline{\Delta U_M^2}}{U_M^2} = \frac{1+a^2}{N\eta RC} \left[ 1 + \frac{2(2+a^2)}{(4+a^2)\sqrt{1+a^2}} - \frac{a^2}{4+a^2} e^{-2 \frac{t_M}{RC}} \right]. \quad (12)$$

For a steady amplitude, the exponential term is equal to zero. Here the average relative fluctuation of the amplitude is

$$\frac{\overline{\Delta U_M}}{U_M} = \frac{1}{\sqrt{N\eta RC}} \sqrt{\frac{(4+a^2)(1+a^2) + 2(2+a^2)\sqrt{1+a^2}}{4+a^2}}. \quad (13)$$

For operation without modulation the error would be equal to

$$\frac{\overline{\Delta U_M}}{U_M} = \frac{\overline{\Delta u}}{u} = \frac{1}{\sqrt{2N\eta RC}}. \quad (14)$$

Thus, for the same time constant of the integrating circuit the mean-square error under modulation conditions increases (the effect of the resonance amplifier is not considered here).

When the specimen is radioactive, the Geiger-Müller counter must be replaced by a proportional counter, a scintillation counter, or an ionization chamber. It was at first decided to work with a scintillation counter. Since the ultimate activity of the specimen would be limited by the saturation current and by the fatigue effects of the last FEU diodes, only the first two diodes were used in the experiments. The task of the scintillation counter with its load circuit was only to transform radiation energy

into electrical voltage, voltages being divided and amplified by a selective amplifier the amplification factor of which could be adjusted to  $\sim 10^7$ . Use was made of the FEU-31 on account of its comparatively small dimensions. But apparently such purposes would best be served by a FMK = 1/4 English photomultiplier having but two diodes and an external diameter of about 5 - 6 mm.

However, the difficulties involved in preparing satisfactory and durable NaI(Tl) crystals, and certain inconveniences in the operation of scintillation counters under hot conditions, prompted replacement of the scintillation counter by an ionization chamber.

When the design of the installation was simplified and its servicing was made easier, the chamber gave excellent results in operation under hot as well as under semihot conditions. It is true that the average reading fluctuation increased somewhat as a result of statistical fluctuations of the charge size in the chamber per absorbed quantum.

In view of the fact that the charge formed in the chamber when an x-ray quantum is absorbed is proportional to the energy of said x-ray quantum, the chamber possesses certain selective properties with respect to K-radiation in comparison with a Geiger-Müller counter. Quantitative data for specific conditions are cited in the discussion of the experimental curves at the end of the article.

Let us dwell on several singularities of design of a diffractometer with modulation. The parameters of the installation were approximately calculated on the basis of equations (7), (8), (13), and  $t_y = 5 RC$ .

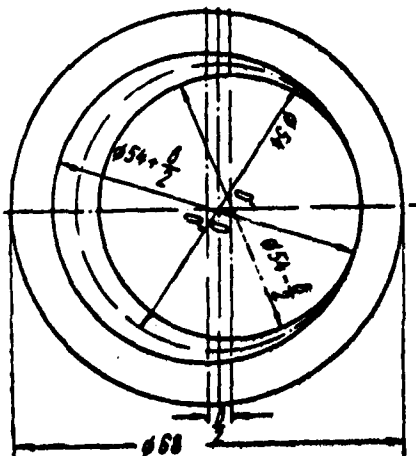


Figure 2. Modulator:

- O - center of rotation
- O' - geometrical center of internal disk
- O'' - geometrical center of external disk
- B - maximum height of beam

Modulator and drive. The shape and dimensions of the modulator are shown in Figure 2. The material is brass, 2 mm thick. In preparing the modulator, the ring and the internal disk are prepared separately, the latter being soldered to the ring with copper-zinc solder. With the modulator in a position as shown in Figure 2, the geometrical center of the ring is shifted downward with respect to the center of rotation, and the center of the internal disk is shifted upward by a quarter of the height of the x-ray beam. With such an arrangement, preparation of the modulator involves no difficulties, and the law of intensity change turns out to be very close to being sinusoidal. In operation under modulation conditions, the modulator crack with respect to height performs the functions of an input crack. A drawback of modulators that vary intensity at the expense of a change in the area (height) of the beam is the necessity of preparing specimens of a specific height. Modulators of atmospheric materials with variable thickness were also tested. They are considerably more complex to prepare; in addition, such a modulator is good only for a specific wavelength. It turned out to be simpler to prepare specimens of given dimensions for modulators of the first type; there were two such modulators, with a maximum crack height respectively of 2 and 3 mm.

The modulator is rotated by means of a synchronous SD-60 meter, the modulator being fastened directly on the axle of the reducing-gear box of said motor. The engine itself is fastened to a plate with runners, said runners being inserted into grooves of the input crack. By means of the runners, and an index pin provided in the plate, the modulator can be adjusted for height. Power is supplied to the motor directly from a 220-v, 50-cycle line. The initially planned auxiliary power-supply circuit with a quartz master oscillator proved to be unnecessary. An exterior view of the modulator and drive, fastened to the table with the tube, is shown in Figure 3. The modulation frequency is 1 cps.

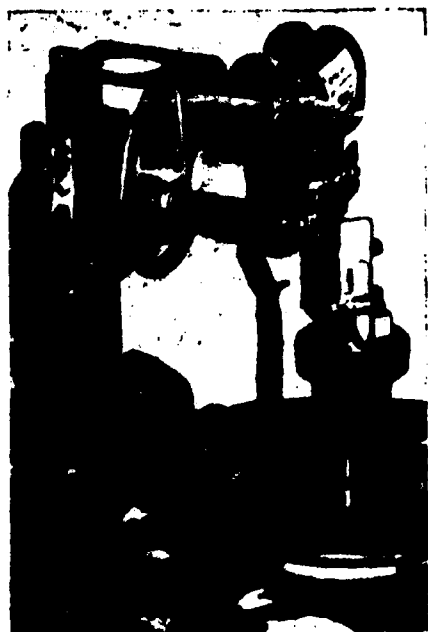


Figure 3. Exterior view of modulator and drive, fastened on table with tube

Radiation Detector. A series-produced current-operated MSTR-5 counter is used as an ionization chamber. The volt-ampere curve such a chamber at some intensity of the beam under modulation conditions is shown in Figure 4. Voltage values of the power supply of the chamber are plotted along the abscissa, and the amplitude values of the sinusoidal voltage at its load are plotted on an arbitrary scale along the ordinate. The signal does not depend on the voltage at the chamber if said voltage remains within the bounds of 15 - 50 v, and as long as these bounds are not exceeded radiation of constant intensity has no effect. When the voltage exceeds 50 v, the mechanism of gas amplification begins to go into effect and the content of the first harmonic of the modulation frequency in the signal voltage diminishes. At an excessively low voltage in the chamber, a signal reduction is as usual brought about by ion recombination. The initial voltage in the chamber was established at 45 v.

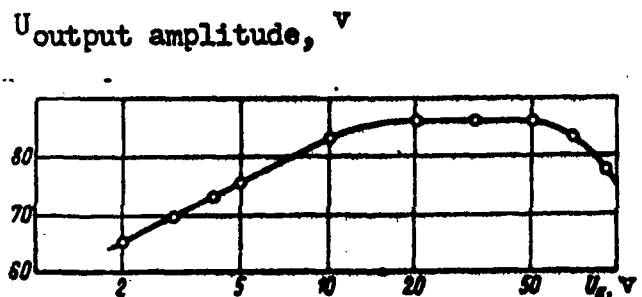


Figure 4. Volt-ampere curve of the current-operated MSTR-5 counter with modulation

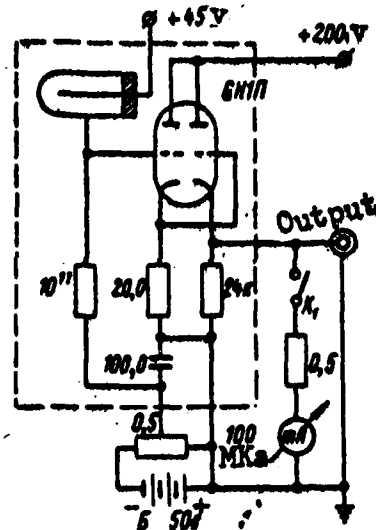


Figure 5. Schematic of preamplifier

Chamber load and preamplifier (Figure 5). The chamber load is a  $10^{11}$  ohm resistance, together with the input capacitance of the preamplifier and the assembly capacitance which have a total value of  $20 \mu\mu f$ . Here x-radiation with an intensity of 50 quanta per second is registered with a probable error of about 5%.

The preamplifier must possess a high input resistance and should be able to withstand considerable overloads. These requirements are satisfied by a preamplifier consisting of two series-connected cathode repeaters. A large resistance of 20 M ohms is connected to the filament

circuit of the first tube, as a result of which the voltage at its grid is established at a point close to the cutoff potential, while the plate current of the tube amounts to fractional parts of a microampere. Thus both the electron and the ion components of the grid current are set aside. In the grid circuit there flows a current determined by leakages between the grid and the other electrodes of the tube. With appropriate processing of the tube bulb [12], the value of this current amounts (in the case at hand) to  $10^{-12}$  a.

Since the output resistance of the first cathode repeater is great, the signal is picked up from it via a second cathode repeater of the conventional type. The overall transmission factor of the preamplifier is equal to 0.81. The operation of the preamplifier is not disrupted by delivery to the input of voltages with a positive polarity of up to 150 v.

For the case of high activity of the specimen, which may bring the working point of the chamber beyond the limits of the plateau of the volt-ampere curve, there is incorporated a compensation circuit for change of the constant voltage in the chamber. The circuit consists of a battery and a potentiometer, the lower end of the chamber load resistance being connected to the blade of said potentiometer. Invariability of the working point is established on the basis of readings from a voltmeter connected to the output of the preamplifier by means of the tumbler  $K_1$ . The part of the preamplifier lying outside the dotted line is located on the control panel.

The selective amplifier (Figure 6) consists of two three-tube sections. In each section there are two negative-feedback circuits, one of which is independent of frequency and embraces the entire section. The purpose of this negative feedback is stabilization of the amplifier parameters. The signal for this feedback is taken off the filament of the last tube of the section, and is fed to the filament of the first tube in said section.

The second feedback circuit defines the selective properties of the amplifier. This feedback is effected through a double T-shaped bridge from the plate to the grid of tube  $J_1$  (in the first section) and of tube  $J_5$  (in the second section). In order to obtain the required shape of the selectivity curve (Figure 7), the resonance frequencies of the bridges differ by 0.04 cps.

The amplification factor may be varied stepwise and continuously within the bounds of 2 to  $10^7$  (at a frequency of 1 cps). The amplification factor of the first section is equal to 2,000. By means of the switch  $J_1$ , the voltage at the output of this section may be subdivided 10, 100, and 1,000 times. In addition, at one of the positions of the switch the signal is taken directly from the plate of the first tube; here the amplification is equal to 20.



Continuous regulation of the signal value at the output of the first sections is carried out by the potentiometer  $R_3$ . By means of the tumbler  $\sqrt{2}$ , it is possible to connect to the output of the first section either the entire second section with an amplification factor of up to 5,000, or only the cathode repeater operating on the basis of tube  $\sqrt{6}$ .

The designation of the remaining regulatory organs is as follows: The variable resistances  $R_2$  and  $R_5$  serve to adjust the amplification factor to the assigned value in the initial alignment, and the Q-factor of the double T-shaped bridges is regulated by means of the variable resistances  $R_1$  and  $R_4$ . From the amplifier output the signal passes to the bridge detector, assembled on the basis of DGTs-27 semiconductor diodes. The rectified voltage is indicated by a M-24 pointer-type instrument, and is recorded on a EPP-09 recording potentiometer.

It should be noted that when working only with chambers, there is no need for large values of the amplification factor. Besides, when the amplification factor exceeds  $10^6$  (this took place in the course of experimental work with photomultipliers), the amplifier became very sensitive to various kinds of induction, and due to the low resonance frequency was also very sensitive to jolts in the power network caused by the switching on and off of power equipment operating from the same network. For these reasons the above-described amplifier was powered by highly stabilized voltages. Below are cited some results of experimental testing of the operation of the installation as a whole.

Figures 8a and 8b show lines (111) and (200) of an x-ray pattern of aluminum. The specimen is inactive. It was in the shape of a 12 x 3 x 2 mm plate with a polished reflecting surface. The first x-ray pattern was obtained on a URS-50 I machine in the conventional manner with registration of the quanta by a MSTR-5 gas counter. The second x-ray pattern was obtained with modulation of the x-ray beam intensity and with the MSTR-5 counter operated by current. In both cases radiation is of the copper type, the voltage at the tube anode is 30 kv, the plate current in the first case is 4 ma and in the second case is 10 ma. The angular velocity of the goniometer, as everywhere in the succeeding experiments, is 1 degree/minute. For convenience of comparative evaluation the peak height was made approximately equal. The ratio of the integral intensities of  $\alpha$  -lines (111) and (200) was in the first case equal to 1.045, and in the second case was equal to 1.042, i.e., the results of the two methods coincide within the limits of planimetry errors.

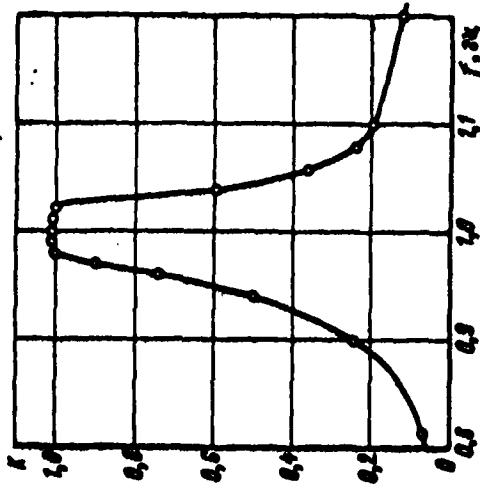


Figure 7. Selectivity curve of the amplifier

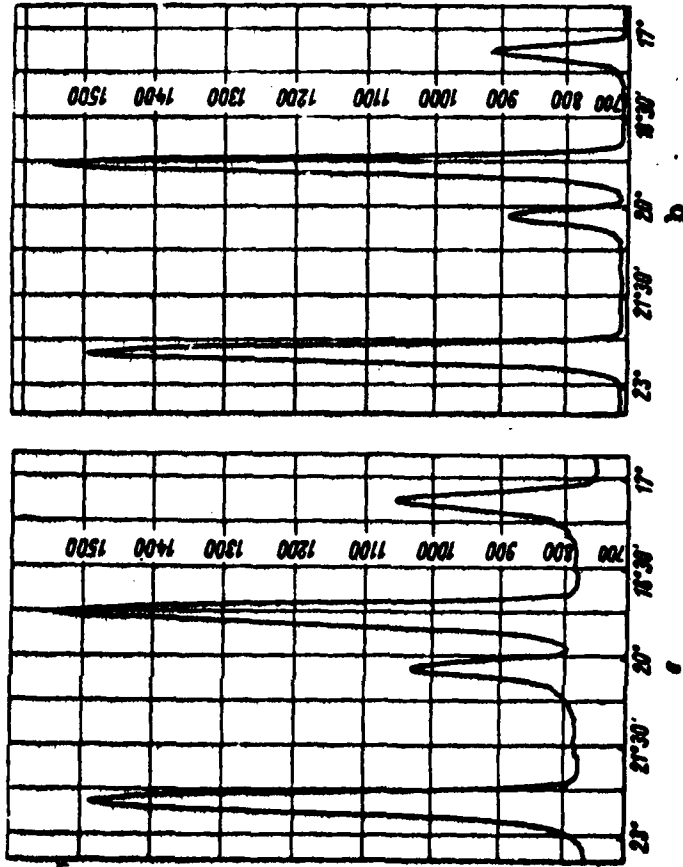


Figure 8. Intensity curves of lines (111) and (200) of aluminum:

- a - without modulation, with counter;
- b - modulation conditions, with chamber.

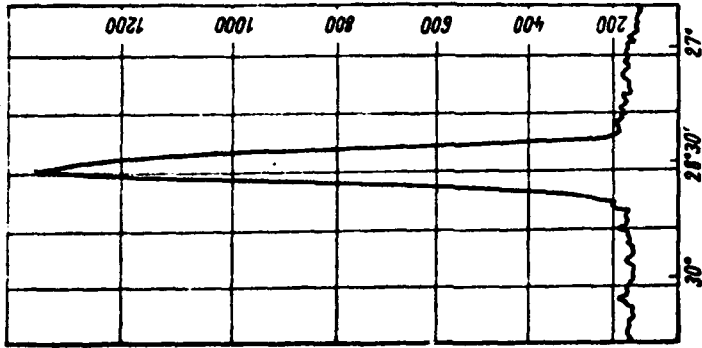
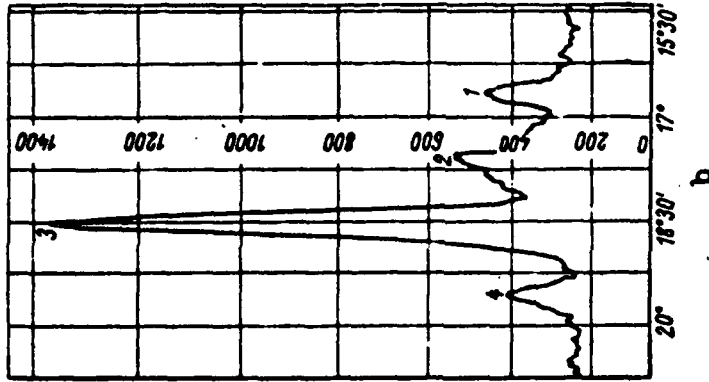
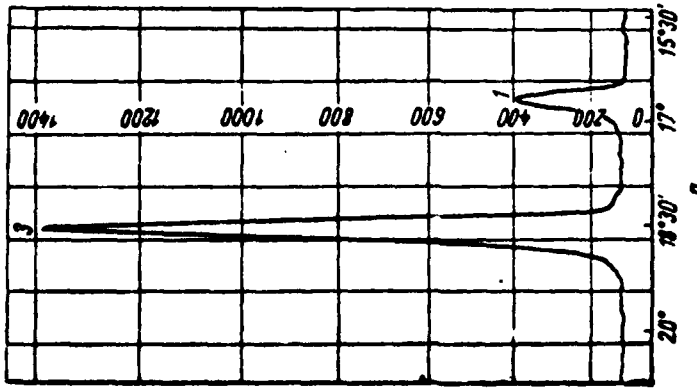


Figure 10.  $\alpha$ -line (110) of stainless steel. Specimen activity is 1  $\mu$  curie



b



a

Figure 9. X-ray patterns of the UM-9 uranium-molybdenum alloy:

a - before irradiation; b - after irradiation, specimen activity is 0.6 curie; uranium lines: 1 -  $\beta$ -line (100) of the  $\gamma$ -phase; 2 -  $\alpha$ -line (021) of the  $\alpha$ -phase; 3 -  $\alpha$ -line (110) of the  $\gamma$ -phase; 4 -  $\alpha$ -line (111) of the  $\alpha$ -phase.

Attention should be drawn to the fact that, with modulation, dispersed x-radiation is not registered (since it is not modulated) and the background here is practically absent. This circumstance increases line resolution and raises the precision of determination of the integral intensity. Hence follows the conclusion of the usefulness of the method of modulation with respect to intensity in the analysis not only of active, but also of conventional specimens.

The ratio of integral intensities of the  $\alpha$ - and  $\beta$ -lines (111) when the counter operates on current increased 1.8 times, this being explained by the "course with rigidity" ["khodom s zhestkost'yu"] of the chamber.

The x-ray patterns cited below were obtained with modulation of the intensity of x-radiation. Figure 9a shows the (110) line of the  $\gamma$ -phase of the UM-9 uranium-molybdenum alloy, and Figure 9b shows an x-ray pattern of the same alloy after irradiation, where the appearance of a new phase of  $\alpha$ -uranium is noted. The activity of the specimen amounted to 0.6 curie.

Figure 10 shows a recording of the intensity curve of the  $\alpha$ -line (110) from a specimen of stainless steel with an activity of 1  $\mu$  curie.

It is obvious that the activity of the specimen in case of the survey method set forth can be very great, and is limited in practice only by considerations of personnel safety. At present work is being completed on automation of the control of a GUR-3 type goniometer installed in a hot chamber. The results of surveys of highly active (several curies) specimens will be communicated separately.

#### BIBLIOGRAPHY

1. Ibragimov, Sh. Sh., Karmilov, A. G., Lyashenko, V. S., Fizika metallov i metallovedeniye, Vol. 10, No. 2, 1960.
2. Sidhu, S. S., Compos, F. P., Zaubereis, D. D., Nuclear Science and Engineering, Vol. 3, No. 6, 1958.
3. Kohler, T. R., Parrish, W. Rev. Scient. Instrum., Vol. 26, No. 4, 1955.
4. Konobeyevskiy, S. T., Levitskiy, B. M. Martynyuk, Yu. A., Zhurnal tekhnicheskoy fiziki (Journal of Technical Physics), Vol. 26, No. 4, 1956.

5. Cummings, W. V., Kaulitz, D. C., Sanderson, M. O., Rev. Scient. Instrum., Vol. 26, No. 1, 1955

6. Bredig, M. A., Krein, G. E., Borie, B. S., Rev. Scient. Instrum. Vol. 26, No. 6, 1955.

7. Batenin, I. V., Sharov, B. V., Pribory i tekhnika eksperimenta (Instruments and Equipment in Experimentation), No. 3, 1956.

8. Karpukhin, V. I., Nikolayenko, V. A., Pribory i tekhnika eksperimenta, (Instruments and Equipment in Experimentation), No. 6, 1960.

9. Ioffe, Ya. K., Kristallegrafiya (Crystallography), Vol. 1, No. 4, 1956.

10. Matalin, L. A., Ivanov, A. A., Pribory i tekhnika eksperimenta, No. 2, 1957.

11. Griбанov, Yu. I., Author's Certificate [Patent] No. 127470 with priority from 16 June 1959.

12. Griбанov, Yu. I., Izmereniye napryazheniy v vysokoomnykh tsepyakh (Measurement of Voltages in High-Resistance Circuits). Moscow, Gosenergoizdat, 1961.

6306

CSO: 1879-D

- END -